

A RADIATION DOSIMETRY MODEL FOR
RADIOLABELED MONOCLONAL ANTIBODIES:
INDIUM-111 LABELED B72.3-GYK-DTPA
FOR COLORECTAL CANCER

By

LATRESIA ANN WILSON

A DISSERTATION PRESENTED TO THE GRADUATE SCHOOL
OF THE UNIVERSITY OF FLORIDA IN PARTIAL FULFILLMENT
OF THE REQUIREMENTS FOR THE DEGREE OF
DOCTOR OF PHILOSOPHY

UNIVERSITY OF FLORIDA

1990

UNIVERSITY OF FLORIDA



3 1262 08552 3487

Copyright 1990

by

Latresia A. Wilson

ACKNOWLEDGEMENTS

First and foremost, I would like to thank my family for their love and support throughout the years. I would especially like to thank my uncle, Manuel Lewis Jr., for his wisdom and support; my grandmother, Lula Lewis, for her patience and understanding; my mother, Geraldine Solomon, for her encouragement and support; my aunts, Evelyn Scott and Marilyn Johnson, for believing in me; and my cousins for their encouragement.

I would especially like to thank Dr. Genevieve Roessler for believing and supporting me during the rough years. I am very thankful to my advisor, Dr. William Properzio, for his superb guidance and support throughout this study. I am also grateful to my advisory committee, Dr. Emmett Bolch, Dr. Walter Drane, Dr. David Hintenlang, and Evelyn Watson, for their guidance and help in this project.

x I would like to thank Evelyn Watson and the staff (Mike Stabin, Audrey Schlafke-Stelson, Fanny Smith, and Stan Walls) of the Radiopharmaceutical Internal Dosimetry Center of Oak Ridge Associated Universities. I would like to thank Oak Ridge
x Associated Universities for giving me the opportunity and resources to learn from the best in my field. I would like to especially thank Martha Kahl and Rana Yalcintes in the medical

library of Oak Ridge Associated Universities for their excellent support. I would like to thank the staff of the Nuclear Medicine Department at the University of Tennessee Hospital for their guidance, patience, and use of their equipment. I would like to thank Phyllis Cotten, Carmine Plott, James Stubbs, Pat Harp Family, and the Rose Foster Family for making my stay in Tennessee an enjoyable one.

I would like to thank Dr. Steven Harwood, Michelle Morrissey, Linda Zangara, Dr. Will Webster, Dr. Carroll and Dave Laven and staff of the Nuclear Medicine Department at Bay Pines Veterans Administrative Medical Center in Bay Pines, Florida for providing the patient data, use of their facilities, and financial and expert support in this project.

I would like to thank the people of the Department of Environmental Engineering Sciences, Dr. Charles Roessler and fellow graduate students for their encouragement and support. I would like to also thank Dr. Libby Brateman for being there to answer all my seemingly endless number of questions and for providing support.

I would like to thank Dean Rodrick McDavis for his continued support. And last, I would like to thank the McKnight Foundation and the Florida Endowment Fund for Higher Education, Dr. Israel Tribble and staff, for their financial support for without which, this degree would never have been undertaken.

TABLE OF CONTENTS

	<u>page</u>
ACKNOWLEDGMENTS	iii
LIST OF TABLES	vii
LIST OF FIGURES	ix
ABSTRACT	xi
 CHAPTERS	
1 INTRODUCTION	1
2 MONOCLONAL ANTIBODIES	6
Immunoglobulin Structure	9
Variables Associated with Radioimmunoimaging and Radioimmunotherapy	14
Tumor Localization	17
Choice of Radiolabel	18
Tumor Size Effect	24
Fragment vs Whole Antibody	25
Dose Administered Effect	27
Labeling Method Effect	28
Dose Administration Route	29
Tumor Biology	30
Other Factors	31
3 RADIATION DOSIMETRY	34
MIRD Approach	36
"Traditional" Point Kernel Method	38
Microdosimetry	41
4 MATERIALS AND METHODS	47
SPECT Model	49
Monte Carlo Model	49
Dosimetry Model	51
Single-Photon Emission Computed Tomography ..	51
SPECT Quantitation	53
Photon Attenuation	54
Photon Scatter	56
SPECT Camera System	57
Image Segmentation	58
Program SPECTDOSE	60
Subroutine THOLD	63
Subroutine CONTOUR	63
Subroutine OBJSELECT	63

Subroutine CORGAN	67
Subroutine VOXFIL	69
Program ALGAMP	69
Pixel and Slice Size Determination	72
Phantom Studies	73
Phantom Study One	74
Phantom Study Two	76
Phantom Study Three	80
Thermoluminescent Devices	84
Clinical Studies	85
Patients	85
Monoclonal Antibody	86
Monoclonal Antibody Procedure	86
Blood Analyses	88
HPLC Procedure	88
Image Analysis	89
5 RESULTS AND DISCUSSION	90
Pixel and Slice Size Determination	91
Phantom Study One	91
Phantom Study Two	97
Phantom Study Three	112
Clinical Study	129
6 SUMMARY AND CONCLUSIONS	133
REFERENCES	140
APPENDICES	
A SAMPLE CALCULATIONS.....	154
B TLD CALIBRATION.....	157
C SPECTDOSE PROGRAM	158
BIOGRAPHICAL SKETCH	181

LIST OF TABLES

Table 2-1	Properties of Human Immunoglobulins	11
Table 2-2	Properties of Human IgG Subclasses	12
Table 2-3	Selected Radionuclides for Radioimmunodetection and Radioimmunotherapy	19
Table 2-4	Radionuclides for Radioimmunodetection and Radioimmunotherapy	21
Table 3-1	Sublethal Radiation Doses.	44
Table 4-1	Phantom Study One Acquisition Parameters	75
Table 4-2	Phantom Study Two Acquisition Parameters	77
Table 4-3	Phantom Study Two Experiments	79
Table 5-1	Phantom Study One Threshold Determination	92
Table 5-2	Phantom Study One Results	94
Table 5-3	Phantom Study Two Threshold Determination	98
Table 5-4	Phantom Study Two Experiment One Results	100
Table 5-5	Phantom Study Two Experiment Two Results	102
Table 5-6	Phantom Study Two Experiment Three Results	104
Table 5-7	Gaussian Prefilter Comparison: Actual versus SPECT Measured Volume	107
Table 5-8	Phantom Study Two Absorbed Dose Results	110
Table 5-9	Phantom Study Three TLD Measurements.	114
Table 5-10	Phantom Study Three Geometric Factor Method and MIRD Pamphlet No. 3 Results	117
Table 5-11	Phantom Study Three Dosimetry Model Results	118
Table 5-12	Phantom Study Three Results	120

Table 5-13 Phantom Study Three Error Anaylsis.	121
Table 5-14 TLD Calibration Study Results	123
Table 5-15 Phantom Study Four TLD Measurements	127
Table 5-16 Phantom Study Four Results.	128
Table 5-17 Phantom Study Four Error Analysis	130
Table 5-18 Clinical Study Results	131

LIST OF FIGURES

Figure 1-1	Antibody Carriers for Diagnosis and Therapy	3
Figure 2-1	Monoclonal Antibody Production	8
Figure 2-2	HAT Mediated Hybridoma Production	10
Figure 2-3	IgG Molecule	13
Figure 2-4	Enzymatic Digestion of IgG Molecule into Fragments	15
Figure 4-1	Research Methodology.	48
Figure 4-2	Single-Photon Emission Computed Tomography .	52
Figure 4-3	SPECT Model Flow Chart.	61
Figure 4-4	SPECTDOSE Program Subroutine Flow Chart . . .	62
Figure 4-5	Illustration of Subroutine THOLD Object Segementation	64
Figure 4-6	Subroutine CONTOUR Object Segmentation . . .	65
Figure 4-7	Subroutine CONTOUR Object Assignment	66
Figure 4-8	Illustration of Subroutine OBJSELECT Selected Object Comparison	68
Figure 4-9	ALGAMP Flow Chart	70
Figure 4-10	Phantom Study Two Torso Phantom and Organ Inserts	78
Figure 4-11	Phantom Study Three Experiment One TLD Location	82
Figure 4-12	Phantom Study Three Experiment Two TLD Location	83
Figure 4-13	B72.3 Linker Complex	87

Figure 5-1	Phantom Study One:Actual versus SPECT Measured Volume	95
Figure 5-2	Phantom Study One:SPECT Measured versus Actual Activity Concentration	96
Figure 5-3	Phantom Study Three TLD Experimental Locations.	113
Figure 5-4	Phantom Study Four TLD Chip Packaging	124
Figure 5-5	Phantom Study Four TLD Locations	126

Abstract of Dissertation Presented to the Graduate School
of the University of Florida in Partial Fulfillment of the
Requirements for the Degree of Doctor of Philosophy

A COMPUTERIZED RADIATION DOSIMETRY MODEL FOR
RADIOLABELED MONOCLONAL ANTIBODIES:
INDIUM-111 LABELED B72.3-GYK-DTPA
FOR COLORECTAL CANCER

By

LATRESIA ANN WILSON

DECEMBER 1990

Chairperson: William S. Properzio
Major Department: Environmental Engineering Sciences

A foundation was developed for a dosimetry methodology that could be used to calculate absorbed doses in target and nontarget tissues using uniformly and nonuniformly distributed activity. In this methodology, a dosimetry model was developed which consisted of three independent models: 1) the SPECT Model, 2) the Monte Carlo Model, and 3) the Dosimetry Model. The SPECT Model uses Single-Photon Emission Computed Tomography (SPECT) images to determine the volume and radioactive uptake. A computer program was written to automatically read and analyze SPECT images. This program uses an edge detection method to determine the volume. Voxel elements within the identified volume are used to calculate the activity concentrations. The Monte Carlo Model uses a monte carlo simulation method

and results of the SPECT Model to calculate the fraction of photon energy deposited in target and nontarget tissues. The Dosimetry Model combines the results of the SPECT and Monte Carlo Models to determine the absorbed dose in target and nontarget tissues.

Several phantom studies were conducted to verify the ability of the Dosimetry Model to evaluate organ and tumor uptake, sizes, and to calculate absorbed doses. Comparisons were made between the Dosimetry Model, other calculational methods (MIRDOSE2, Geometric Factor Method, MIRD Pamphlet No. 3), and TLD measurements.

For diagnostic activity doses, the SPECT Model was found to calculate organ volumes of the order of 1000 ml to within fifteen percent of the actual volumes but it failed to accurately calculate organ volumes of 200 ml or less.

No meaningful relationship was found between the actual and SPECT measured activity concentrations.

The Dosimetry Model agreed within 12% when compared with the Geometric Factor Method and the MIRD Pamphlet No.3 results using homogeneously and heterogeneously distributed ¹¹¹In. The TLD measurements were within 30% at most of the other methods.

Results of the several phantom studies indicated the Dosimetry Model was an appropriate methodology for calculating absorbed doses for homogeneously distributed activity. Further investigation is needed to determine the

accuracy of the Dosimetry Model in the heterogeneously distributed activity case.

The addition of photon attenuation and scatter correction and nonpenetrating radiation transport is pertinent to the accuracy of the dosimetry methodology.

CHAPTER 1

INTRODUCTION

In the United States, cancer is the second leading cause of death with the number of annual deaths fast approaching 400,000 (1). This value represents a little over 20% of all deaths. Women are more susceptible to cancer than men and except for accidents, cancer kills more children than any other illness (1). In England, cancer is the leading cause of death in children 1-14 years of age (1).

Utilization of antibodies to fight cancer started as early as 1946 when Pressman theorized that polyclonal antibodies directed against antigens expressed on tumor cells could be used to localize radionuclides in the tumor. He believed that once the antibodies were bound to the antigen-rich tumor site, the radioactivity could be detected with a gamma scanning device or if the radionuclide concentration in the tumor was sufficient, serve as local radiation therapy. So, after a series of ingenious experiments, he successfully demonstrated that immune proteins could be used to target radioactivity to tumors in

living animals (2). Unfortunately at that time, it was difficult to produce antibodies that would survive in cultured media, thus limiting the ability to produce sufficient amounts with the specificity needed for clinical studies. This ultimately limited the further use of this technology for many years to come.

In 1975, Köhler and Milstein introduced a new technique called hybridization, which would allow for the production of large quantities of identical (monoclonal) antibodies (3). This technique made it possible for the methodologies proposed by Pressman to be applied clinically. Köhler and Milstein later went on to receive the Nobel Prize for their contribution.

With the advent of the hybridization technique, there was renewed interest in the use of radiolabeled antibodies for tumor therapy. It is generally believed that monoclonal antibodies attached to radiolabels for therapy (radioimmunotherapy) may be effective in treating metastases and small tumors, where surgery may not be feasible. This new technique offers some ray of hope in the fight against cancer.

Recent advances in biotechnology have given new hope to achieving the ultimate goal of using monoclonal antibodies for targeting radioactivity for the dual purpose of cancer diagnosis and therapy (Figure 1-1). This potential has

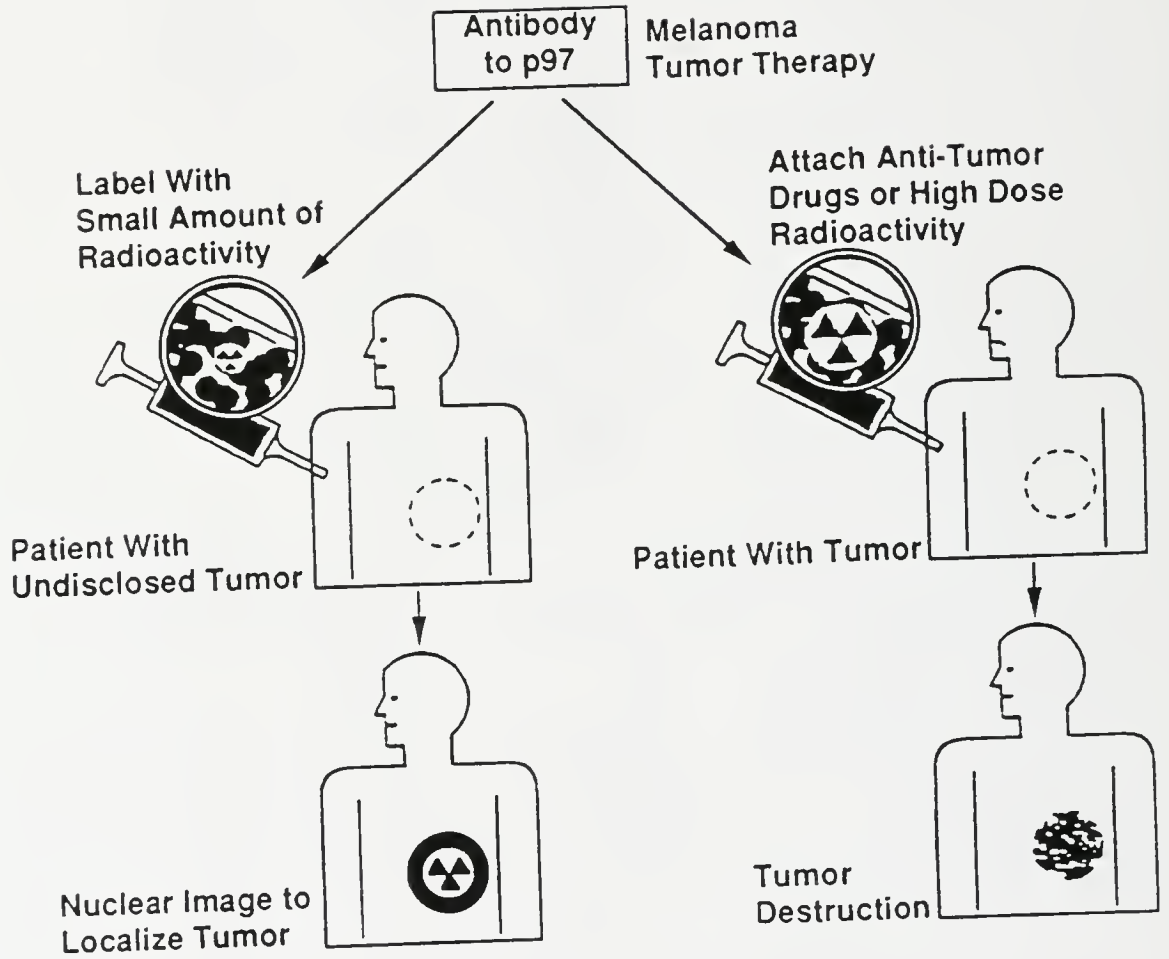


Figure 1-1. Antibody Carriers for Diagnosis and Therapy*

* Adapted from Reference 4

generated a significant amount of interest and growth in the field of nuclear medicine over the past few years. This growth, in turn, has generated many new problems and questions. One of these problems, the radiation dosimetry of using radiolabeled monoclonal antibodies, is the focus of this research.

Current radiation dosimetry methods, which allow for the calculation of absorbed doses for both target and nontarget tissues, assume that the radiolabel's energy is distributed uniformly throughout the target and nontarget organ. This assumption is not valid in the case of radioimmunotherapy, since it has been shown that radiolabeled monoclonal antibodies distribute heterogeneously throughout a given organ and on the tumor cell (5). It is, therefore the objective of this research to develop a foundation for a radiation dosimetry methodology that could be utilized for radiolabeled monoclonal antibodies; i.e., a methodology which would allow for the calculation of absorbed doses in tissues with a heterogeneous or homogeneous radioactivity distribution. A computerized dosimetry model, which allows for the calculation of absorbed doses to both target and nontarget tissues after intravenous (IV) injection of Indium-111 labeled B72.3-GYK-DTPA monoclonal antibody directed against colorectal cancer, will be proposed in this research. Clinical applications and ease-of-use of this dosimetry

model will be emphasized. A comparison of the results from this model with that of current dosimetry methods will be made.

This dissertation is divided into five basic sections. First, an overview of monoclonal antibodies and the factors that affect their localization are presented. Second, there is a discussion of the current radiation dosimetry methods and their inadequacies for use with radiolabeled monoclonal antibodies. Third, a discussion of the experimental methods, computer models, and imaging techniques used in this study are presented. Next, the computational results are presented and analyzed. Finally, the results are summarized and suggestions for future applications of this method are made.

CHAPTER 2

MONOCLONAL ANTIBODIES

Antibodies, or immunoglobulins, are proteins made by many animal species as part of their specific response to foreign substances (antigens). When antibody-antigen binding occurs, this immunologic response usually results in the destruction or elimination of the antigen.

Immunoglobulins are produced by the activity of the B lymphocytes and possess specific binding regions that recognize the shape of particular sites or determinants on the surface of the antigen. An antigen may have several determinants, or epitopes, each of which is capable of stimulating one or more B lymphocytes. For this reason, an antigenic challenge results in the production of a variety of antibodies (6).

Early antibody production techniques employed the use of animals, usually a mouse or rabbit, immunized with an antigenic substance, to obtain antibodies, which were found in the serum of the immunized animal. These antibodies were

polyspecific because they reacted with a wide variety of antigenic binding sites.

Highly specific antibodies can be developed by extracting individual lymphocytes and cloning them in tissue culture; each clone would have the potential to manufacture a single antibody species, a monoclonal antibody (Figure 2-1). Unfortunately, normal antibody-producing cells do not survive in culture media. It took Nobel laureates Köhler and Milstein (3) to recognize that myeloma cells, which are cancer cells that produce large amounts of identical but nonspecific immunoglobulins, and which can survive in cultures indefinitely, might be altered by the new techniques of recombinant genetics to construct immortal clones that secrete immunoglobulins.

Köhler and Milstein developed a method of producing such monoclonal antibody strains by fusing the lymphocytes from the spleen of an immunized mouse with mouse myeloma cells, thus forming clones of hybrid cell lines, called hybridomas (4). These cells are usually fused in polyethylene glycol and result in clones that have the specific-antibody characteristics of the lymphocytes and the longevity of the myeloma cells. Additionally, pure hybridoma cells are selectively grown in hypoxanthene-aminopterin-thymidine (HAT) media since it supports neither the unfused lymphocytes nor the myeloma cells. Once these hybridomas are produced, they can be assayed for antibody activity and for

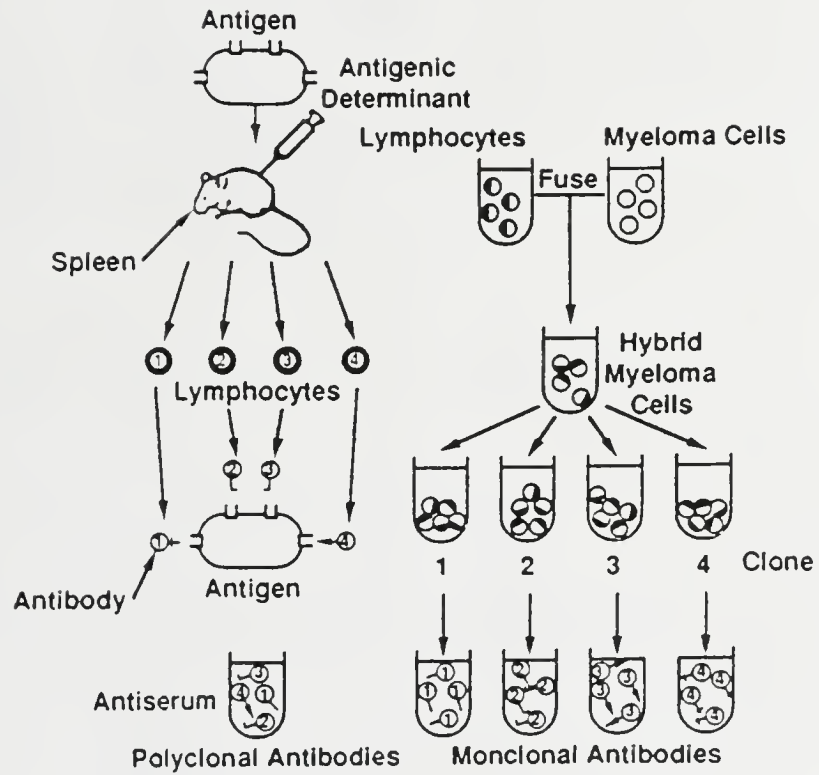


Figure 2-1. Monoclonal Antibody Production*

* Adapted from Reference 4

further selective cultivation (Figure 2-2). The reader is referred to Reference 6 for an excellent review of the techniques involved in the production, purification, analysis, quality control, radiolabeling, and storage of monoclonal antibodies.

Immunoglobulin Structure

Immunoglobulins (Ig) are divided into five classes: IgG, IgA, IgM, IgD, and IgE and can further be subdivided (isotypes) on the basis of internal attributes (see Table 2-1 and 2-2). IgM antibodies are often the first to appear during immunization and IgE antibodies mediate hypersensitivity reactions (8).

Immunoglobulins of all classes are composed of two heavy (H) chains and two light (L) chains in their simplest form. All classes share the same light chains and differ solely in the structure of the heavy chains. The heavy chains are attached to one another by means of one or more disulfide bonds, and a light chain is attached to each heavy chain by a disulfide bond (Figure 2-3). Isotypes differ structurally in the number of disulfide bonds linking the two heavy chains together, and they differ functionally in their ability to fix complement and to interact with effector cells such as macrophages and mast cells (Table 2-2).

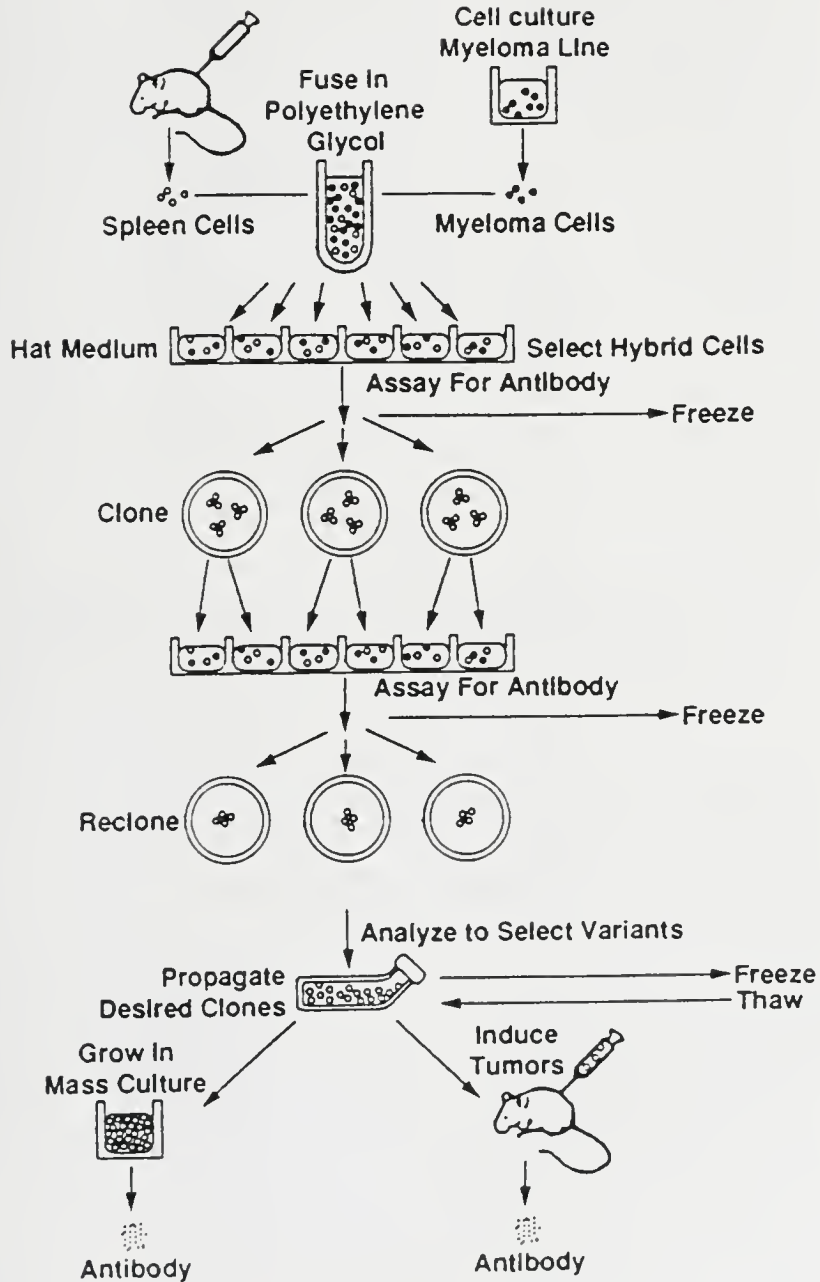


Figure 2-2. HAT Mediated Hybridoma Production*

* Adapted from Reference 7

Table 2-1. Properties of Human Immunoglobulins†

	IgG	IgA	IgM	IgD	IgE
Normal adult serum concentration (in g 100 ml ⁻¹)	1.0-1.4	0.2-0.3	0.04-0.15	0.003	10 ⁻³ -10 ⁻⁵ (avg ≈ 10 ⁻⁴)
Distribution	Intvas.* excel.** fluid	Intvas. internal secr.***	Mainly intvas.	Mainly intvas.	Intvas. and skin respiratory, GI tracts
Intravascular (%)	45	42	80	75	51
Molecular Weight	150,000	155,000	900,000	185,000	187,000
Molecular Weight of H Chains (MW of L chains ≈ 23,000)	53,000	55,000	65,000	70,000	71,000
Normal H/L chain ratio	2/1	5/4	3/1	1/6	?
H chain subclasses	IgG1, IgG2 IgG3, IgG4	IgA1, IgA2	IgM1, IgM2	Ja, La	-
Approximate occurrence of the H chain subclass (%)	75, 15, 7, 3	93, 7	-	85, 15	-
Half-life (days)	23	6	5	3	3

† Adapted from Reference 8
 * Intravascular
 ** Extracellular
 *** Secretions

Table 2-2. Properties of Human IgG Subclasses*

	IgG1	IgG2	IgG3	IgG4
H chains	1	2	3	4
Approximate occurrence in serum (%)	70	20	7	≈3 (rather variable)
Half-life (days)	20	24	7	23
Electrophoretic mobility	Slow	Fast		Fast
Complement binding	++	+	++++	-
Placental transport	+	±	+	+
Binding to macrophages and monocytes	+	-	+	-
Papain digestibility	Most readily	Only after reduction with mercaptoethanol	Readily	After reduction with cysteine
Aggregation	+(Fab only)	+(Fab only)	+++ (Both Fab and Fc)	+(Both Fab and Fc)

* Adapted from Reference 7

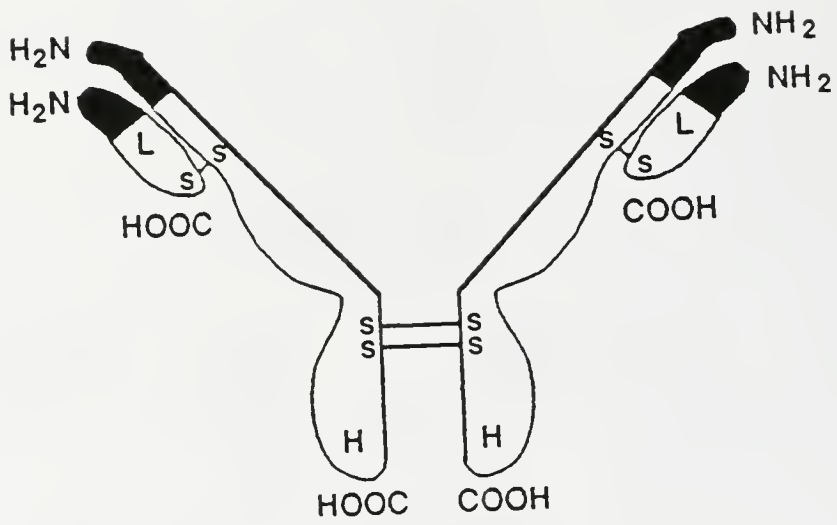


Figure 2-3. IgG Molecule*

* Adapted from Reference 8

The antibody-specific sites of the immunoglobulins are situated near the amino-terminal (NH_2) end of each of the four chains (Figure 2-3), and it is in this region (variable region) that the greatest variability in amino acid sequence occurs from immunoglobulin to immunoglobulin (9). Constant amino acid sequences are found in the carboxyterminal (COOH) regions (constant region) of the immunoglobulin chains (Figure 2-3). The two variable regions bind to specific antigenic sites and the constant region (Fc) interacts with the host immune system.

Since the Fc region of the antibody is most likely to trigger allergic responses, fragmentation has been used to remove this portion from the antibody molecule. Pepsin, a proteolytic enzyme, cleaves off most of the Fc region, which leaves two Fab fragments bound together in a divalent structure known as the F(ab')_2 fragment (Figure 2-4). The enzyme papain breaks the immunoglobulin into two monovalent Fab fragments and an intact Fc fragment.

Variables Associated with Radioimmunoimaging and Radioimmunotherapy

A number of variables that must be considered before diagnostic and therapeutic applications of monoclonal antibodies can be utilized. Generally monoclonal antibodies alone are not effective in tumor destruction (10). This has been attributed in part to the heterogeneous distribution of tumor-associated antigens on cell surfaces, which leads to

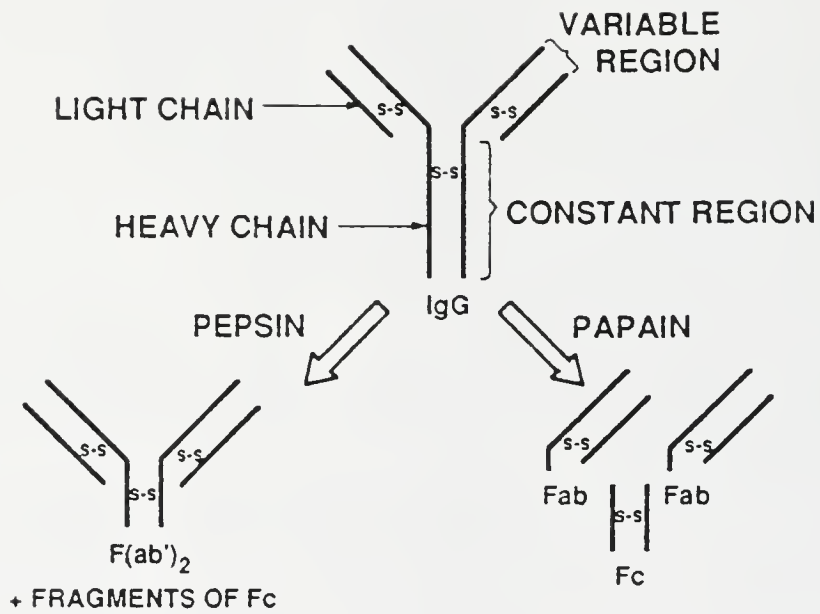


Figure 2-4. Enzymatic Digestion of IgG Molecule into Fragments*

* Adapted from Reference 9

variable attachments of the antibodies to the different tumor cells; more antibodies are attached to those cells which have significant amounts of the antigen on their surfaces but none to other tumor cells that are devoid of the specific antigen and are therefore allowed to proliferate (10). Since the monoclonal antibody alone is not cytotoxic, it usually acts as a carrier of a more cytotoxic radionuclide or toxin. This introduces a number of more complicating factors and variables, which include the combined physical, chemical, and biological properties of the antibody and radiolabel. The following is a summary of the variables directly linked with the production of the radiolabeled tumor-associated antibody for imaging and therapy (11):

1) Physical properties of radionuclides

- a) Physical half-life
- b) Gamma energies and abundances
- c) Photon yield per absorbed radiation dose
- d) Parent-daughter relationship-stable decay products
- e) Ratio of penetrating to nonpenetrating components
- f) Particle radiation (β^- , β^+ , IC, and Auger electrons)
- g) Production mode (availability)

2) Chemical properties

- a) Stability of radionuclide-protein bond
- b) Specific activity-number of labels per molecule obtainable
- c) Retention of immunological activity versus specific activity
- d) Addition of nonradioactive carrier-metal ion contamination
- e) Sample pH

- 3) Biodistribution and biological half-life
 - a) Route of administration and activity of initial dose
 - b) Vascularity: Blood flow and interstitial fluid space
 - c) Uptake of protein-bound form of the isotope
 - d) Plasma and whole body clearance
 - e) Relative size of tumor model
 - f) Size of animal or human model
 - g) Cell proliferation
 - h) Capillary and cell permeability
 - i) Presence of inflammation
- 4) Target-nontarget time-dependent ratio: dose to tumor, whole body, and other sensitive organs
- 5) Immunological purity of the antibody and its relative specificity
- 6) Characteristics of imaging system with respect to the radiolabel properties
- 7) Marketability, availability, convenience

This list, which is by no means all-inclusive, is complicated by the fact that each variable seems to be related to a number of the other variables.

Tumor Localization

The localization of radiolabeled antibodies at tumor sites is dependent on a number of factors as reported by several investigators (12-27). These include the tumor size, radiolabeling method, choice of radiolabel, type of antibody (whole vs fragment), route of administration, tumor biology (blood flow, vascular permeability etc.), and the dose administered. However, tumor uptake is ultimately dependent upon its antigen content (13).

Choice of Radiolabel

The choice of a radiolabel is dependent upon its intended use: diagnostic or therapeutic applications. For diagnostic applications, one is more concerned with the sensitivity and specificity of the test with the least radiation dose. This is obtained by the use of radionuclides with a low equilibrium absorbed dose constant. In therapy, the objective is to attain the highest differential radiation dose, which requires the use of radionuclides with a high equilibrium absorbed dose constant. The goal of both applications is to attain the highest radiation dose factor for the target site in comparison to the normal tissue (28).

Ideally, radionuclides which are particularly suited for imaging with radiolabeled antibodies should be characterized by 1) physical half-life of 6 hr to 8 days, 2) gamma energy range of 80-240 keV, 3) high single energy gamma abundance per decay, 4) small abundances and low-energy particulate radiation, and 5) reasonable radiolabeling chemical properties and stability (11). Similarly, radionuclides used for therapy should have complementary properties to the antibody-bound radionuclides used in imaging. However, their decay should be characterized with a large component of particulate radiation with little or no accompanying gamma radiation such that a high localized dose may be delivered (11). Table 2-3 lists the various radionuclides that meet the required

Table 2-3. Selected Radionuclides for Radioimmunodetection†

Nuclide	Half-life	Primary Decay Characteristics	
^{99m} Tc	6 h	IT (99%);	$\delta = 141$ keV (89%)
¹²³ I	13 h	EC (100%);	$\delta = 159$ keV (83%)
¹¹¹ In	68 h	EC (100%);	$\delta = 171$ keV (88%) $\delta = 245$ keV (94%)
¹³¹ I*	193.2 h	β^- (100%);	$\delta = 364$ keV
⁹⁷ Ru	69 h	EC (100%);	$\delta = 216$ keV (86%)
⁶⁷ Cu*	62 h	β^- (100%);	$\delta = 91$ keV (7%) $\delta = 93$ keV (17%) $\delta = 184$ keV (47%)

Selected Radionuclides for Radioimmunotherapy†

Nuclide	Half-life	Primary Decay Characteristics	
¹³¹ I‡	193.2 h	β^- (100%);	0.608 MeV (86%) $\delta = 364$ keV (82%)
⁹⁰ Y	64 h	β^- (100%);	2.29 MeV (100%)
⁶⁷ Cu‡	62 h	β^- (100%);	$\delta = 91$ keV (7%) $\delta = 93$ keV (17%) $\delta = 184$ keV (49%)
²¹² Bi	1 h	α (36%) β^- (64%)	²¹² Po (0.3 μ g \cdot sec $T_{1/2}$, $\alpha = 8.78$ MeV)
²¹¹ At	7.2 h	α (41%); EC (59%)	5.9 MeV (41%)
¹²⁵ I	144.5 h	EC (100%);	$\delta = 35$ keV x-rays = 27 keV

† Adapted from Reference 29

* Potentially useful in therapy as well

‡ Potentially useful in imaging also

specifications for diagnostic and therapeutic applications of monoclonal antibodies. Table 2-4 lists the advantages and disadvantages of the use of the radionuclides found in Table 2-3.

Technetium-99m, ^{111}In , and ^{131}I are examples of radionuclides that are currently under extensive use in medical imaging (29-34). They have the advantage of availability, well-known chemistry, and optimal half-life and gamma decay energy. Unfortunately, ^{131}I suffers from dehalogenation in vivo, which allows for nonspecific uptake of free iodine in sites other than the tumor sites, especially in the thyroid, liver and spleen (30,35). This makes identifying tumors in these organs by imaging nearly impossible. Iodine-131 also delivers a high radiation dose to normal tissues due to its long half-life and medium gamma energy (36). Indium-111 in vivo metabolism is relatively unknown, although it has been shown to have good affinity once in the tumor, but if it comes off the antibody, it will relocate to the liver, spleen, and bone marrow (30). Technetium-99m has a chemistry problem; i.e., it is difficult to obtain a stable bond between it and the antibody. Childs and Hnatowich (37) found increased stability when $^{99\text{m}}\text{Tc}$ was coupled directly to the chelate DTPA (diethylenetriaminepentacetic acid). Rhodes et al. (38) used a pretinning method to successfully label $^{99\text{m}}\text{Tc}$ directly to antibody fragments, which showed increased stability against

Table 2-4. Advantages and Disadvantages of Selected Radionuclides for Radioimmunodetection†

Nuclide	Advantages	Disadvantages
^{99m} Tc	Availability Decay energy	Short T _{1/2} Chemistry problem
¹²³ I	Decay energy Iodine chemistry	Availability Cost (\$20/mCi) Short T _{1/2}
¹¹¹ In	Decay energy Optimal T _{1/2} Chelation chemistry	In vivo metabolism
¹³¹ I	Availability Iodine chemistry Optimal T _{1/2}	Decay energy In vivo de-iodination
⁹⁷ Ru	Chelation chemistry	In vivo metabolism Availability Decay Energy
⁶⁷ Cu	Optimal T _{1/2}	Decay Energy

Advantages and Disadvantages of Selected Radionuclides for Radioimmunotherapy†

Nuclide	Advantages	Disadvantages
¹³¹ I	Availability Imaging Cost	Long tissue path
⁹⁰ Y	⁹⁰ Sr-Generator Pure β ⁻ decay	Chemistry problems In vivo metabolism?
⁶⁷ Cu	Imaging	In vivo metabolism?
²¹² Bi	High LET decay	Short T _{1/2} Unknown chemistry
²¹¹ At	High LET decay	Short T _{1/2} Unknown chemistry
¹²⁵ I	High LET decay	Must be in nucleus to kill tumor

† Adapted from Reference 29

transchelation. Recently, Goldenberg and associates (39) have reported in vivo retentions of 98% immunoreactivity in patients using anti-CEA murine monoclonal antibody (IMMU-4) Fab' labeled directly with ^{99m}Tc . Chen and colleagues (40) also have reported good results using ^{99m}Tc labeled antibodies in the confirmation of diagnosis of uveal melanoma.

Several alpha- and beta-emitting radionuclides have potential for radioimmunotherapy as seen in Table 2-3. Iodine-131 has been most commonly used and is currently being utilized in human clinical studies (35,41,42). However, the choice of ^{131}I has not been because it is the optimum for radioimmunotherapy; two-thirds of its absorbed dose equivalent is due to penetrating radiation, which usually escapes the primary tumors and their metastases (4). The Auger electrons of iodine-125 may be effective for therapy when used in conjunction with antibodies that are internalized rather than remaining on the cell surface (9).

The appeal of alpha-particles for radioimmunotherapy is their short range (~50-90 μm) and high linear energy transfer (LET) (~80 keV/ μm), which produces extreme cytotoxicity. An alpha-particle traversing the diameter of a 10 μm nucleus deposits an energy of 800 keV, equivalent to an absorbed dose of approximately 0.25 Gy (4). Potential alpha-emitting radionuclides for radioimmunotherapy are astatine-211 and bismuth-212 (Table 2-3). Experimental

trials with ^{211}At -conjugated antibodies on a murine lymphoma system are in progress by Harrison (43) and Vaughan (44). Perhaps the half-life of bismuth-212 is too short (60.6 min) to fully capitalize on the longer antibody retention in the tumor, although Macklis found it to be highly cytotoxic to the murine Thy 1.2⁺ EL-4 tumor cell line (45). More recently Simonson et al. (46) showed ^{212}Bi to be also cytotoxic to the LS174T cell line. Few suitable alpha-sources are available because most alpha-emitters are heavy elements ($A > 82$) which decay to unstable daughters. The recoil alphas produced in the decay of these daughters rupture the radionuclide-antibody bond, which allows the daughter product to diffuse away from the tumor (5).

Yttrium-90 offers another possibility for use in radioimmunotherapy and has the advantage in that it is a pure beta emitter and is easily available by production from a strontium-90 generator (Table 2-4). Unfortunately, it has no gamma emissions to allow for useful biokinetic studies in the patient and, once detached from the antibody, it deposits in the bone in sufficient quantities to give a high radiation dose to the marrow. Yttrium-90 is currently under investigation by several groups (24,47-52). Sally DeNardo and colleagues (51,53) found copper-67 to be one of the most promising radionuclides for radioimmunotherapy because of its short half-life, abundance of beta particles, and the presence of 93 and 184 keV gamma emissions.

A potential radionuclide for radioimmunotherapy, palladium-109, a predominately beta-emitting radionuclide ($E_{\max} = 1$ MeV; half-life = 13.4 h) that is available carrier-free, was investigated by Fawwaz et al. (54), who labeled it to an antimelanoma monoclonal antibody. Unfortunately, they found that at least 60% of the radiolabeled antibody preparation failed to bind to melanoma cells. They believed this was partly the result of inactivation of the antibody during purification, storage, or radiolabeling and/or the presence of carrier ^{108}Pd in the ^{109}Pd preparation. A new radionuclide for radioimmunotherapy, rhenium-186 (1.07 MeV maximum beta, 9% abundant 137 keV gamma), is being extensively evaluated in patients by Schroff and associates (55). Preliminary findings indicate it to have similar in vivo properties to $^{99\text{m}}\text{Tc}$ and is very stable in vivo.

Tumor Size Effect

Several investigators have found that tumor uptake of the radiolabeled monoclonal antibody is inversely related to the tumor size; i.e., the per gram uptake of monoclonal antibodies decreases as the tumor size increases (12-15,56,57). Pimm and Baldwin (14) have found a multitude of parameters that could potentially account for this relationship. These include changes in blood flow, degree of necrosis, levels of cellular and intratumor or extravascular antigen, and the presence of circulating tumor-derived

antigen. However, this relationship could not be duplicated by Cohen et al. (16). In fact, their findings contradicted those by other investigators, in that they found the total tumor uptake increased with increasing tumor size. No satisfactory explanation has been offered to explain the differences between the findings. Pedley et al. (57) found that for tumor weights greater than 100 mg a strong positive correlation exists between absolute uptake and tumor weight but found a poor correlation for smaller tumors. They thus concluded that specific uptake was inversely proportional to tumor size regardless of the antibody.

At present, although still controversial, one may conclude that the relationship between the tumor size and the antibody uptake is an inverse one.

Fragment versus Whole Antibody

Antibody fragments (Figure 2-4) reach their maximum accumulation faster and clear from the body faster than whole antibodies (9,17-19,29,53). However, whole antibodies remain in the tumor longer to achieve higher concentrations. Thus, the choice of antibody type depends on the application. Radioimmunoimaging would benefit most from the use of fragments, because of their early maximum accumulation and faster clearance, which results in a lower background (nonspecific uptake) level. Radioimmunotherapy would benefit most from the use of whole antibodies because

the cytotoxic effect could be delivered over a longer period of time.

The difference in tumor localization between the fragments and whole antibody has been attributed to the smaller weight of the fragments (55,000 daltons and 110,000 daltons for IgG Fab and $F(ab')_2$ respectively) compared to that of the whole IgG antibody (160,000 daltons), which allows them to transverse the intravascular and extravascular space much more quickly (53). This effect also may be the result of differences in the valency of the antibodies (9). Since Fab fragments are monovalent, their bonds to cell-bound antigens are weaker than those of the divalent whole antibodies and because of this, they shed the tumor and are rapidly cleared from the body via the kidneys (9). $F(ab')_2$ fragments, on the other hand, are divalent, but demonstrate similar kinetics to the Fab fragments. Ballou et al. (19) compared IgM $F(ab')_{2\mu}$ fragments to whole IgM antibodies. The weight of the IgM $F(ab')_{2\mu}$ fragment was 130,000 daltons, which is not considerably less than that of a whole IgG antibody (160,000 daltons). However, the IgM $F(ab')_{2\mu}$ did weigh considerably less than the whole IgM antibody, which weighed 900,000 daltons. The $F(ab')_{2\mu}$ showed a 1.6-fold faster whole body clearance and reached its maximum uptake earlier than that of the whole IgM antibody. However, its total uptake was lower than the whole IgM antibody. Ballou suggests that this may be caused in part by

differences in metabolism between the whole antibody and fragment and also possible changes in the antigen-binding of the fragments resulting from low pH digestion.

The choice of antibody type will depend upon its application. For imaging, fragments will most likely be used. The best choice seems to be $F(ab')_2$ because it remains in the blood longer than Fab fragments. This results from its larger molecular weight, which reduces its loss through the kidneys (58). For therapy, whole antibodies will probably be used. Perhaps $F(ab')_2$ fragments will prove superior in all cases, because they offer the advantages of fragments and the lack of immunogenicity of whole antibodies.

Dose Administered Effect

Eger et al. (20) found dose-dependent kinetics in 12 human patients with melanoma. They found that as the amount of injected antibody increased, the plasma half-life increased, which eventually resulted in a higher tumor uptake. They also found that the radioactivity levels in the spleen and marrow decreased as the amount of antibody increased. This dose dependent effect was also seen by Hnatowich et al. (21). Pedley et al. (57) also studied the effect of tumor weight on uptake with escalating amounts of antibody. They found that there was decreased uptake with escalating amounts of antibody in small tumors. This effect

was thought to be the result of steric hindrance in the small tumors, even though the rate of diffusion into the tumor may have increased.

Labeling Method Effect

The method used to attach the radionuclide to the antibody will affect the antibody's localization. If the method is inefficient, in that the radiolabel detaches from the antibody in vivo or if the radiolabel's radiation destroys or alters the properties of the antibody, all hope of tumor localization is lost and radioimmunotherapy is rendered useless.

Since most suitable radiolabels for therapy are metals (Table 2-3), early methods of antibody labeling attempted to attach them directly to the antibody. This proved to be highly unstable and the radiolabel detached from the antibody in vivo (9). However, nonmetals, such as iodine, are currently being attached directly to the antibody by the Iodogen or Chloramine-T methods (22). These elements also suffer from instabilities and tend to dehalogenate in vivo (18). The latest methods employ the use of a coupling agent, usually a chelate, to attach the metallic radiolabel to the antibody (9,21,23,24). The most widely used chelate is diethylenetriaminepentaacetic acid (DTPA). The antibody is attached to the DTPA which, in turn, is attached to the radiolabel. The bonds formed with the DTPA are much stronger

than those of the direct-attachment method (23); thus the chelate-coupled antibodies are much more stable in vivo (53). Another advantage to using a chelate such as DTPA is that many different chelate substitution levels on the antibody can be achieved by straightforward manipulation of the relative amounts of reactants or time of reaction with the antibody (53). Other chelates have also been used and their effects on the antibody biodistribution are continually being investigated (59-62).

Dose Administration Route

The site where the antibody is administered affects not only how fast the antibody reaches the tumor, but also how much eventually localizes in the tumor (17,25). Obviously, if one is interested in localization in the lymphatic system, intralymphatical administration will prove superior to the other routes (25). If there are ascites in the peritoneal cavity, intraperitoneal administration would prove superior over the other routes. Hnatowich et al. (47) concluded that the use of intraperitoneal rather than intravenous administration may be important in the application of yttrium-90 because it probably offers a means of reducing radiation exposures to the bone marrow and the critical organ without reducing exposure to the tumor within the peritoneum. Larson (17) found that the concentration of radiolabeled antibodies in human tumors is tenfold less

after administration via the intravenous route than after injection either subcutaneously, intralymphatically, or intraperitoneally.

Tumor Biology

Tumors grow radially from a central group of cells; therefore as the tumor enlarges, the dividing cells form a shell around a relatively hypoxic core. When these cells outgrow their blood supply, they die and form a necrotic central nest containing some viable cells that are highly resistant to radiation (26). Blood flow in this situation is low which makes delivery of the radiolabeled antibody to the tumor very difficult. Studies by Gullino and Grantham found that the average value of blood supply to tumors was 0.14 ± 0.01 ml per hour per mg of nitrogen and the blood supply was independent of the host (27). Solid tumors were also found to be angiogenesis dependent by Folkman (63). The radiolabeled antibody must reach the tumor through circulation, crossing the capillary wall and diffusing throughout the interstitial fluid to reach the tumor cells. The rate of diffusion across these barriers is slowed by the large size of the antibody molecule (64). This diffusion rate has, according to Winchell (65), an 18 to 24 hour half-life. Diffusion of the labeled antibody from the vascular compartment into the tumor is caused by the concentration gradient between the blood and the tumor (26). The higher

the concentration of radiolabeled antibody in the blood compared with the tumor, the higher the diffusion rate will be. Leichner et al. (66) found that external-beam irradiation increased the permeability of tumor vascularity, which resulted in increased tumor uptake of radiolabeled antiferritin.

Other Factors

Other factors may influence the localization of radiolabeled monoclonal antibodies in the tumor, such as the amount of circulating antigens in the vascular system and the metabolism and catabolism of the antibody in vivo. Circulating antigens in the blood may combine with circulating labeled antibodies. This complex could be phagocytized by the reticuloendothelial system to reduce the number of labeled antibodies that reach the tumor site (67,68). Pimm and Baldwin (69) found that the average rate of catabolism of ^{125}I -labeled-IgG₁ anti-CEA monoclonal antibody was 1.64% of the administered dose per gram per 24 hours and that this rate was higher for tumor bearing mice as opposed to nontumor bearing mice. They also concluded that tumor localization by the labeled antibody is a dynamic process with simultaneous localization and degradation. Gatenby et al. (70) have shown that the level of oxygen in the tumor or tumor region also affects the antibody localization. They found that tumors or tumor regions with a

mean oxygen pressure of 16 mm Hg or less had lower antibody uptake, even when the presence of antigen was confirmed by biopsy. This suggests that physiological factors other than antigen expression may affect antibody uptake. In the past few years a factor that has become increasingly important because of the increase in the number of human studies is the development of human anti-mouse antibodies (HAMAs). The body, in response to the injection of murine antibodies, produces antibodies (HAMAs) against the murine antibody which it recognizes as being foreign. This response can be detected within one week of exposure to the mouse protein and is maximal within 2-3 weeks of exposure (71). The timing and detection of the HAMAs are influenced by the dose of the mouse antibody administered (71). HAMA clearly alters the pharmacokinetics of subsequent murine antibody infusions and, depending on the dose of the murine antibody and titer of HAMA, can interfere with radioimaging and therapy and can lead to toxicity because of the immune complexes and their redistribution (71). Scannon (72) found a rapid clearance of the infused murine antibodies from the blood which limited further administration. It has been suggested that antibody fragments be used instead of whole antibodies, because they lack the Fc region (Figure 2-4), which most likely triggers the allergic response. Other approaches to reducing HAMA include the use of chimeric (human-mouse) monoclonal antibodies, chemical alteration of the murine Fc portion,

ultrapheresis of human plasma to remove Ig, and chemical suppression of the immune response.

From the above discussion, one may conclude that the localization of radiolabeled monoclonal antibodies at the tumor site is dependent upon a number of seemingly interrelated variables which may vary from patient to patient. Larson (25) also concluded that tumor localization varied considerably from patient to patient.

CHAPTER 3

RADIATION DOSIMETRY

Before radioimmunotherapy can be implemented successfully, it is necessary to know the amount of radiation absorbed by the target and nontarget tissues. This has proved to be difficult because of the lack of appropriate methods to measure the amount of radiation absorbed in the tissues; i.e., the absorbed dose, which was deposited there by radiolabeled antibodies. The lack of an appropriate method for correlating non-uniform dose with effect has also hindered the efforts to assess the absorbed dose. Assessment of the absorbed dose is complicated by the large number of interrelated factors that affect the localization of the radiolabeled antibodies in vivo (see Chapter 2). These factors require that the calculated absorbed dose be patient-specific. The current methods used to calculate absorbed dose are based on assumptions that are not valid when radiolabeled antibodies result in a nonuniform distribution are used.

Current dosimetry methods can be divided on the basis of the approach taken to calculate the absorbed-dose. There are three basic approaches (73): (a) those that utilize the conventional Medical Internal Radiation Dose Committee (MIRD) formulation, a macroscopic approach which was developed to cater mainly to diagnostic situations usually involving gamma emitters and whole organs rather than discrete targets (74); (b) those that utilize Berger's point kernels, a semi-microdosimetry approach which considers small size targets but not very low energy emissions at the level of cell dimensions (75); and (c) those that take a microdosimetric approach, which investigates doses from short range emissions located near the cell surface or cell nucleus (76).

Since absorbed dose is defined as the amount of energy deposited per unit mass by ionizing radiation at the site of interest (77), dosimetry calculations require a knowledge of the physical properties of the radiolabel, length of time the radioactivity remains in the various sites, and the distribution of the radionuclide to the various sites in the body (28,78,79). The physical properties of the radiolabel are perhaps the easiest to determine accurately and will be known in detail if conventional labels are used (80). The residence time and spatial distribution of the radiolabeled antibody in vivo are not usually known and must be determined prior to radioimmunotherapy. These parameters

are usually determined by sequential, timed quantitative imaging. Several investigators (10,11,78) have suggested that a diagnostic study, as such, be performed prior to radioimmunotherapy. In this diagnostic study, the antibody would be labeled with a small amount of the therapeutic agent or a short-lived isotope of the therapeutic agent in an effort to reduce the hazard to the patient (69).

Medical Internal Radiation Dose Committee (MIRD) Formulation

The MIRD Formula (74) is the most widely accepted method for calculating radiation absorbed dose from internally deposited radionuclides. This method was recommended by the Medical Internal Radiation Committee of the Society of Nuclear Medicine in 1968 and was later adopted for standard use by the International Commission on Radiation Units (ICRU) (81) in 1971. MIRD is based on the dose rate equation developed by Loevinger et al. (82) in 1956 and is expressed as

$$\text{Dose rate to target} = K \times \frac{\text{activity in target}}{\text{mass of target}} \times \frac{\text{energy of emission}}{\text{absorbed fraction}} \quad 1)$$

where K is a constant which depends on the units used.

Several assumptions are made in this approach, the most important in the present context being that in applying this method to humans, an anthropomorphic phantom is used, which in calculating the absorbed dose, does not take into account

the nonuniformity of the activity distribution. Thus, source homogeneity is assumed throughout the organs. Humm (4) gives two reasons why this assumption may not necessarily be valid in the case of radioimmunotherapy. First, the irregular nature of the tumor vasculature will result in a complex pattern of diffusion gradients guiding the antibodies through the tumor. Second, immunohistochemical studies with antibodies have shown that the tumor antigens may not be expressed uniformly throughout the whole tumor cell population.

For the application of radioimmunotherapy, and assuming that the activity remaining in the body after organ uptake is distributed uniformly, the mean dose to the target (tumor) is the sum of three components: a) the dose from nonpenetrating radiations (radiation pathlength is smaller than the dimensions of the organ in which it resides) emitted within the target organ, b) the dose from penetrating radiations (radiation pathlength is greater than the dimensions of the organ in which it resides) emitted within the target organ, and c) the dose from penetrating radiations emitted by the activity in the rest of the body (41). The absorbed fraction for nonpenetrating radiations is assumed to be unity; i.e., all the energy emitted by the source organ is absorbed in the source organ. With this in mind, one proceeds to calculate the various parameters of the MIRD equation for each component. The effective half-

time can be calculated from exposure rate measurements and activity measurements of the blood and urine as a function of time. Decay constants are calculated from a least-squares fit of the time-varied target organ count rates.

Compartmental modeling is often employed to calculate the cumulated activity, decay constants, and the other parameters needed for the MIRD equation. Tumor and critical organ volumes are determined from Computed Tomography (CT) or Single-Photon Emission Computed Tomography (SPECT) images.

For conventionally employed radionuclides such as ^{131}I , ^{32}P , or ^{90}Y and for targets greater than a centimeter in diameter, the MIRD method holds quite reasonably (73).

Berger's Point Kernels

This method is based on Berger's Point Kernels for calculating the absorbed dose from beta-rays (75). If the medium is assumed to be uniform and unbounded, the beta-ray dosimetry problem can be divided into two separate parts: a) determination of the distribution of absorbed dose around a point isotropic source, which is often referred to as a point kernel, and b) appropriate integration over the point kernel weighted by the source density to obtain absorbed-dose distributions for extended sources (83). Part a) contains all the physical aspects of the problem and part b) is entirely geometric. Using the principles of

superposition, the absorbed dose from one source element can be added independently to the contribution from another source element. Thus, a distributed radionuclide source can be considered as a collection of independently acting isotropic sources (83).

The beta-ray dose rate is expressed in the form

$$R_{\beta} = 1.38E-05 E_{\beta} \phi A \quad \text{Gy d}^{-1} \quad 2)$$

where R_{β} is the beta-ray dose rate in the tissue, E_{β} is the average beta-ray energy per disintegration in Mev, ϕ is the isotropic specific absorbed fraction, and A is the Activity of the radionuclide in Bq.

Since the dose rate is proportional to the average concentration, the total beta-particle dose is obtained by integrating the concentration over the time the tissue is exposed to the beta particles:

$$D_{\beta}(t) = \int_0^t R_{\beta}(t) dt = 1.38E-05 E_{\beta} \phi \int_0^t A(t) dt \quad \text{Gy} \quad 3)$$

where E_{β} is in Mev, t is in days, and A is in Bq. Thus, whenever the average activity $A(t)$, is known as a function of time, the absorbed dose can be computed by integration.

Loevinger et al. (82) states that for purposes of dosimetry, the tissue distribution can be represented by a stable system of separate compartments interconnected by first-order reactions. First-order reactions imply that the

total amount of radioactivity leaving a given compartment per unit time is proportional to the amount present. The rate of change of the total radioactivity in the i th compartment is described by the following differential equation:

$$\frac{dq_i}{dt} = -\lambda_p q_i - k_{i0} q_i + \sum_{j=1}^n (k_{ji} q_j - k_{ij} q_i) \quad 4)$$

- q_i = total radioactivity in the i th compartment
 k_{ij} = constant fraction of the radioactivity in the i th compartment transferred to the j th compartment, per unit time
 k_{i0} = constant fraction of the radioactivity in the i th compartment transferred to outside the system (excretion)
 λ_p = radioactive decay constant
 n = number of compartments

The first term on the right represents the loss due to radioactive decay, the next term the loss from the system by excretion or fixation, the first term inside the bracket represents the contribution of the $(n-1)$ other compartments to the i th compartment, and the second term inside the bracket represents the loss from the i th compartment to the $(n-1)$ other compartments. Integrating this equation for q_i (μCi) and then dividing by the mass (g) of compartment i gives the average concentration of radioactivity in the i th compartment:

$$C_i(t) = 3.7 \times 10^4 q_i(t)/m_i \quad \text{Bq g}^{-1} \quad 5)$$

Thus, it is now possible, using Equation (5), to calculate the total beta-particle dose from Equation (3). Spencer (84)

showed the applicability of this method in radioimmunotherapy.

A whole range of electron energies from 10 keV to over 1000 keV, as well as tumor sizes from single cells to 10^7 cells (each having a millimeter diameter), can be encompassed with this approach.

Microdosimetry

Microdosimetry is most applicable for evaluating dose-effect relationships. It uses the microscopic distribution of radiation interactions with biological systems to explain the effects of radiation on the system (76). In some instances, the distribution of specific energy in small targets, individual tracks, or even individual energy absorption events such as single ionizations may be needed to obtain meaningful dose-effect relationships.

Microdosimetry takes into account the statistical aspects of the particle track structure, energy distribution patterns, and radionuclide distribution within tissues and provides a means for determining the number and frequency of cells irradiated, the probability densities in specific energy, and the average dose delivered to cells of interest (85). Charged-particle radiation interacts with atomic electrons of the matter through which it passes, and ionization and/or excitation energy is imparted with each interaction. The charge and mass of the particle, its initial energy, and the

matter through which it travels determine the pattern of energy loss, the distance traveled, and the direction taken by the particle. Ionizations and excitations are produced when the energy is transferred from the particle to the medium.

The basic quantity that describes the energy imparted to matter is the absorbed dose, which actually is a mean value. By definition, the absorbed dose D is the quotient of $d\bar{e}$ by dm , where $d\bar{e}$ is the mean energy imparted by ionizing radiation to matter of mass dm (86):

$$D = d\bar{e}/dm \quad 6)$$

The specific energy, z , a stochastic quantity with units similar to absorbed dose, is defined as the quotient of e by m , where e is the energy imparted by ionizing radiation to matter of mass m (86):

$$z = e/m \quad 7)$$

The mean absorbed dose in a volume is equal to the mean specific energy z , in the volume:

$$\bar{D} = \bar{z} \quad 8)$$

The ratio e/m is highly dependent upon target size. As the target size gets smaller and smaller, the variations in the local dose becomes increasingly greater, and the average dose value becomes less and less indicative of the complete

dose distribution (85). Thus, for very small target sites, the concept of absorbed dose becomes increasingly abstract, and the dose is better represented by a distribution of doses in "specific energy". For a given value of target size mass, this distribution is called the "probability density in specific energy" and is denoted by $f(z)$. The probability that the specific energy received by a target site lies in the infinitesimal range dz containing the value z is $f(z)dz$.

Methods for calculating the probability densities in specific energy can be divided into four steps (85). The first step involves characterizing the geometrical relationship between the radioactive source distribution and the target sites. Second, the density in specific energy must be determined for a target at any distance from the radioactive source and with all possible angles of intersection considered. Third, the probability that a point source exists at any given distance from the target must be determined from the spatial distribution of sources. And fourth, the densities from all point sources are convolved using Fourier transforms to construct a new specific energy density for the target population.

The product of a microdosimetry calculation is a statistical distribution of doses to small sites from which an average dose could be determined. The precise relationship between the specific energy density (average dose) and the resulting biological effects is not known;

therefore, the results from this approach are not directly applicable to the rather different conditions found in radioimmunotherapy. However, several investigators (85,87-91) have proceeded to utilize this method for radiolabeled antibody dosimetric calculations.

Critical Organs

The maximum radiation doses that radiosensitive organs can tolerate and still continue to function adequately to support life are listed in Table 3-1 (10). With current systemic approaches to therapy, bone marrow toxicity has been the dose-limiting side-effect (92). However, as shown by in vivo radiolabeled antibody biodistribution studies, the dose-limiting organ is most likely to be the liver or kidney.

Table 3-1. Sublethal Radiation Doses[†]

Organ System	Dose (Gy)
Bone Marrow	< 2
Intestinal Mucosa	< 7
Kidney	< 15
Liver	< 25

[†] Adapted from Reference 10

Leichner et al. (41), using the MIRD methodology, found that the ¹³¹I radiation dose for four patients ranged from four to 10 Gy for the liver and from 1.1 to 2.2 Gy for total-body

irradiation. Vaughan et al. (93), using Berger's Point Kernels, found that a tumor dose of two Gy in one week with ^{131}I was associated with a whole-body dose of 17 Gy. Bigler et al. (87) utilized a microdosimetric approach to calculate the mean dose to the red marrow for a number of different radiolabels. The mean dose ranged from 1.6 Gy with ^{73}As to 17 Gy with ^{131}I for a large cell size.

In recent years with the advent of new materials technology, Griffith et al. (94-95) and Wessels (96) have developed a method for the direct measurement of absorbed radiation dose through the use of teflon-embedded, $\text{CaSO}_4:\text{Dy}$ thermoluminescent dosimeters (TLD)*, which have been modified to fit inside a 20-gauge needle. The TLDs are directly implanted into the tissue of interest and are subsequently recovered for read-out. They measured an absorbed dose of 8.1 Gy for the ^{131}I labeled B72.3 colorectal carcinoma mouse system and 17.4 Gy for the ^{131}I labeled LYM-1 Raji B-cell lymphoma mouse system, which correlated well with autoradiography measurements (95). This method is not appropriate for human dosimetry studies because of patient discomfort and tissue trauma.

In order for radioimmunotherapy to be successful, the radiation dose deposited in the tumor and other critical organs must be known accurately. Current dosimetric methods do not adequately address the unique features proposed by

* Teledyne, Inc., NJ.

the use of radiolabeled antibodies for the calculation of absorbed dose. Therefore, new methods must be created. As more clinical information using radiolabeled antibodies becomes available, a better method may be defined, which can be compared to direct measurements.

CHAPTER 4

MATERIALS AND METHODS

In this research, a foundation for a dosimetry methodology to determine the absorbed dose in both target and nontarget tissues using uniformly and nonuniformly distributed activity has been developed. The calculation of absorbed dose can be divided into two parts: 1) the determination of the radionuclide concentration, and 2) the determination of the amount of energy deposited in the tissues of interest. This new dosimetry methodology uses Single-Photon Emission Computed Tomography (SPECT) to determine the radioactive uptake in the tissues and a Monte Carlo method to determine the amount of energy deposited in the tissues.

The research method utilized in this research is shown in Figure 4-1. In this figure, the research method is divided into three models: 1) the SPECT Model, 2) the Monte Carlo Model, and 3) the Dosimetry Model. Results from the SPECT and Monte Carlo Models are utilized in the Dosimetry Model.

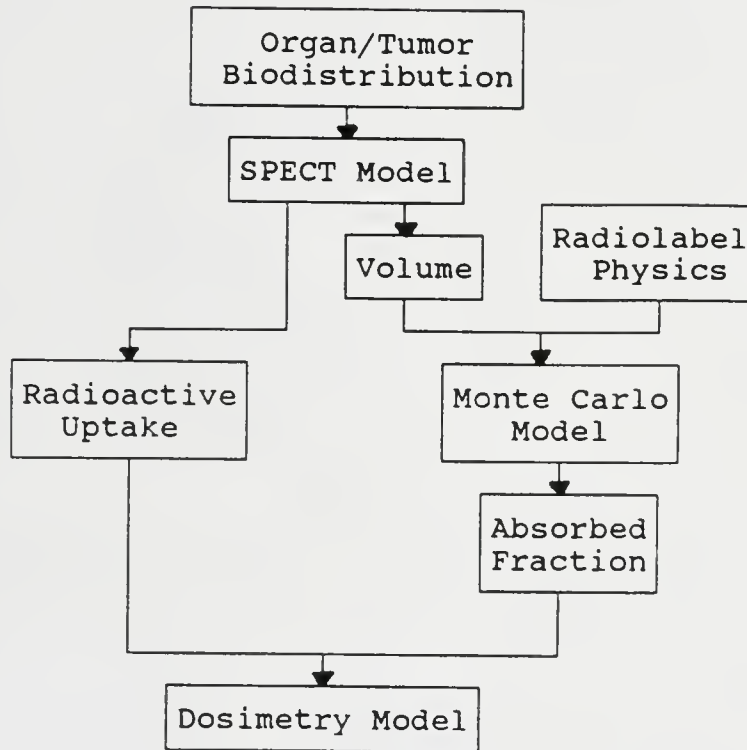


Figure 4-1. Research Methodology

SPECT Model

The SPECT Model employs the use of Single-Photon Computed Tomography, a diagnostic imaging technique, to determine the volume and radioactive uptake in the target and nontarget tissues following injection of radiolabeled monoclonal antibodies. A computer program, SPECTDOSE, was written to calculate both target and nontarget tissue volumes and radioactive uptake. SPECTDOSE uses edge detection and contour tracing algorithms to determine the volume of the various organs and tissues of interest. The SPECT image is divided into several three-dimensional arrays of a preselected size and number. Sixty-four arrays composed of 64 x 64 elements (pixels) are utilized in this research. Each element of the array represents an image volume (voxel) at a specified location. Each voxel contains an integer value derived from the measured activity in the imaged object. The total number of voxels and their location, image intensity per voxel, and organ volume (total number of voxels at a specified location) are determined in this model. Results of this model are used in the Monte Carlo Model.

Monte Carlo Model

This model uses a monte carlo method to calculate the fraction of photon energy deposited per unit mass of target and nontarget tissues (specific absorbed fraction). A monte

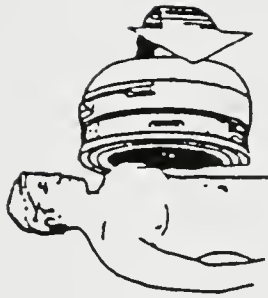
carlo computer program was obtained from Oak Ridge National Laboratory, Oak Ridge, Tennessee (97). This program, called ALGAMP, is a photon transport code which accurately simulates the physical phenomena of the photon by the use of the statistical nature of radioactivity. In ALGAMP, the human body and organs are represented by a set of mathematical equations known collectively as the Cristy Parametized Phantom (98). The radioactive distribution within each organ is assumed to be homogeneous in the Cristy Parametized Phantom. ALGAMP was modified for use in this research by the deletion of the Cristy Parametized Phantom and the addition of a method which permits the direct use of the voxel information created by the SPECT Model. The voxel information generated by the SPECT Model defines the organ volumes and locations of interest. In the dose calculation each voxel value represents the heterogeneous radioactivity distribution found in the organs following the use of radiolabeled monoclonal antibodies. By use of the SPECT image voxel information and the monte carlo simulation method, the amount of photon energy deposited per tissue mass, specific absorbed fractions, can be determined for each organ volume and voxel. The specific absorbed fractions are utilized in the Dosimetry Model.

Dosimetry Model

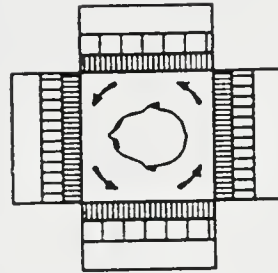
The Dosimetry Model uses the results of the SPECT and Monte Carlo Models to determine the absorbed dose to both the target and nontarget tissues. Voxel matrix values of the tissue volumes determined in the SPECT Model are utilized in the Monte Carlo Model to determine the specific absorbed fractions in the tissues of interest. The Dosimetry Model combines the specific absorbed fractions with the organs' radioactive uptake determined in the SPECT Model to calculate the absorbed dose. The absorbed dose is determined for both the organ and organ voxels; i.e, the absorbed dose can be calculated for each organ voxel also. The Dosimetry Model retains the concepts of the MIRD Method in addition to accounting for the heterogeneous distribution of radioactivity exhibited in the organs and organ voxels following the injection of radiolabeled monoclonal antibodies into humans.

Single-Photon Emission Computed Tomography

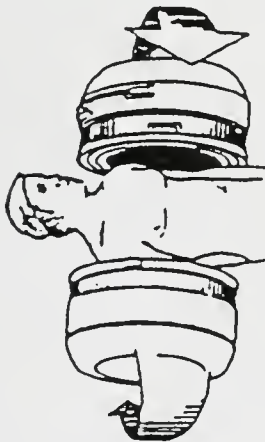
Single-Photon Emission Computed Tomography (SPECT) is a diagnostic imaging technique utilized in nuclear medicine, in which, the differences in radioactive distribution of internally administered radionuclides are exploited (99). In SPECT, the detector, a gamma camera, rotates around the patient while acquiring data (photon detection) (Figure 4-2). With the use of a computer and several complicated



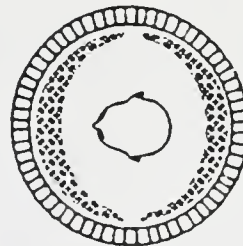
Single-Head SPECT
Gamma Camera



Single-Head SPECT Unit



Dual-Head SPECT
Gamma Camera



Multi-Detector Head
SPECT Unit

Figure 4-2. Single-Photon Emission Computed Tomography*

* Adapted from Reference 100

algorithms, the data is reprojected (reconstructed) into a transverse section image (slice) of the activity distribution. Basically, SPECT maps the three dimensional concentration of a radionuclide by measuring the angular distributions, or projections, of gamma ray intensities emitted within the body. SPECT is also capable of eliminating overlying and underlying source activities and offers the potential for quantitating the radioactive uptake in the patient (100)

SPECT Quantitation

SPECT quantitation of radionuclide activities in the human body is affected by several physical and instrumental factors including absorption attenuation of photons in the patient, Compton scattered events, the system's finite spatial resolution, and object size, finite number of detected events, partial volume effects, the radiopharmaceutical biokinetics, and patient and/or organ motion. Other instrumentation factors such as calibration of the center-of-rotation, sampling, and detector nonuniformities will affect the SPECT measurement process (100,101,102). Several of the major factors that affect quantitation with SPECT systems are as follows (100):

- 1) Physical Factors:
 - a) Characteristic energy of the emitted photons
 - b) Radiation decay as a function of time

- c) Attenuation of gamma photons within the patient
 - d) Inclusion of scattered photons within pulse height window
- 2) Anatomical/Physiological Factors:
- a) Source size and location within the body
 - b) Patient and/or organ motion
 - c) Biokinetical behavior of radiopharmaceutical within the body
- 3) SPECT System Factors:
- a) Camera/collimator energy and spatial resolutions
 - b) Detection efficiency
 - c) Changes in collimator geometric response with distance from the collimator surface
 - d) Sensitivity variations across the camera surface
 - e) Camera electronic variations, ADC errors, and gantry mechanical variations with time and/or position
 - f) Characteristics of reconstruction process such as shape of filter function, linear and angular sampling interval values, accuracy of attenuation, nonuniformities, and scatter compensation methods and accuracy of edge-detection methods

Their relative importance depends on the type of quantitative information desired and the biokinetic properties of the radiopharmaceutical. The determination of radionuclide concentration as a function of time for small volume elements (voxels) within the body is affected most by the factors listed above.

Photon Attenuation

The determination of the radionuclide concentration as a function of time in the voxel elements is affected by the

absorption attenuation and scattering of photons. The effect of attenuation results in a decrease in the measured gamma ray intensity. There is self-attenuation in the source organ and also attenuation in the surrounding body tissues. Most attenuation compensation methods assume that the attenuation coefficient, the fraction of the gamma-ray beam attenuated per unit thickness of absorber (103), is constant. Although this will provide a less accurate compensation within regions where the value of the attenuation coefficient is variable, it is the method utilized in this research. Other attenuation compensation methods, those which do not assume a constant attenuation coefficient, can be divided into three classes: 1) Preprocessing Methods, 2) Intrinsic Compensation Methods, and 3) Postprocessing Methods (100).

Preprocessing methods attempt to correct the projection data prior to image reconstruction. These methods are relatively easy to implement, however, they tend to generate streak artifacts in the presence of noise. This method was not used in this research because the antibody SPECT images were very noisy.

Intrinsic compensation methods integrate attenuation correction directly in the reconstruction algorithm. An attenuation map is measured (by using a transmission source) or assumed as part of the reconstruction algorithm. These methods require the use of large computers and are time

consuming, thus preventing the use of this method in this dissertation.

Postprocessing methods apply attenuation correction after the image reconstruction has completed. This approach is used most often in commercial SPECT systems and requires the measurement or estimation of the patient's body contour. In the human studies undertaken in this research, the patient's body contour was not retained, which precluded the use of this method in this research. The area of attenuation compensation in SPECT is currently undergoing extensive analysis and the reader is further directed to a number of reports on this subject (104-119).

Photon Scatter

Compton scattering events degrade the image contrast resulting in a major source of error in the quantification of radionuclide concentrations. Scattered photons can contribute as much as 50% of the total collected events in SPECT (120). The use of a sodium iodine-thallium doped detector in SPECT systems results in the inclusion of both scattered and nonscattered photons in the photopeak energy window. Several approaches have been attempted to compensate for the scattered radiation, but none at this point have proven to be of substantial value (100,101,102,121-130). No scatter correction method was utilized in this research.

SPECT Camera System

SPECT was performed with a digital rotating gamma camera* with a medium energy collimator and a 20% peak energy window. A rotation of 360°, 128 projections (2.81° apart), and a study of 26 minutes (12 s view⁻¹) was used. Data was acquired on a computer** in the 64 x 64 x 16 bit mode (131). After acquisition, the raw image data is reduced from 16 bits to 8 bits using the system software***. After which, the data is prefiltered using a Gaussian filter of the 24th order and a frequency cutoff of 0.20 (131). This data is reconstructed using the high resolution reconstruction algorithm, which is an iterative reconstruction method (132,133), with one iteration and a dampening factor of 0.5 (134). The dampening factor indicates the level of contribution by the error image to the production of the iterative transverse slices (135). Sixty-four transaxial slices, one pixel thick, are created. The size of the elemental voxel is one pixel in the x and y axis (transaxial plane) and in the z direction (parallel to the axis of rotation). One pixel was determined to be equal to 6.9 mm in the patient studies.

* Technicare Omega 500, Technicare Corporation,
Cleveland, OH 44139

** ADAC DPS-3300, ADAC Laboratories, San Jose, CA 95138

*** ADAC Laboratories Version 4 System Software, San
Jose, CA 95138

Image Segmentation

Prior to determining the organ volumes, the SPECT image must be segmented into the respective organs. Image segmentation is the process of subdividing an image into its constituent parts or objects. Segmentation algorithms are generally based on two properties of the image gray-level values: discontinuity and similarity. The gray-level value is an integer that represents the image intensity. In the discontinuity category, the image is partitioned on the basis of abrupt changes in the gray level. Detection of points, lines, and edges are of principle interest in this category. In the similarity category, the image is divided on the basis gray level similarities. Approaches to the similarity category include thresholding and region growing (136). Several segmentation or edge detection methods were attempted prior to the selection of the Threshold Segmentation Method in this research.

The Gradient Method, an approach that looks for discontinuity, was attempted first. It is assumed in this method that the regions of interest are homogeneous so that the transition between two regions can be determined on the basis of gray-level discontinuities alone. A local derivative operator is determined, whereby the magnitude of the first derivative indicates the presence of an edge and the sign of the second derivative determines where the edge pixel lies; the background or object side (137). Since the

first and second derivatives must be determined for each image pixel, this method is computationally intensive.

A second approach, Histogram Segmentation Method, was also attempted. This technique creates a histogram of the gray-level contents of an image. The image is subdivided into its constituents by use of the peaks and valleys in the histogram, which represent the image object and background regions respectively. Division between objects is difficult when a deep valley or steep peak is not present (138). In the presence of image noise, differentiation between peaks and valleys is futile. Because of noisy SPECT images this method was not used in this research.

The last approach attempted and used in this research is the Threshold Segmentation Method. This technique segments on the basis of gray-level similarity. A threshold value is applied to the image, whereby any image pixel's gray-level value that is greater than the threshold value is considered to be a part of the object and any pixel with a gray-level less than the threshold value is apart of the background. Since the threshold depends only on each pixel's gray-level, it is called global (139). This method was selected because of its easy implementation, small computation requirements, and excellent results when used with noisy images.

Program SPECTDOSE

The Program SPECTDOSE was developed in this research to calculate the necessary parameters proposed by the SPECT Model; i.e., organ volumes and radioactive concentrations (Figure 4-3). This program is written in Fortran-77 for a VAX/VMS Operating System. The Program SPECTDOSE is divided into a number subroutines (Figure 4-4). Before the SPECT image could be utilized, its data format or the way the image data was written to the file had to be determined. The data format for the SPECT images was obtained with a promise of confidentiality from the ADAC Corporation (140). The reconstructed SPECT image data is stored in each voxel as hexadecimal (base-16) numbers. The main program reads the hexadecimal numbers into a logical array, where the values (image count) are scaled between 0-255 intensity levels (gray-levels) and read into an integer array. The resulting reconstructed image data is represented as an interger which has a value between 1 and 256. The image count can be corrected for attenuation and radioactive decay at this point by entering the appropriate linear attenuation coefficient, radionulide half-life, and time of decay values into the program. The image threshold value is entered and the subroutine THOLD is called to segment the image into its constituent objects. This process is repeated for each image slice.

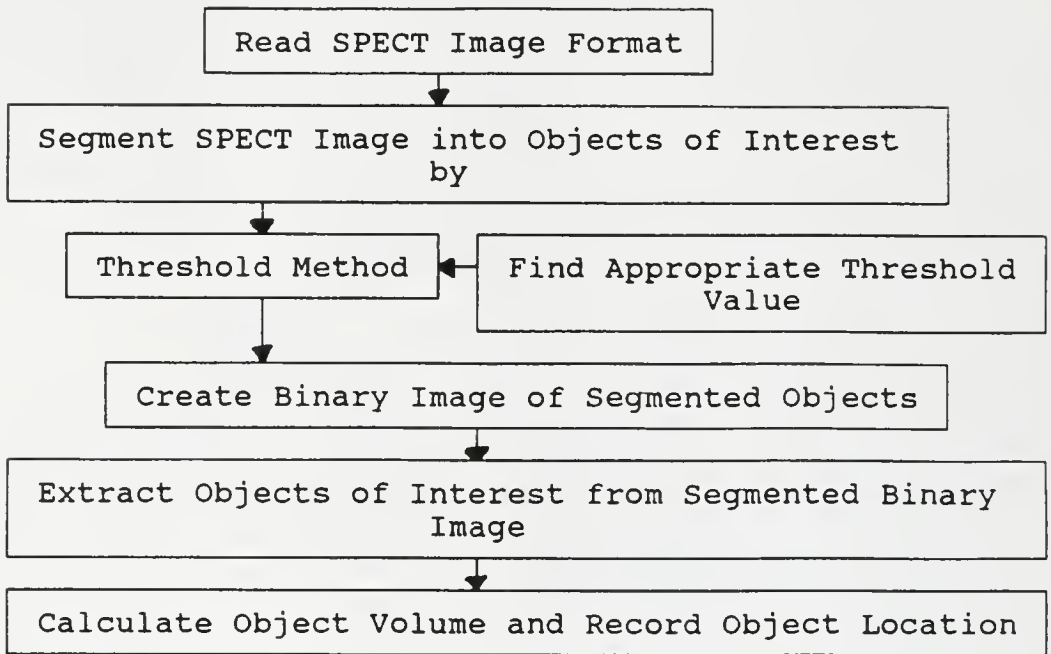


Figure 4-3. SPECT Model Flow Chart

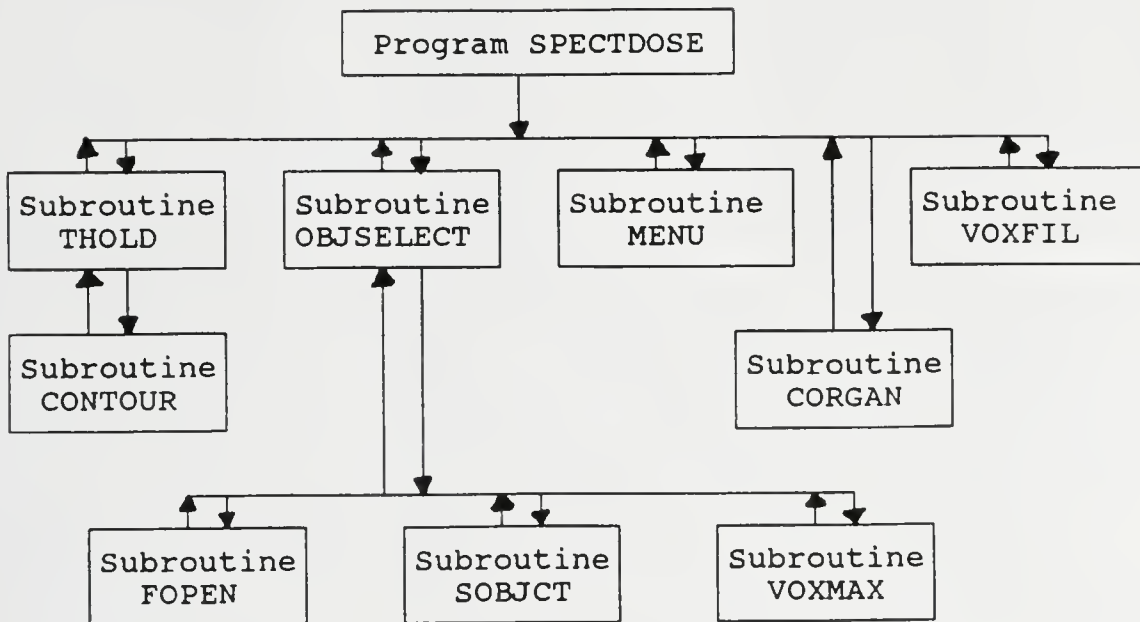


Figure 4-4. SPECTDOSE Program Subroutine Flow Chart

Subroutine THOLD

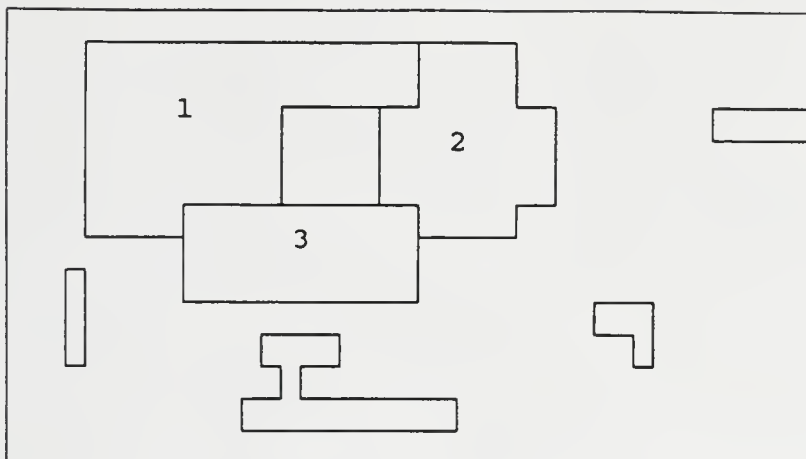
The subroutine THOLD segments the image into various objects using the Threshold Segmentation method (139) (Figure 4-5). The objects are separated from the background pixels by comparing their intensity values with a global threshold value; all pixels with an intensity value higher than the threshold belong to the object. The subroutine CONTOUR is called to extract the objects from the segmented image.

Subroutine CONTOUR

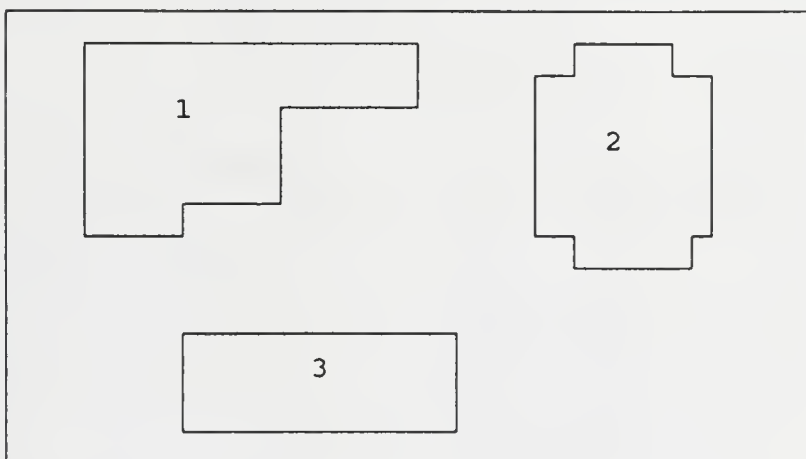
The subroutine CONTOUR extracts the objects from the segmented image (Figure 4-6). The extracted object's boundary is traced and the resulting object is stored in a binary file called OBJECT#.DAT. This process is repeated for all objects in the segmented image. Each object file is assigned a consecutive identification number; i.e., Object1.dat, Object2.dat etc. (Figure 4-7). The extracted object's characteristics, which include the number of voxels, total count, maximum and minimum indices, volume, and area, are written to the file, OBJVAL.DAT.

Subroutine OBJSELECT

The subroutine OBJSELECT integrates the extracted objects of each slice into a single object; i.e., organ. The extracted object that best represents the shape of the organ of interest is determined. This object's, the selected object,

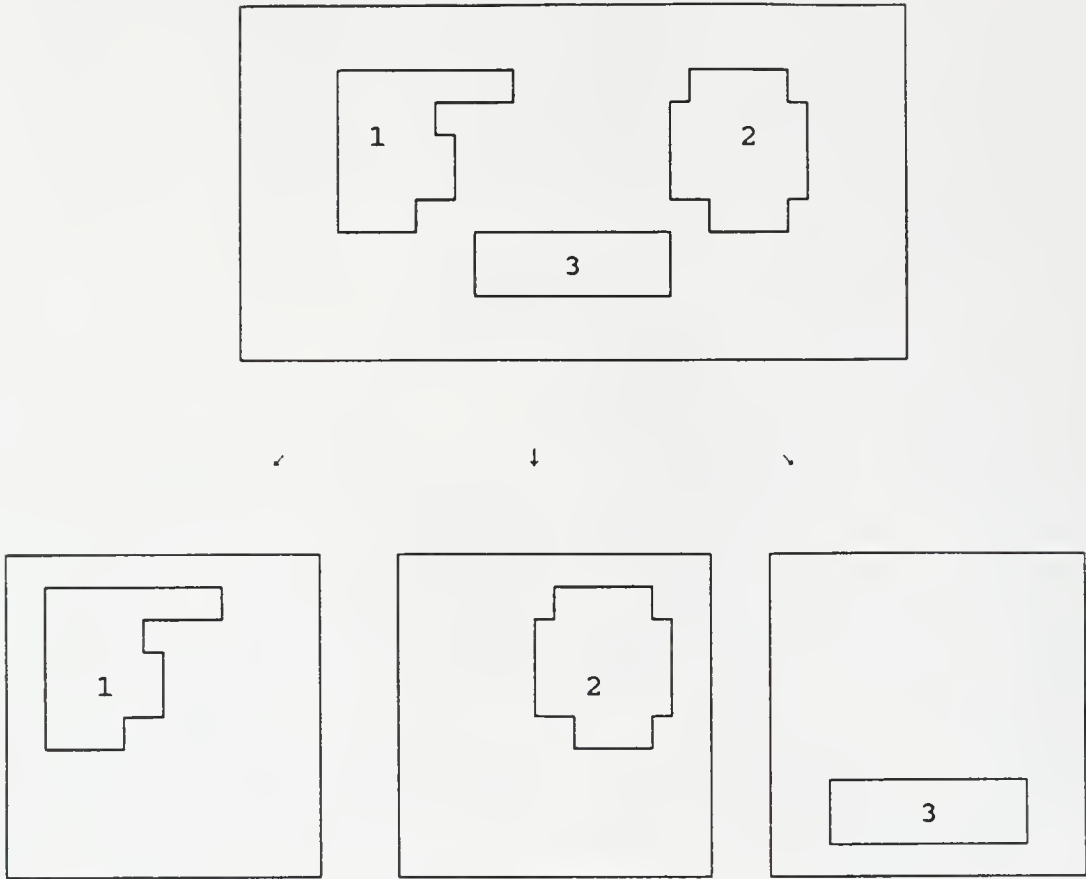


↓



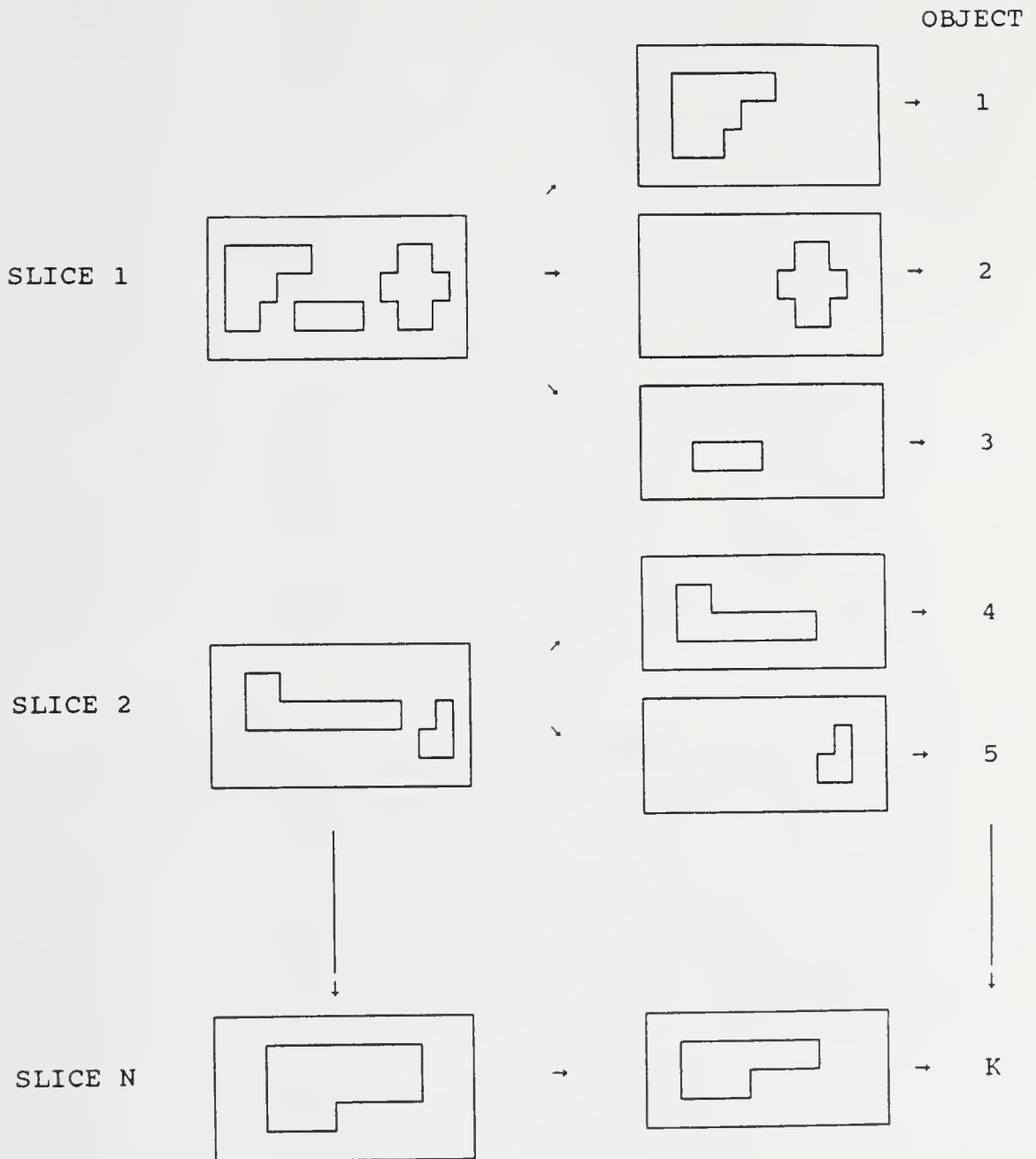
Objects are separated from the background in the SPECT image using the Threshold Segmentation Method, which is implemented in Subroutine THOLD.

Figure 4-5. Illustration of Subroutine THOLD Object Segmentation



Segmented objects are extracted and separated into separate files by Subroutine CONTOUR

Figure 4-6. Subroutine CONTOUR Object Segmentation



Segmented objects from each image slice is extracted and separated into separate files and assigned file names in consecutive order by Subroutine CONTOUR

Figure 4-7. Subroutine CONTOUR Object Assignment

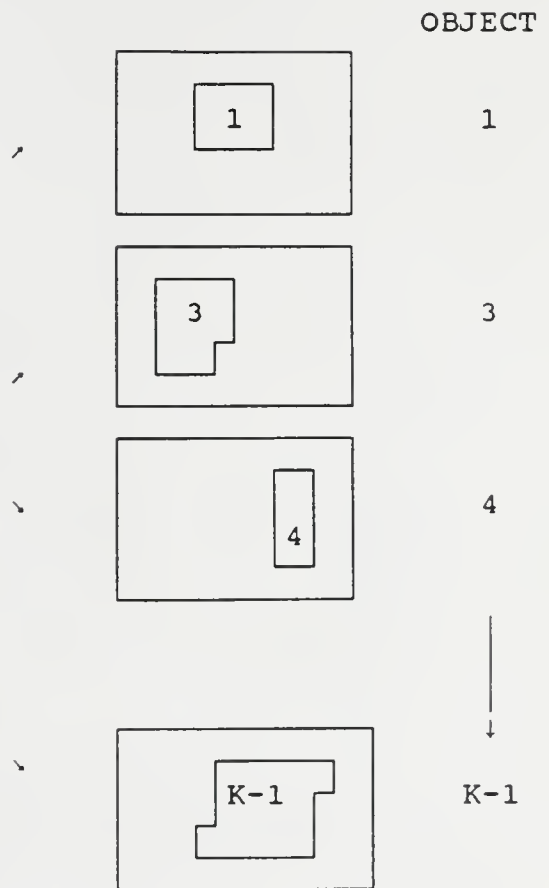
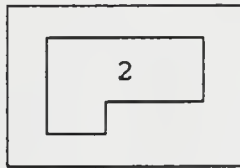
identification number is entered into the program. The selected object is then compared with the rest of the objects (Figure 4-8). If ninety percent of the object's voxels are the same for each slice as the selected object's voxels, the object is considered to be apart of the organ. This process is repeated for all organs. The organ's voxel indices, count, name, identification number, and volume are stored in the file, VOXEL.DAT.

Subroutine CORGAN

The subroutine CORGAN creates an organ given its voxel indices and identification parameters. Each pixel is assigned an integer value which will represent the organ volume desired. The number of image slices included in the organ is also assigned. The organ created is used as a photon reflector or sink; i.e., it either scatters or absorbs the incident photons, and represents the areas of the body not included in the SPECT image. If the whole body is to be included in the SPECTDOSE Program, it is necessary to create those areas of the body not seen in the SPECT images due to the limited field-of-view of the SPECT camera and the lack of availability of whole body SPECT images. These areas are created using this subroutine.

Select Object 2
for Comparison:

SELECTED
OBJECT



Selected objects are compared to the remaining objects for possible inclusion into one larger object (organ)

Figure 4-8. Illustration of Subroutine OBJSELECT Selected Object Comparison

Subroutine VOXFIL

Once the organ files have been created; i.e., each organ's voxel information has been stored in a VOXEL.DAT file, the subroutine VOXFIL assembles the organs (each VOXEL.DAT file) into one larger file called VOXPHAN.DAT. The number of organs; i.e., the number of VOXEL.DAT files, is entered into the program. This file contains the voxel indices, image counts, weighting factors, identification numbers, and the total number of voxels for all organs. The VOXPHAN.DAT file is read directly by the program ALGAMP.

Program ALGAMP

The program ALGAMP is a point energy gamma-ray monte carlo radiation transport code for calculating specific absorbed fractions of energy and absorbed dose data from internal and external sources (97). This program is written in Fortran and was developed at Oak Ridge National Laboratory in Oak Ridge, Tennessee (97). A flow chart of this program can be seen in Figure 4-9. This program is composed of 30 or more subroutines and initially utilized the organs of the parametrized phantom model from the Cristy Phantom Series (98). In this Series, the organs were represented by mathematical equations of various geometrical shapes, such as, spheres and cylinders. The equations were confined to a small number of ALGAMP subroutines (GEOM, SUM1, SUM2, and RESULT), which hasten the modification process.

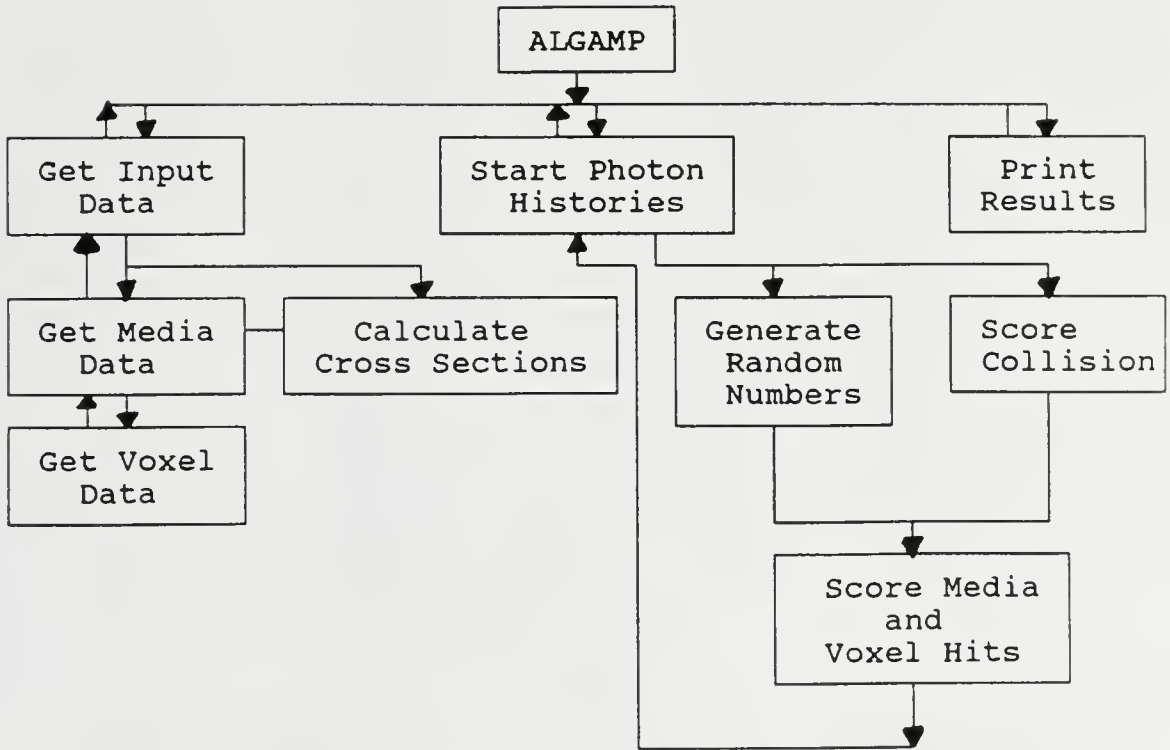


Figure 4-9. ALGAMP Flow Chart

The Cristy Phantom Series was not used in this research because it assumes a homogeneous source distribution, which is not valid in the case when radiolabeled monoclonal antibodies are used; the organs were not patient specific; and its inability to represent diseased organs, which are most often found in nuclear medicine patients.

Since each human is uniquely different, it was the desire of this research to make this new dosimetry method patient specific; i.e., the organs of the imaged subject are utilized in the calculation. This can be achieved by using the actual SPECT image to define the organ volumes and radioactive uptake. Each organ's voxel information was determined and compiled into the file VOXPHAN.DAT by the SPECT Model. The VOXPHAN.DAT file is read by ALGAMP. Each voxel inherently, at the level of the camera system's resolution, accounts for the heterogeneous source distribution exhibited in the organs at that level following the uptake of the radiolabeled monoclonal antibodies. If the activity is not distributed heterogeneously at the level of the camera system's resolution, which is approximately one half centimeter in this research, the voxels will reflect this and the activity will be assumed to be homogeneously distributed. For this homogeneous case, no additional modifications to ALGAMP would be needed. Several ALGAMP subroutines (INPUT, SOURCE, SEARCH, GEOM, SUM1, SUM2,

RESULT, and RANPOS) were modified to accommodate the inclusion of the voxel information.

For sources distributed in energy, the cumulative distribution function (cdf) for the source energy spectrum is used. A detailed cross-section table is generated for the source energies of interest. Each photon is weighted by a weighting factor which describes the probability of photons existing in a given voxel. The photon weighting factor is computed for each voxel by dividing the voxel image count by the average voxel count for a given organ. The source photon location is chosen by randomly sampling the voxel locations in the VOXPHAN.DAT file. Photon collisions are scored by determining the voxel location given the photon direction coordinates. Scoring is tallied for each voxel and organ.

Pixel and Slice Size Determination

In order to determine the organ volumes, it is necessary to determine the size of each image pixel and slice in physical dimensions. Since these values are dependent upon the camera system's electronics, they must be determined after each camera adjustment or change. A pixel and slice size determination study was conducted prior to the patient and phantom studies and in the case when the camera system's electronics were changed. Two line sources (small tubes containing ^{99m}Tc) of known length and distance apart are imaged in the planar (static) mode. The line

sources are imaged in both the parallel and perpendicular positions relative to the camera system's axis-of-rotation (AOR) to detect changes in the x and y planes, which would indicate the camera system was working improperly. The system software was used to return the number of pixels in a line drawn between the two line source centers in the planar imaged. The image pixel size in centimeters per pixel equals the distance between the two line sources in centimeters divided by the number of pixels in the line drawn between the line source centers. The slice size is determined by dividing the length of the line sources in centimeters by the number of transverse slices that is required to transverse the length of the line sources. The result is reported in centimeters per slice.

Phantom Studies

Since the Threshold Segmentation Method is used in this research, a threshold value which best relates the actual objects of interest to the resulting SPECT image objects must be determined. Three phantom studies were conducted to determine the best threshold value for a given volume and condition and to verify that the SPECT, Monte Carlo, and Dosimetry models were working properly. The first phantom study consisted of several cylinders of different volumes filled with homogeneously distributed activity (^{111}In) imaged in air. The second phantom study tested a torso phantom

containing three organ inserts under three experimental conditions. First, the organ inserts were filled with homogeneously distributed activity and placed in the cold (no activity present) water filling the torso phantom. Second, the organ inserts were filled with heterogeneously distributed activity and placed in the cold water filling the torso phantom. And last, the heterogeneously distributed organ inserts were placed in the hot (activity present) water filling the torso phantom. The last phantom study consisted of a single cylindrical volume filled with activity homogeneously and heterogeneously distributed and thermoluminescent dosimetry devices for measuring absorbed dose.

Phantom Study One

It is necessary to determine the best threshold value which will result in the SPECTDOSE program calculating the most accurate organ volume. A phantom study using objects of a known volume can be conducted to determine the threshold value which results in the SPECTDOSE program calculating a volume which is closest to the known volume. In this study, five cylinders of different sizes were SPECT imaged using the same setup parameters as in the Clinical Studies (see the previous section, SPECT Camera System) (Table 4-1). The resulting images were read by the program SPECTDOSE to calculate the phantom volume and activity concentration

Table 4-1. Phantom Study One Acquisition Parameters

FIVE CYLINDERS OF TISSUE EQUIVALENT MATERIAL

SOURCE: INDIUM-111

<u>PHANTOM</u>	<u>VOLUME (ml)</u>	<u>ACTIVITY (GBq)</u>
1	30.56	1.13
2	438.71	16.28
3	496.17	18.36
4	616.39	22.86
5	6032.50	229.33

ACQUISITION PARAMETERS:

360 degree rotation
128 views at 12 s view⁻¹
20% window over each peak
medium energy collimator
64 x 64 Matrix

PIXEL SIZE: 0.69 cm

SLICE SIZE: 0.71 cm

using different threshold values. The results were analyzed by linear regression to determine the correlation between the threshold value, phantom volume, and activity concentration. The threshold value that yielded the best correlation between the actual phantom volume and SPECTDOSE measured volume was used for that range of volumes and set of conditions.

Phantom Study Two

This study was conducted to simulate the conditions in which a patient has been injected with a radiolabeled substance. A tissue-equivalent torso phantom with a liver, spleen, and tumor insert was tested under several experimental conditions. The study set up parameters can be seen in Table 4-2. The tumor insert was placed 12 cm below the liver insert and the spleen insert was placed right of the tumor insert 2.5 cm below the liver insert (Figure 4-10). In the first experiment, the organ inserts were filled with homogeneously distributed ^{111}In activity and placed inside the torso phantom, which is filled with water with no radioactivity in it. The amount of activity added to the inserts and the acquisition parameters can be seen in tables 4-2 and 4-3. In the second experiment, the liver and spleen inserts were filled with small glass beads (5 mm diameter) and ^{111}In . The beads were used to distribute the radioactivity heterogeneously within those organs. This

Table 4-2. Phantom Study Two Acquisition Parameters

TORSO BODY PHANTOM WITH ORGAN INSERTS

SOURCE: INDIUM-111

<u>PHANTOM</u>	<u>VOLUME (ml)</u>
LIVER	1200.00
SPLEEN	166.31
TUMOR	0.26
BODY PHANTOM	13854.42

ACQUISITION PARAMETERS:

360 degree rotation
128 views at 12 s view⁻¹
20% window over each peak
medium energy collimator
64 x 64 matrix

PIXEL SIZE: 0.80 cm

SLICE SIZE: 0.82 cm

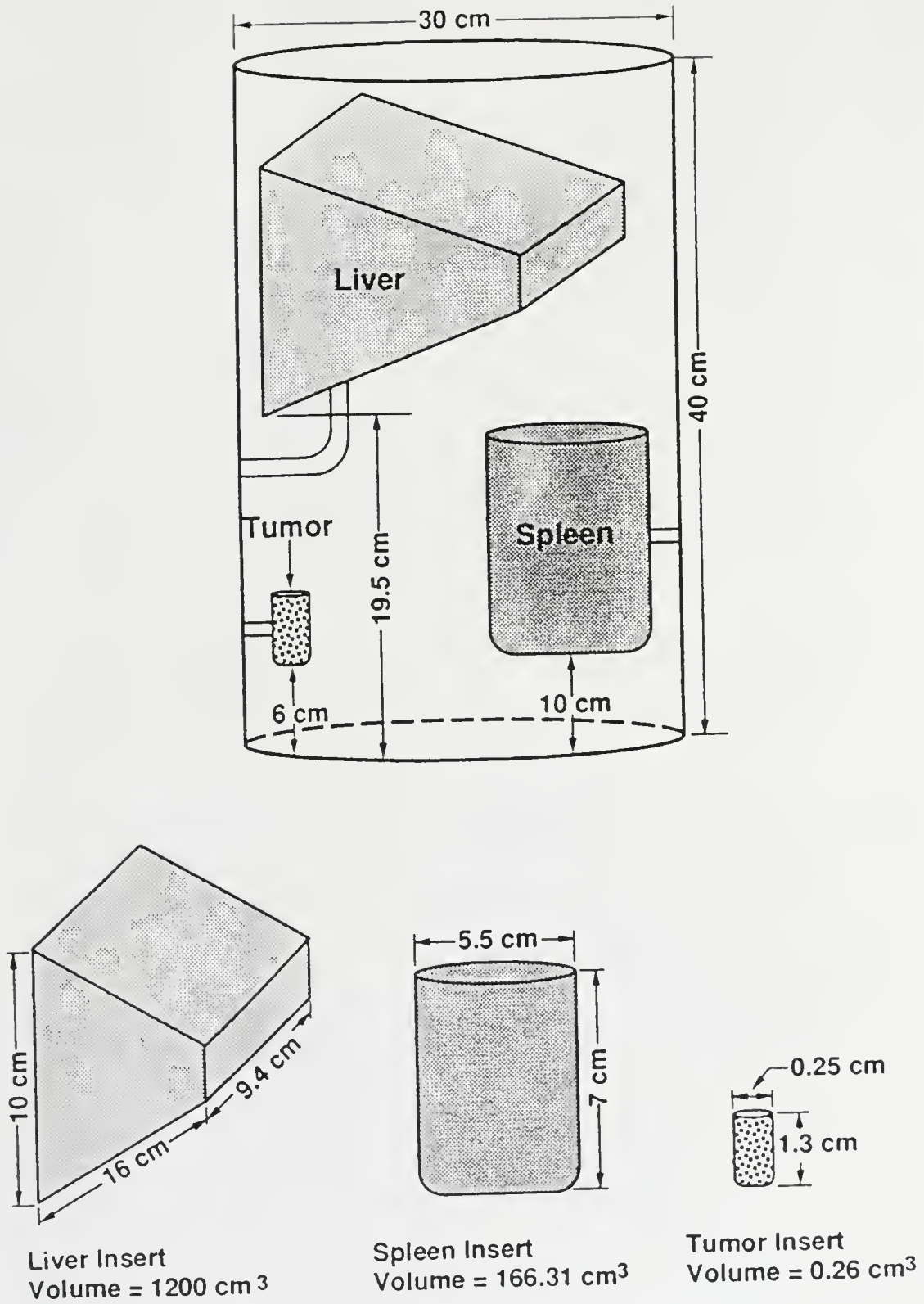


Figure 4-10. Phantom Study Two Torso Phantom and Organ Inserts

Table 4-3. Phantom Study Two Experiments

 I. HOMOGENEOUS DISTRIBUTION/COLD BACKGROUND

Activity is uniformly distributed within organ inserts with no activity in body phantom (background).

<u>PHANTOM</u>	<u>VOLUME (ml)</u>	<u>ACTIVITY (MBq)</u>
LIVER	1200.00	38.48
SPLEEN	166.31	5.74
TUMOR	0.26	2.37

II. HETEROGENEOUS DISTRIBUTION/COLD BACKGROUND

Glass beads were added to the liver and spleen inserts displacing 150 and 40 ml of liquid, respectively. No activity in body phantom.

<u>PHANTOM</u>	<u>VOLUME (ml)</u>	<u>ACTIVITY (MBq)</u>
LIVER	1200.00	32.45
SPLEEN	166.31	4.22
TUMOR	0.26	2.29

III. HETEROGENEOUS DISTRIBUTION/HOT BACKGROUND

Glass beads were added to the liver and spleen inserts displacing 150 and 40 ml of liquid, respectively. Activity was added to the body phantom.

<u>PHANTOM</u>	<u>VOLUME (ml)</u>	<u>ACTIVITY (MBq)</u>
LIVER	1200.00	31.45
SPLEEN	166.31	4.14
TUMOR	0.26	2.26
BACKGROUND	12307.89	5.81

experiment simulates the condition in which the patient's organ(s) has a cold (nonradioactive) tumor within it. The heterogeneously distributed radioactive organs and the homogeneously distributed tumor insert were placed in the cold (nonradioactive) water of the torso phantom and SPECT imaged. The third experiment consisted of the heterogeneously distributed radioactive liver and spleen inserts and the homogeneously distributed tumor insert from experiment two placed in the torso phantom which is filled with radioactive water and SPECT imaged. Indium-111 (5.8 MBq) was added to the water of the torso phantom (Table 4-3). Each experiment was SPECT imaged three times to detect camera fluctuations. If the results varied from image to image, this would indicate that the camera system was not working properly and that the variation in results was due to an improperly working camera system.

Phantom Study Three

This study was undertaken to verify the results of the Dosimetry Model by comparing its results to direct measuring devices placed in the phantom and to results calculated by other methods. Indium-111 was placed homogeneously and heterogeneously in the Jaszczak Phantom**** along with several thermoluminescent dosimetry devices. The Jaszczak Phantom is a cylinder made of tissue-equivalent material

**** Data Spectrum Corporation, High Point, NC 27514

with a volume of 6032.50 milliliters. In the first experiment, 73 megabecquerels of ^{111}In was added to the water of the Jaszczak Phantom and six TLD cards of two chips each were placed on the walls in various locations in the phantom (Figure 4-11). The phantom was SPECT imaged using the same camera setup parameters reported in the SPECT Camera System section of this chapter. The TLDs were exposed to ^{111}In for a half an hour in the phantom. In the second experiment, a cubed insert (7 cm x 6 cm x 7 cm) filled with air was added to the radioactive water of the phantom to distribute the activity heterogeneously. Six new TLD cards were added to the walls of the phantom and the cubed insert (Figure 4-12). The phantom was SPECT imaged using the same camera setup parameters noted above. The TLD cards, once exposed, were read by an automatic TLD reader****. The TLD reader was calibrated using a Cesium-137 needle source; whereby, two TLD cards were exposed to the ^{137}Cs source for each of the four exposure times (Appendix B). Once calibrated, the experimental TLD readings can be converted to exposure and absorbed dose. The TLD results calculated at time infinity were compared to the results of the Dosimetry Model, Geometric Factor Method (142), and the results calculated by use of data in MIRD Pamphlet No. 3 (143) at time infinity. It is assumed in each of these calculational methods

**** TLD System 4000, Harshaw/Filtrol Partnership, Solon, OH 44139

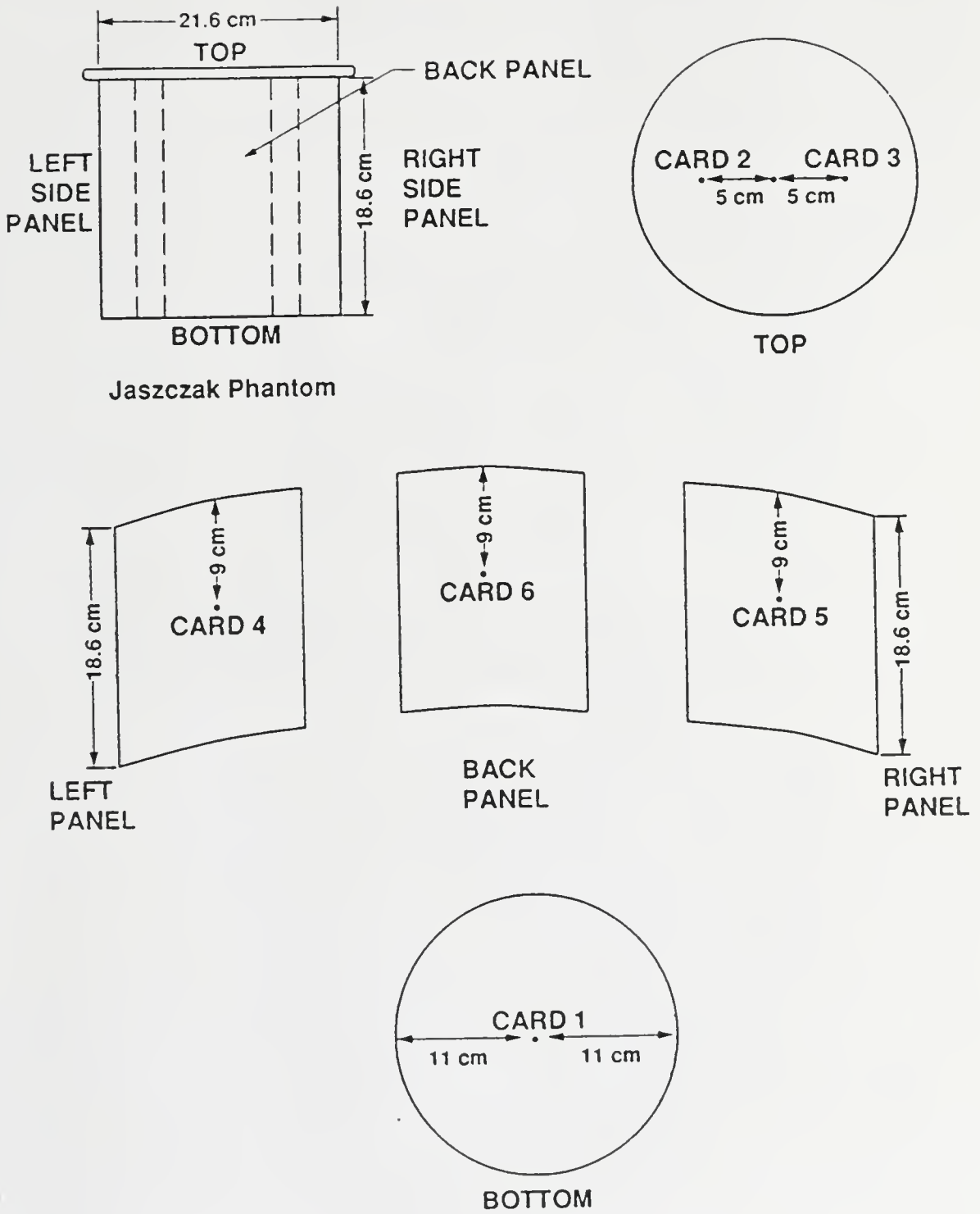


Figure 4-11. Phantom Study Three Experiment One TLD Location

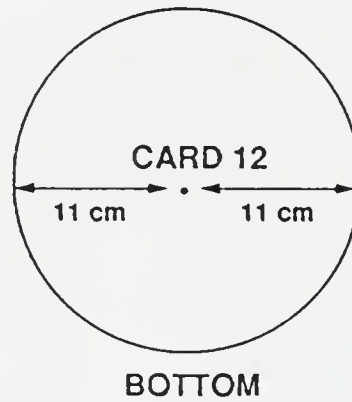
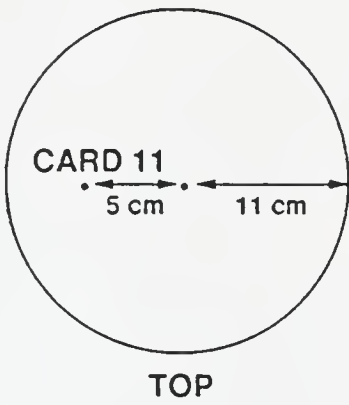
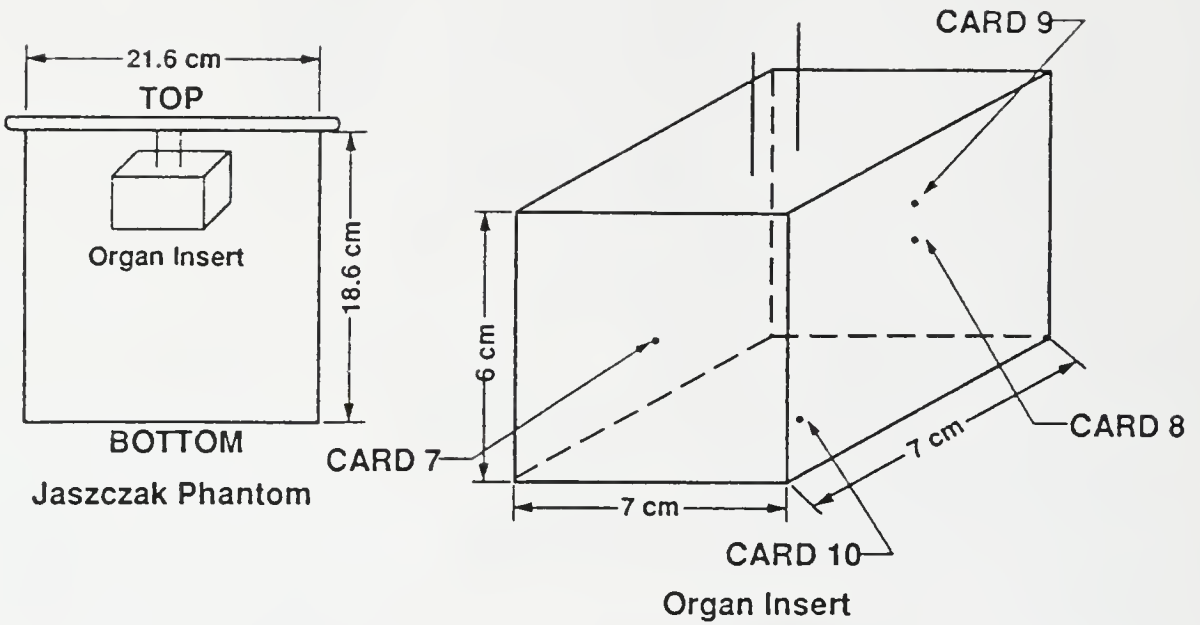


Figure 4-12. Phantom Study Three Experiment Two TLD Location

(Dosimetry Model, Geometric Factor Method, and MIRD Pamphlet No. 3) that the activity in the source organs are removed only by physical decay, the effective half-life is equal to the physical half-life, and all non-penetrating radiation is absorbed in the source organ.

Thermoluminescent Dosimeters (TLDs)

Ionizing radiation incident on a thermoluminescent crystal elevates an electron from the valence band to the conduction band to leave a hole in the valence band. The electron and hole pair migrate throughout the crystal until they are trapped at impurity sites. When the chip is heated, energy is imparted to the electron which causes it to move and to eventually recombine with its counterpart hole (or electron). The recombination energy is released in the form of visible light, which can be detected by a phototube. The thermoluminescent crystal used in this research is lithium fluoride, which is the most common thermoluminescent crystal used today (142). The lithium fluoride chip has a useful range that extends beyond 10^3 Sv and good linearity response, which extends below 0.1 mSv. The dynamic range of TLDs, in general, is large, with doses from a few mSv to 10 Sv. Two TLD-100 chips (0.318 cm x 0.318 cm x 0.009 cm) placed in the Type G-1 gamma card configuration***** were used in this research. Six Type G-1 cards were used in each

***** Harshaw/Filtrol Partnership, Solon, OH 44139

experiment and were secured in place in the phantom with a hot glue gun.

Clinical Studies

The results of Phase One, Two, and Three clinical studies being conducted at Bay Pines Veterans Administration Medical Center (VAMC) in Bay Pines, Florida, using indium-111 labeled B72.3-GYK-DTPA directed against colorectal cancer, will be utilized in this research. The goals of Phase One, Two, and Three studies are similar to those of this research, in that, they both seek to determine the radiation absorbed dose. Phase One, Two, and Three studies also seek to establish the radionuclide-antibody biodistribution, dosage range, clearance half-life, critical organs, and optimal imaging and sampling times in diseased patients (143). The research at Bay Pines VAMC is being sponsored by Cytogen Corporation of Princeton, New Jersey, and is ongoing. The experimental protocol for these studies is given below.

Patients

Sixteen male patients participating in a phase I-III study using indium-111 labeled B72.3-GYK-DTPA were screened prior to antibody infusion. The age of the patients ranged from 49-89 years with a mean age of 67 years. All subjects had

proven primary or were suspected of having recurrent colorectal cancer.

Monoclonal Antibody

The antibody, B72.3, is a murine monoclonal antibody of the IgG₁ subclass which detects a 200K-400K molecular weight tumor-associated glycoprotein called Tag-72. The Tag-72 antigen has been found to be expressed on certain human colon and human breast carcinoma cell lines. B72.3 is coupled to In-111 by oxidation of the oligosaccharide moieties on the constant region of the antibody molecule. This provides a site for specific attachment of radionuclides and other ligands, while retaining the homogeneous antigen affinity and binding characteristics of the antibody. B72.3 is conjugated with the linker complex, glycyl-tyrosyl-(N-ε-diethylenetriaminepentaacetic acid)-lysine (GYK-DTPA) to produce B72.3-GYK-DTPA-In-111 (Figure 4-13).

Monoclonal Antibody Procedure

Each patient was given a pre-infusion diagnostic blood screening workup prior to the antibody infusion. The analyses included routine blood chemistries, hematology, electrolyte, and urinalysis, serum TAG-72, HAMA and CEA levels. Each patient was then given B72.3-GYK-DTPA in randomly assigned doses of 0.5, 1 or 2 milligrams of

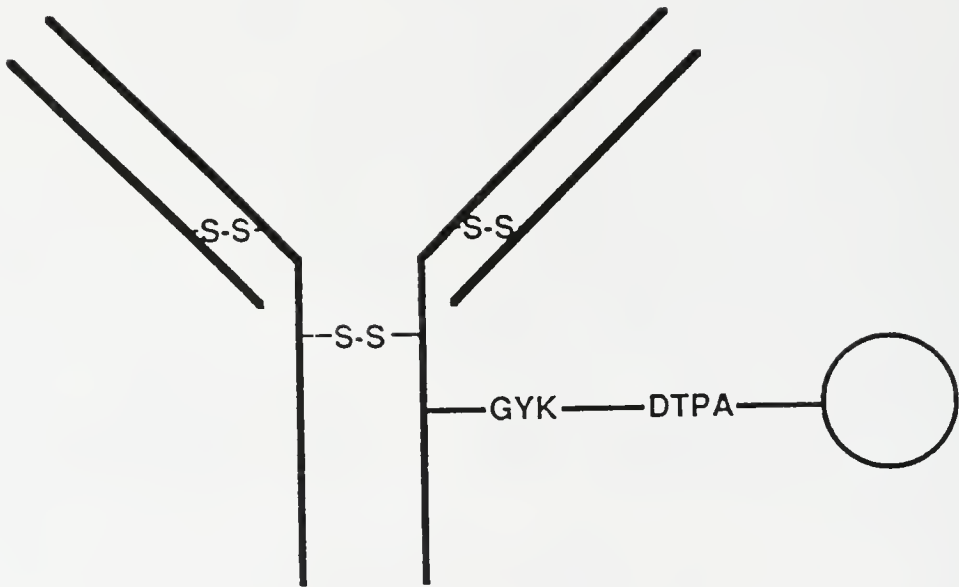


Figure 4-13. B72.3 Linker Complex

antibody radiolabeled with 129.5 - 185.0 MBq of indium-111 through an in-dwelling intravenous catheter (Heparin lock) by slow intravenous push over five minutes. The subject's vital signs and blood pressure was monitored prior to, and for two hours after antibody infusion.

Blood Analyses

Blood samples were taken via a Heparin lock in the arm opposite the infusion site at 1, 15, 30, 60, 90, 120, and 240 minutes after antibody injection. Additional blood samples were taken at 8, 24, and 30 hours and daily for seven days. All samples were then centrifuged and counted in an automated well counter. An aliquot of representative blood samples were analyzed by size exclusion HPLC chromatography.

HPLC Procedure

Representative blood and urine samples were analyzed by HPLC gel filtration chromatography with a ultraviolet radioisotope detector. Samples were diluted with a running buffer (PBS) prior to injection. Five-component standards and the data were analyzed using a computer, whereby separation was based on the component's molecular weight.

Image Analysis

Each patient was scanned by an external gamma camera***** at two hours, and on days one, three, seven post-infusion. Planar images (10 minutes/view) were acquired in both the anterior and posterior projection over the chest, abdomen, and pelvis. Standards of known activity were imaged along with the patient. Single Photon Emission Computed Tomography (SPECT) imaging was also performed on days three and seven.

***** Technicare Omega 500, Technicare Corporation,
Cleveland, OH 44139

CHAPTER 5
RESULTS AND DISCUSSION

The objective of this research was to develop a foundation for a dosimetry methodology which could be used to calculate absorbed doses in target and nontarget tissues using uniformly and nonuniformly distributed activity. In this proposed methodology, a computer program, SPECTDOSE, was developed to calculate the target and nontarget tissue volumes and activity concentrations. ALGAMP, a monte carlo program, was modified to determine the specific absorbed fractions. The results of the SPECT and Monte Carlo models were combined in the Dosimetry Model to determine the absorbed dose.

The accuracy of the SPECTDOSE program was accessed in several phantom studies; the results of which are presented in this chapter. Validation of the results from the modified ALGAMP program was made by comparing them to the results of the MIRDOSE2 program (141), the Geometric Factor Method (144,145), MIRD Pamphlet No. 3 results (146), and TLD measurements. The results of the pixel and slice size determination studies, the three phantom studies and the clinical study are presented in this chapter.

Pixel and Slice Size Determination Studies

Three pixel and slice size determination studies were performed: one prior to the Clinical Study, Phantom Study Two, and Phantom Study Three. The pixel size was determined to be 0.69 cm by 0.69 cm and the slice thickness was 0.71 cm for a 64 x 64 image in the Clinical Study. For Phantom Study Two, the pixel size was determined to be 0.80 cm and the slice size was 0.82 cm for a 64 x 64 image. The pixel size was 0.96 cm and the slice size was 0.98 cm in Phantom Study Three. The pixel and slice sizes had to be determined after the camera crystal was replaced prior to Phantom Study Two and after the camera system's electronics were adjusted prior to Phantom Study Three.

Phantom Study One

Phantom Study One was conducted to determine the best threshold value for a given range of volumes and to determine a relationship between the SPECT measured activity concentrations and the actual activity concentrations. Several threshold values were tested to determine the one which best related the actual phantom volumes to the SPECT measured volumes (Table 5-1). The standard error of the estimate was used to determine the best threshold value for the range of volumes in this study. For the five different cylindrical volumes in this study, a threshold value of 0.52 was determined to have the lowest standard error of the

Table 5-1. Phantom Study One Threshold Determination

Threshold	Standard Error of Estimate
0.20	87.4
0.25	76.0
0.30	76.1
0.35	74.6
0.45	69.1
0.50	63.5
0.52	63.4
0.53	117.0
0.55	92.8
0.60	88.8

estimate (63.4 ml) (Table 5-1). The SPECT measured volumes and concentrations using the threshold value of 0.52 is shown in Table 5-2. Using the threshold value 0.52, a positive correlation can be seen between the actual and SPECT measured volumes in Figure 5-1. A positive correlation is also seen between the actual activity concentration and the SPECT measured activity concentration using the threshold value of 0.52 (Figure 5-2). The correlation coefficient between the actual activity concentration and the SPECT measured activity concentration was 0.75. The increase in photon scatter within the phantoms and the enhancement of the object's boundaries by the Gaussian prefilter, which made segmentation of the SPECT image easier, may account for the excellent correlation between the actual and SPECT measured volumes. The poor correlation between the actual and SPECT measured activity concentrations is due to photon absorption attenuation and scatter which reduces the measured gamma ray intensity and thus, the SPECT measured activity concentration. The poor correlation between the actual and SPECT measured activity concentration is also attributed to the fact that the activity concentrations were essentially the same for each volume, which would produce a horizontal line with zero slope and no correlation. Thus, the low correlation coefficient is reflecting this point. Another study in which the phantom activity concentrations are varied more is

Table 5-2. Phantom Study One Results

Threshold Value = 0.52

Phantom	Volume		Standard Error (%)	Concentration	
	Actual (ml)	SPECT (ml)		Actual (GBq ml ⁻¹)	SPECT (ct vox ⁻¹)
1	30.6	61.1	99.9	0.037	116
2	438.7	558.1	27.2	0.037	144
3	496.2	767.1	54.6	0.037	134
4	616.4	792.0	28.5	0.037	154
5	6032.5	7077.4	17.3	0.038	168

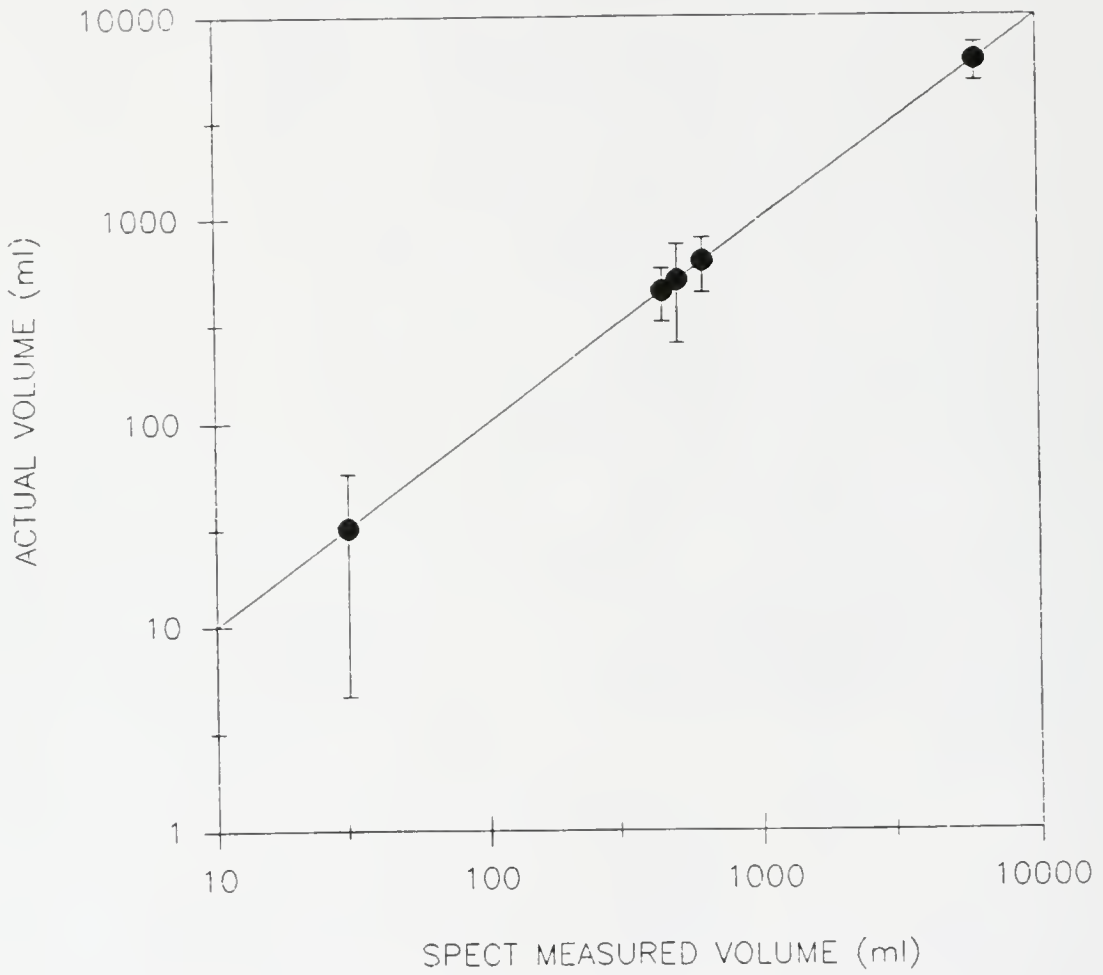


Figure 5-1. Phantom Study One: Actual versus SPECT Measure Volume

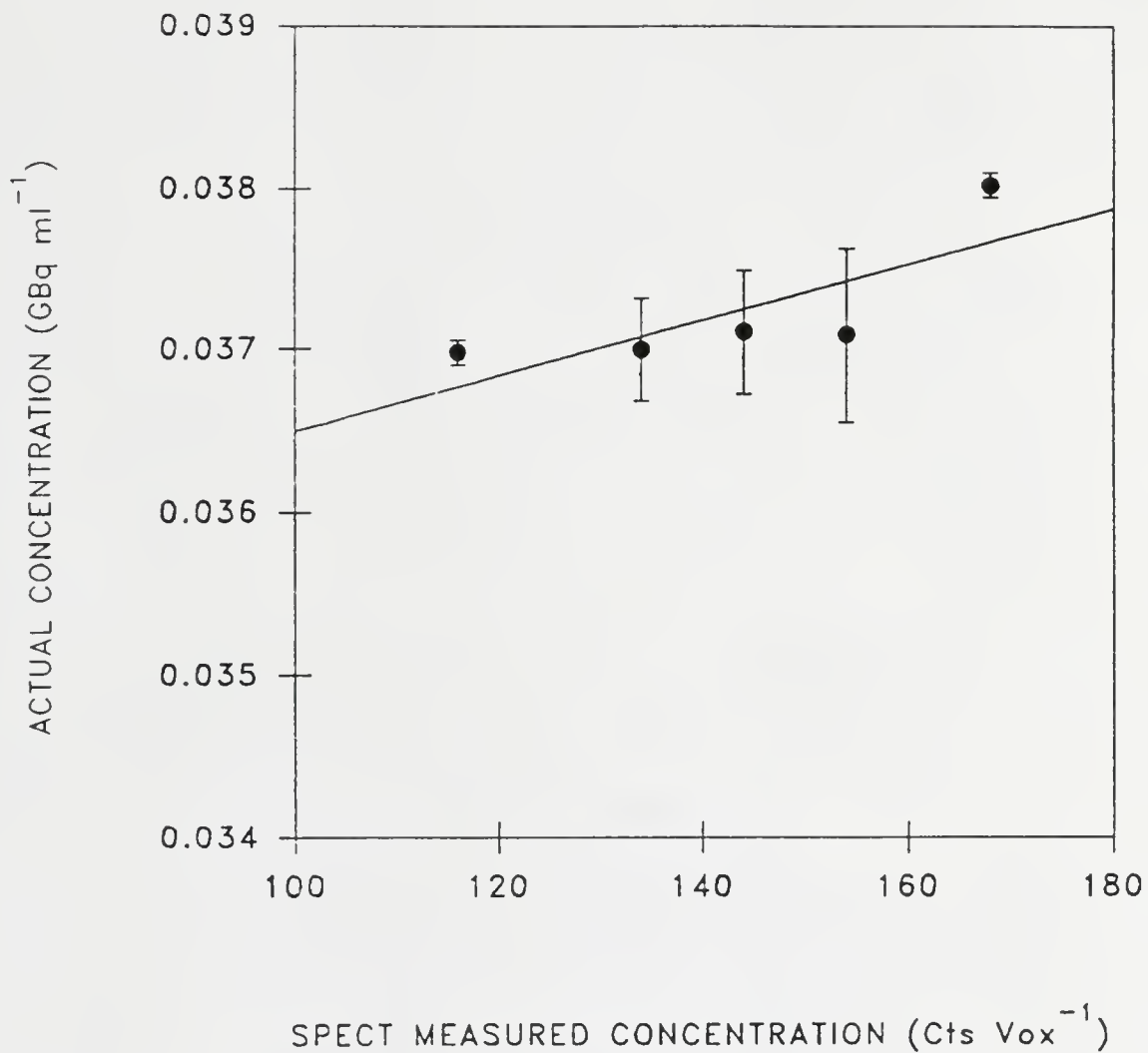


Figure 5-2. Phantom Study One: SPECT Measured versus Actual Activity Concentration

recommended to adequately assess the relationship between the actual and SPECT measured activity concentrations.

Phantom Study Two

Phantom Study Two consisted of three experiments in which three SPECT images were acquired for each experiment. The results presented for each experiment are the average of the results determined from each of the three images. In Experiment One, the organ inserts were filled with homogeneously distributed ^{111}In and placed in the nonradioactive water of the torso phantom. The phantom was SPECT imaged sequentially three times. In each of the resulting images, the tumor insert was not seen. It was determined that the Gaussian prefilter in the process of smoothing the SPECT image (removing noise) had removed the tumor from the image. The amount of activity in the tumor was very small (2.37 MBq) and the tumor image had similar image intensity values as the image background which aided the Gaussian prefilter in assuming it was image noise. The SPECT Model determined the volume and activity concentration for the remaining organs (liver and spleen). An average threshold value of 0.53 was used for this experiment (Table 5-3). The average difference between the actual and SPECT measured volume for the liver was 180.95 ml and 843.18 for the spleen. The SPECT Model overestimated the spleen volume and underestimated the liver volume in each image, however,

Table 5-3. Phantom Study Two Threshold Determination

Experiment	Threshold Value	Average Threshold Value	Correlation of Coefficient
COLD HOMO-1*	0.52	-----	n/a**
COLD HOMO-2	0.52	0.53	n/a
COLD HOMO-3	0.55	-----	n/a
COLD HETER-1***	0.55	-----	n/a
COLD HETER-2	0.56	0.56	n/a
COLD HETER-3	0.58	-----	n/a
HOT HETER-1****	0.67	-----	0.97
HOT HETER-2	0.50	0.56	0.89
HOT HETER-3	0.50	-----	1.00
COLD HOMO-NG†	0.62	-----	1.00
COLD HETER-NG††	0.60	-----	0.83

* Cold Homogeneous-Image#

** n/a - Not Applicable (only two data points)

*** Cold Heterogeneous-Image#

**** Hot Heterogeneous-Image#

† Cold Homogeneous-Image 2 no Gaussian prefilter

†† Cold Heterogeneous-Image 2 no Gaussian prefilter

the liver estimations were closer to the actual values (Table 5-4). It can be inferred from this limited observation (two data points) that there is a positive correlation between the actual and SPECT measured volumes. This is perhaps due to the fact that image segmentation is easier for larger volumes (see Image Segmentation section in Chapter 4). A negative correlation can also be inferred between the actual and SPECT measured activity concentrations. The conclusion that there is a positive correlation between the actual and SPECT measured volumes and a negative correlation between the actual and SPECT measured activity concentrations may be invalid if more data is acquired; however, the standard deviations support these observed trends. Since there are only two data points (liver and spleen) for this experiment, the number of inferences that can be made about the experiment is limited.

In Experiment Two, the results were similar to those of Experiment One, but requiring a higher average threshold value of 0.56 (Table 5-3). The increase in the average threshold value from Experiment One to Experiment Two is due to the decrease in activity in the liver and spleen inserts and the increase of scatter photons within the phantoms, which manifests itself as noise in the image. When a large amount of noise is present in an image, a higher threshold value is required to segment objects from the noisy

Table 5-4. Phantom Study Two Experiment One Results

Image	Liver Volume		Spleen Volume	
	Actual (ml)	SPECT (ml)	Actual (ml)	SPECT (ml)
1	1200.0	1142.8	166.3	1417.7
2	1200.0	955.4	166.3	832.5
3	1200.0	959.0	166.3	778.2
Average	1200.0	1019.1	166.3	1009.5
Standard Deviation		107.2		354.6

Image	Liver Activity Concentration		Spleen Activity Concentration	
	Actual (MBq ml ⁻¹)	SPECT (cts vox ⁻¹)	Actual (MBq ml ⁻¹)	SPECT (cts vox ⁻¹)
1	0.032	137	0.035	127
2	0.032	160	0.035	148
3	0.032	152	0.035	143
Average	0.032	150	0.035	139
Standard Deviation		11.7		11.0

background (Chapter 4, Image Segmentation section). The average SPECT measured volume was 1110.7 ml for the liver insert and 1091.6 ml for the spleen insert (Table 5-5). The tumor insert was not seen in the images of this experiment because it was filtered out of the images by the Gaussian prefilter. The SPECT Model underestimated the liver volume by an average of 89.3 ml, which represents a standard error of 7.4%, and overestimated the spleen volume by an average of 925.3 ml, which is a factor of six or more higher (Table 5-5). Thus, the actual volume correlates positively with the SPECT measured volume in this experiment. The actual activity concentration correlated positively with the SPECT measured activity concentration; however, this observation is limited by the two data points. Again, due to the limited amount of data in this experiment, any other conclusions drawn from this data would be highly speculative.

Experiment Three's results were consistent with the previous experiments. This experiment is a representation of the conditions most often found in nuclear medicine patients. The activity in the background of the torso phantom represents the blood pool of the patient and the organ inserts with heterogeneously distributed activity (glass beads placed in organ inserts to distribute activity heterogeneously) represents the patient's organ following injection of radiolabeled monoclonal antibodies. The tumor insert was seen in the images of this experiment after the

Table 5-5. Phantom Study Two Experiment Two Results

Image	Liver Volume		Spleen Volume	
	Actual (ml)	SPECT (ml)	Actual (ml)	SPECT (ml)
1	1200.0	1174.0	166.3	1330.7
2	1200.0	1157.6	166.3	1017.3
3	1200.0	1000.5	166.3	926.7
Average	1200.0	1110.7	166.3	1091.6
Standard Deviation		95.8		212.0

Image	Liver Activity Concentration		Spleen Activity Concentration	
	Actual (MBq ml ⁻¹)	SPECT (cts vox ⁻¹)	Actual (MBq ml ⁻¹)	SPECT (cts vox ⁻¹)
1	0.027	159	0.025	143
2	0.027	151	0.025	138
3	0.027	162	0.025	143
Average	0.027	157	0.025	141
Standard Deviation		5.7		2.9

use of the Gaussian prefilter. The average threshold value for this experiment was 0.56 (Table 5-3). The threshold value of Image One was 0.67, which was higher than Images Two and Three. The threshold value of Image One was higher than expected and was due in part to the movement (settling) of the glass beads within the organ inserts while the image was being acquired.

The average threshold value in this experiment would increase in comparison to the two other experiments because there was an increase in the number of scattered photons within the torso phantom. The Gaussian prefilter would smooth out the objects' edges which would make it difficult to distinguish one object's edge from another in the presence of the image noise, which would make it difficult to see the tumor insert in the SPECT image. On the contrary, the tumor insert was seen in this experiment. No explanation is offered for this contradiction.

The SPECT Model overestimated the volumes for all three inserts in this experiment with the smallest overestimation occurring for the liver volume (Table 5-6). The correlation between the Actual and SPECT measured volume for this experiment was positive. The large standard deviations for the mean of the volumes was an indication of the usefulness of this result and also demonstrated a positive trend in the

Table 5-6. Phantom Study Two Experiment Three Results

Image	Liver Volume		Spleen Volume		Tumor Volume	
	Actual (ml)	SPECT (ml)	Actual (ml)	SPECT (ml)	Actual (ml)	SPECT (ml)
1	1200.0	685.1	166.3	260.1	0.26	22.0
2	1200.0	1859.1	166.3	1052.2	0.26	12.8
3	1200.0	1510.9	166.3	90.1	0.26	4.6
AVG*	1200.0	1351.7	166.3	467.5	0.26	13.1
SD**		609.0		513.5		8.7

Image	Liver Activity Concentration		Spleen Activity Concentration		Tumor Activity Concentration	
	Actual (MBq ml ⁻¹)	SPECT (cts vox ⁻¹)	Actual (MBq ml ⁻¹)	SPECT (cts vox ⁻¹)	Actual (MBq ml ⁻¹)	SPECT (cts vox ⁻¹)
1	0.026	138	0.025	115	8.7	4
2	0.026	98	0.025	121	8.7	3
3	0.026	104	0.025	53	8.7	3
AVG*	0.026	113	0.025	96	8.7	3
SD**		21.6		37.7		0.6

* AVG - Average

** SD - Standard Deviation

data (Table 5-6). The correlation between the actual and SPECT measured activity concentration was negative. The standard deviations for this data indicate a negative trend (Table 5-6). As the actual activity concentration increases, the SPECT measured activity concentration decreases.

The results of this experiment demonstrate that the SPECT Model overestimates the volume and underestimates the activity concentration. This result can be remedied by the use of a higher threshold value, which would allow the SPECT Model to better predict the volumes and activity concentrations.

To determine what effect the Gaussian prefilter had on the images, the results of Experiment One and Two were compared to the case in which no Gaussian prefilter was used. The raw image data for both experiments was reconstructed without the use of the Gaussian prefilter. Since the Gaussian prefilter was not used, the tumor insert was seen in the images for this test. In Experiment One, without the use of the Gaussian prefilter (Cold Homogeneous-No Gaussian prefilter), a threshold value of 0.62 was determined to produce a positive correlation between the actual and SPECT measured volumes. Using this threshold value, there was a negative correlation between the actual activity concentration and the SPECT measured activity concentration. The best threshold value for Experiment Two without the use of the Gaussian prefilter (Cold

Heterogeneous-No Gaussian prefilter) was determined to be 0.60. The correlation was positive between the actual and SPECT measured volume and negative between the actual and SPECT measured activity concentration in this case.

Comparisons can now be made between the images with and without the Gaussian prefilter to assess its effect. Table 5-7 shows the results of comparing the threshold values, correlation slope signs and magnitudes, and correlation coefficients for Image Two of Experiment One and Two with and without the Gaussian prefilter. From this test it was concluded that the absence of the Gaussian prefilter necessitated the use of a higher threshold value (Table 5-7). This result was expected since there is more noise present in the image when the Gaussian prefilter is not used, which makes image segmentation difficult and requires a higher threshold value to segment the objects from the image background noise. One may conclude from this Study that the Gaussian prefilter smooths the image, which reduces the amount of noise present in the image. This effect acts to reduce the threshold value required to segment the image.

The results of Phantom Study Two showed that the SPECT Model overestimates the activity concentration in the organs. This overestimation is greatest for the smaller volumes. Upon further investigation of this result, it was found that the calculation of the SPECT measured activity concentration in the program SPECTDOSE had been performed

Table 5-7. Gaussian Prefilter Comparison: Actual Versus SPECT Measured Volume

Parameter	COLD HOMO-2* w/Gauss.***	COLD HOMO w/o Gauss.†	COLD HETER-2** w/Gauss.	COLD HETER w/o Gauss.
Threshold Value	0.52	0.62	0.56	0.60
Correlation Slope Sign	n/a††	(+)	n/a	(-)
Correlation Slope Magnitude	n/a	1.7	n/a	0.63
Correlation Coefficient	n/a	1.00	n/a	1.00

Gaussian Prefilter Comparison: Actual Versus SPECT Measured Activity Concentration

PARAMETER	COLD HOMO-2* w/Gauss.***	COLD HOMO w/o Gauss.†	COLD HETER-2** w/Gauss.	COLD HETER w/o Gauss.
Threshold Value	0.52	0.62	0.56	0.60
Correlation Slope Sign	n/a	(-)	n/a	(+)
Correlation Slope Magnitude	n/a	0.69	n/a	0.76
Correlation Coefficients	n/a	1.00	n/a	0.83

- * Cold Homogeneous-Image 2
 ** Cold Heterogeneous-Image 2
 *** With Gaussian prefilter
 † Without Gaussian prefilter
 †† n/a - Not Applicable (only two data points)

incorrectly. In the Subroutine THOLD of SPECTDOSE, the user-entered threshold value is multiplied by the maximum image count and any pixels having values greater than this result, are considered to be apart of the object. This method is correct for volume calculations, but not for activity concentration calculations. For activity concentration calculations, the resulting value of the threshold value times the maximum image count is subtracted from each pixel's value and any pixel with a value greater than this result is considered to be apart of the object. A modification was made to the program SPECTDOSE, but unfortunately, the results were the same, i.e. the SPECT Model overestimates the activity concentration in the organs. Since the activity concentrations utilized in this study were determined using the relation between the actual and SPECT measured activity concentrations determined in Phantom Study One, the conclusions stated above may or may not be valid. Since the relationship developed between the actual and SPECT measured activity concentrations in Phantom Study One was only accurate for the limited activity concentrations, it may not be appropriate for the wider range of activity concentrations utilized in this study. However, this can be easily remedied by conducting another phantom study as in Phantom Study One in which the range of activity concentrations of interest are used.

The accuracy of the Dosimetry Model developed in this research was tested by comparing the results of this study using the Dosimetry Model to those using the MIRDOSE2 program (141). In MIRDOSE2, the liver and spleen are used both as organs of source activity and targets. The liver and spleen residence times, which are required for the MIRDOSE2 calculation, were calculated by using the organ anterior and posterior counts determined from Planar imaging taken at specific times and then fitting this data after decay correction to an exponential function by using a subroutine supplied with the MIRDOSE2 program. The Dosimetry Model requires the use of the pixel and slice sizes determined in the Pixel and Slice Size Determination Study. The results of both programs are presented in Table 5-8 for this study.

In Experiment One, the percent difference between the Dosimetry Model and MIRDOSE2 absorbed dose result was ten percent for the liver and four percent for the spleen. The average absorbed dose in the liver was 141 mGy and 130 mGy in the spleen as calculated by the Dosimetry Model (Table 5-8).

In Experiment Two, the average dose in the liver was 111 mGy and 109 mGy in the spleen as calculated by the Dosimetry Model (Table 5-8). In this experiment, the percent difference between the Dosimetry Model and MIRDOSE2 absorbed dose was three percent for the liver and nine percent for the spleen (Table 5-8).

Table 5-8. Phantom Study Two Absorbed Dose Results

EXPERIMENT 1:						
Image	DM* Liver (mGy)	MIRDOSE2 Liver (mGy)	DM Spleen (mGy)	MIRDOSE2 Spleen (mGy)		
1	128.7	128.4	106.8	136.0		
2	143.7	128.4	146.2	136.0		
3	149.6	128.4	138.3	136.0		
Average	140.7	128.4	130.4	136.0		
SD**	10.8		20.8			
Standard Error Liver: 9.54% Spleen: - 4.10%						
EXPERIMENT 2:						
Image	DM Liver (mGy)	MIRDOSE2 Liver (mGy)	DM Spleen (mGy)	MIRDOSE2 Spleen (mGy)		
1	105.4	107.7	95.4	100.2		
2	112.3	107.7	111.4	100.2		
3	116.3	107.7	121.7	100.2		
Average	111.4	107.7	109.5	100.2		
SD	5.5		13.2			
Standard Error Liver: 3.39% Spleen: 9.25%						
EXPERIMENT 3:						
Image	DM Liver (mGy)	MIRDOSE2 Liver (mGy)	DM Spleen (mGy)	MIRDOSE2 Spleen (mGy)	DM Tumor (mGy)	MIRDOSE2 Tumor (mGy)
1	187.2	105.0	336.7	98.5	1028.3	n/a***
2	111.6	105.0	146.4	98.5	1505.7	n/a
3	129.3	105.0	498.9	98.5	1090.6	n/a
Average	142.7	105.0	327.3	98.5	1208.2	n/a
SD	39.5		176.4		259.5	
Standard Error Liver: 35.89% Spleen: 232.30%						

* SD - Standard Deviation

** DM - Dosimetry Model

*** n/a - Not applicable (MIRDOSE2 does not calculate tumor absorbed doses)

In Experiment Three, the Dosimetry Model had a percent difference of 36% for the liver absorbed dose to that of MIRDOSE2. The Dosimetry Model and MIRDOSE2 differed by a factor of three in the calculation of absorbed dose for the spleen (Table 5-8). The Dosimetry Model also calculated the absorbed dose for the tumor insert in this experiment, which was 1208 mGy (Table 5-8). The MIRDOSE2 program does not calculate tumor absorbed doses.

The Dosimetry Model absorbed dose estimate for the liver differed by as much as 36% to that of the MIRDOSE2 absorbed dose estimate and by as much as a factor of two for the spleen. This difference may be explained by the use of different organ volumes in the calculation of the absorbed doses by each method. The MIRDOSE2 program uses the organs of Reference Man in which the liver is 1800 ml and the spleen is 150 ml (103). The Dosimetry Model used a smaller liver volume of 1200 ml and a larger spleen volume of 166.31 ml. A volume difference of 50% is found between each method's liver volume and a volume difference of 11% is found between the spleen volumes. The absorbed dose for the Dosimetry Model was higher than the MIRDOSE2 absorbed dose because of its higher nonpenetrating dose contribution due to the smaller liver volume used (specific absorbed fraction equals $1/m$). And accordingly, the MIRDOSE2 spleen absorbed dose was higher in Experiment One and Two. The volume differences do not completely account for the difference in

absorbed doses for the liver and spleen by the two methods, therefore, other causes will be examined in the next phantom study.

Phantom Study Three

Phantom Study Three was conducted to test the accuracy of the Dosimetry Model. The Jaszczak Phantom was filled with homogeneously and heterogeneously distributed activity and thermoluminescent devices (TLDs). A threshold value of 0.47 was found to give the best estimate of the Jaszczak Phantom volume (6103.8 ml) in Experiment One, which is the homogeneously distributed activity case. Experiment Two's, (heterogeneously distributed activity), threshold value was 0.45 with a calculated volume of 6024.2 ml. The volume percent difference was less than 1.2% in Experiment One and 0.1% in Experiment Two. In Experiment One, the TLDs were placed in the phantom (cards one through six) and the phantom was filled with homogeneously distributed ^{111}In in water (Figure 5-3). The measured TLD absorbed doses and rates for this experiment are shown in Table 5-9. The average absorbed dose rate for Experiment One was $2.84 \pm 0.41 \text{ mGy h}^{-1}$ (278 mGy). In Experiment Two, the TLDs were placed in the phantom and on the organ insert (cards six through twelve), and the phantom was filled with heterogeneously distributed ^{111}In in water (Figure 5-3). The average absorbed dose rate for Experiment Two was $1.84 \pm$

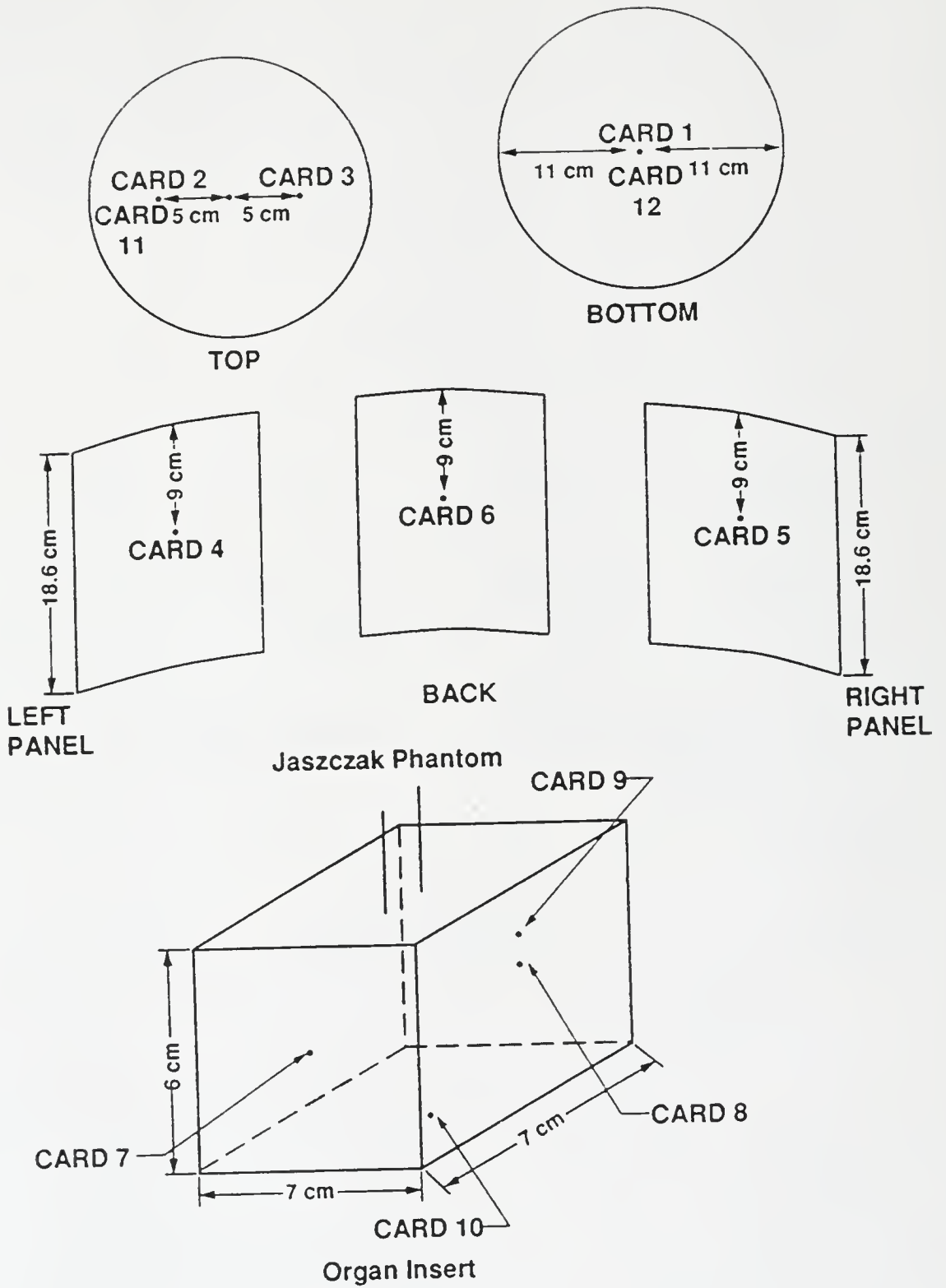


Figure 5-3. Phantom Study Three TLD Experimental Locations

Table 5-9. Phantom Study Three TLD Measurements

Location	Experiment 1		Location	Experiment 2	
	Absorbed Dose Rate (mGy h ⁻¹)	Total Dose (mGy)		Absorbed Dose Rate (mGy h ⁻¹)	Total Dose (mGy)
1	3.30	322.9	7	2.78	272.8
2	2.14	209.4	8	1.45	142.1
3	2.71	265.6	9	2.07	203.0
4	3.16	309.7	10	2.00	196.3
5	2.87	281.0	11	1.51	148.4
6	2.88	281.7	12	1.23	120.2
AVG*	2.84	278.4		1.84	180.5
SD**	0.41	39.8		0.56	55.5

* AVG - Average

** SD - Standard Deviation

0.56 mGy h⁻¹ (181 mGy) (Table 5-9). This result is consistent, in that, the average absorbed dose was lower because of the smaller amount of activity in the phantom, which was displaced by the organ insert. The average TLD absorbed dose rates were integrated out to infinity for each experiment to derive the total absorbed dose. It is assumed in this integration that the activity is removed only by decay and the effective half-life is equal to the physical half-life.

The TLD results of this study were compared to the results calculated for this study by the use of the Geometric Factor Method (144,145) and the results found using data in MIRD Pamphlet No. 3 (146) for a similar phantom.

In the Geometric Factor Method, the integral equation that represents the volume of interest, a cylinder in this study, located at a distance r from the point where the absorbed dose is desired, is approximated by an average geometric factor. The average geometric factor has been calculated and tabulated for cylinders of different heights and diameters (144). The average absorbed dose for gamma photons in the cylinder is calculated by multiplying the activity concentration of the cylinder by the specific gamma-ray emission and by the average geometric factor (145) and is tabulated in the reference for various radioactive sources. The specific gamma-ray emission is the gamma

radiation exposure rate from a point source of unit activity at a unit distance (145). It is assumed in this method that the source activity is uniformly distributed (144,145).

Tabulated in MIRD Pamphlet No. 3 are absorbed fractions for various sized spheres which contain uniformly distributed gamma emitting activity. Absorbed fractions for a sphere of six kilograms approximated the cylinder used in this study. The chosen absorbed fractions are put into the MIRD Formula (74) to determine the average absorbed doses.

The results of the Geometric Factor and MIRD Pamphlet No. 3 methods are seen in Table 5-10 and are reported as average absorbed doses at infinity. The total absorbed doses include the assumptions that the activity is removed only by physical decay, the effective half-life is equal to the physical half-life, and all non-penetrating radiations are absorbed in the target organ.

Phantom Study Three was also analyzed by the Dosimetry Model. The resulting absorbed dose for Experiment One was 58 mGy and for Experiment Two, 51 mGy after 10000 histories (Table 5-11). The coefficient of variation for the specific absorbed fractions was one percent for both Experiment One and Two. In the Dosimetry Model, the absorbed doses were calculated using the MIRD Formula (74) after the specific absorbed fractions were determined using the Monte Carlo Model (Appendix A).

Table 5-10. Phantom Study Three Geometric Factor Method and MIRD Pamphlet No. 3 Results

Experiment	Geometric Factor Method Absorbed Dose (mGy)	MIRD Pamphlet No. 3 Absorbed Dose (mGy)
1	63.5	64.4
2	61.0	57.7

Table 5-11. Phantom Study Three Dosimetry Model Results

	Experiment 1	Experiment 2
Activity A_0 (MBq)	43.40	41.44
Photon Histories	10000	10000
Specific Absorbed Fraction (kg^{-1})	0.03	0.03
Coefficient of Variation (%)	1.1	1.2
Absorbed Dose (mGy)	58.3	51.1

A comparison can now be made between the four methods for determining absorbed dose; whereby, each method's total absorbed dose values are shown in Table 5-12. The absorbed doses calculated using the calculational methods compared well with each other; however, the TLD measurements were a factor of two or more greater than these other methods. If the average absorbed doses calculated by the use of the data in MIRD Pamphlet No. 3 are considered the standard by which all calculations will be compared, the standard error between the results of using MIRD Pamphlet No. 3 and the other methods and measurements are presented in Table 5-13. The Geometric Factor Method underestimated the absorbed dose in Experiment One by one percent and overestimated the absorbed dose in Experiment Two by six percent. The Dosimetry Model underestimated the absorbed dose by 10% and 11% in Experiment One and Two respectively. The TLD measurements overestimated the absorbed dose by a factor of four and three for experiments One and Two respectively. A complete error analysis was initiated to determine the cause and contribution of errors in this study, especially in the TLD measurements. It was discovered that the error of greatest significance was found in the TLD measurements and was associated with the TLD reader and its initial calibration. A calibration study; whereby, several TLDs were exposed to known amounts of activity were read by the same TLD reader as used in Phantom Study Three, was conducted to

Table 5-12. Phantom Study Three Results

Experiment	TLD Average Abs. Dose (mGy)	Geometric Factor Method Abs. Dose (mGy)	MIRD Pamphlet No. 3 Abs. Dose (mGy)	Dosimetry Model Abs. Dose (mGy)
1	278.4	63.5	64.4	58.3
2	180.5	61.0	57.7	51.1

Table 5-13. Phantom Study Three Error Analysis

Standard Error between MIRD Pamphlet No. 3 Results :

Experiment	Standard Error* TLD Average (%)	Standard Error Geometric Factor Method (%)	Standard Error Dosimetry Model (%)
1	332.3	- 1.4	- 9.5
2	212.8	5.7	- 11.5

* Standard Error = $100 \times \frac{(X - \text{MIRD Pamphlet No. 3 value})}{\text{MIRD Pamphlet No. 3 value}}$

X = TLD, Geometric Factor, or Dosimetry Model value

estimate the amount error associated with the TLD reader. The results of this study, which was conducted as a blind study; i.e., the TLD exposure was unknown to the TLD reader operator prior to reading the exposed chips, are presented in Table 5-14. At the lower exposures, the TLD reader overestimated the exposures by as much as 52% and at the higher exposures, it overestimated the exposures by 39%. This accounts for most of the error found between the TLD measurements and the MIRD Pamphlet No. 3 calculation; however, the TLD measurements were still one order of magnitude above the calculated results using MIRD Pamphlet No. 3. The remaining error was attributed to the dose calibrator (~3%), the monte carlo calculation in MIRD Pamphlet No. 3 (~2%), and to the TLD exposure time (~20%); however, since the exact cause of the TLD measurement error could not be identified, the results of this experiment will not be utilized in this research.

A second phantom study using the same setup as in Phantom Study Three was conducted, but with TLD chips which were read by a more reliable TLD chip reader and in which all parameters, such as, the exposure time and packet drying were monitored more closely.

Two TLD chips (lithium fluoride) were wrapped in black paper to limit exposure to light and sealed in polyethylene plastic (Figure 5-4). Seventeen chip packets were adhered to various locations throughout the inside of the Jaszczak

Table 5-14. TLD Calibration Study

Actual Exposure (mR)	Measured Exposure (mR)	Standard Error (%)
55.0	83.6	52.0
55.0	76.4	38.9
55.0	74.2	34.9
Bkg*	Bkg	0.0
99.0	121.6	22.8
99.0	122.0	23.2
99.0	145.9	47.3
Bkg	Bkg	0.0
148.0	191.3	29.2
148.0	193.7	30.9
148.0	215.0	45.3
Bkg	Bkg	0.0
198.0	247.5	38.7
198.0	275.0	38.9
198.0	252.1	27.3

* Bkg - Background Exposure

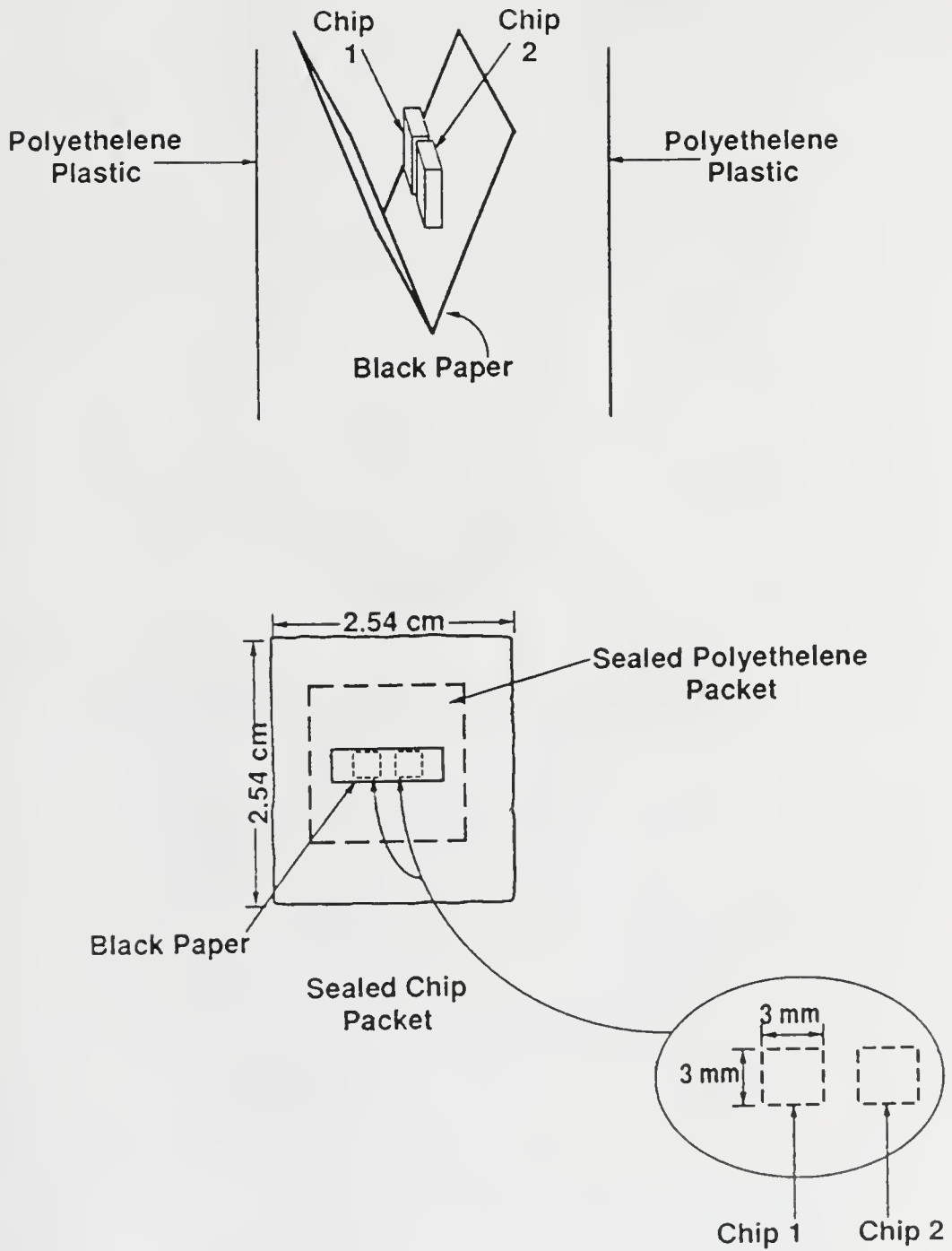
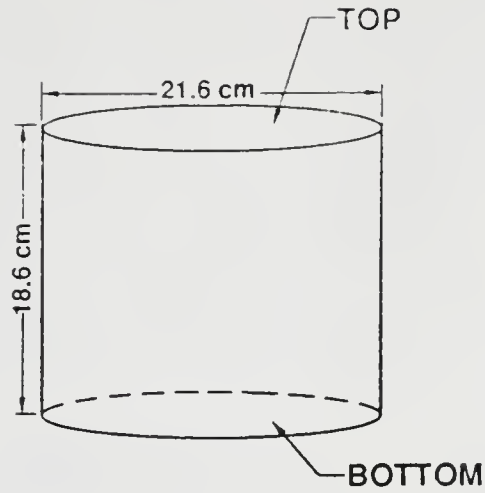


Figure 5-4. Phantom Study Four TLD Chip Packaging

Phantom by a hot glue gun (Figure 5-5). One millicurie of ^{111}In was homogeneously distributed in water which was then added to the phantom. The phantom was SPECT imaged using the same setup parameters as used in Phantom Study Three. The chips were exposed to the uniformly distributed activity for an hour during the phantom preparation and SPECT imaging. Each chip was read for 30 seconds using a TLD reader* The resulting exposure, exposure rate, absorbed dose rate, and total absorbed dose at time infinity for each chip packet is shown in Table 5-15. The average absorbed dose for this study was 70 ± 12 mGy (Table 5-15). The centerline chip packets had the highest average absorbed dose rate (0.84 mGy h^{-1}) and the right panel chip packets had the lowest absorbed dose rate (0.53 mGy h^{-1}). The phantom was imaged on its side (axis parallel to the camera's AOR), with the right panel facing upward and the left panel on the bottom. The activity settled to the bottom of the phantom to expose the left panel more than the right panel.

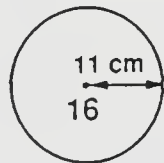
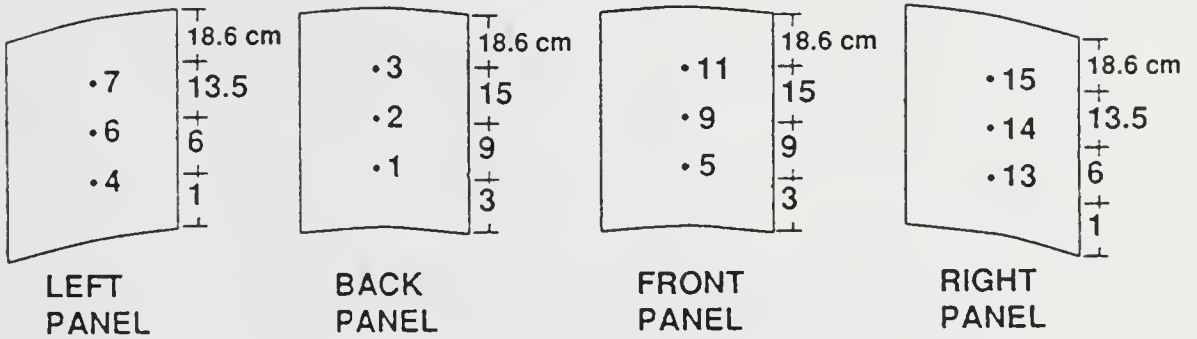
The TLD results were compared to the calculated results using the Geometric Factor Method, MIRD Pamphlet No. 3, and the Dosimetry Model (Table 5-16). Using the MIRD Pamphlet No. 3 results as the standard, the TLDs overestimated the total absorbed dose by 30%; however, this is accounted for in the standard deviation of the mean TLD absorbed dose

* Harshaw 2000 A/B, Hawshaw/Filtrol Partnership, Solon, OH 44139

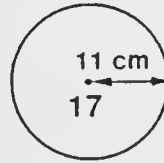


Jaszczak Phantom

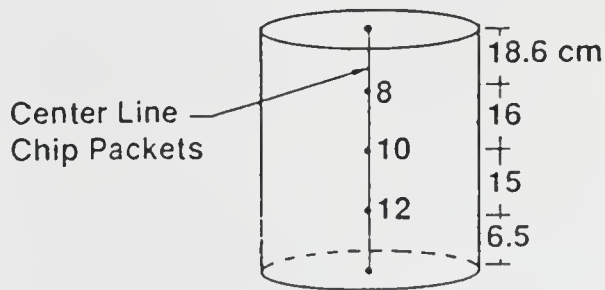
PANEL VIEW



TOP PANEL



BOTTOM PANEL



• — Chip Packet #

Figure 5-5. Phantom Study Four TLD Locations

Table 5-15. Phantom Study Four TLD Results

Location	Rate (mGy h ⁻¹)	Experiment 1 Absorbed Dose Total (mGy)
Back Panel		
1	0.798	78.2
2	0.840	82.3
3	0.719	70.5
Left Panel		
4	0.874	85.7
6	0.673	66.0
7	0.679	66.5
Front Panel		
5	0.763	74.8
9	0.730	71.5
11	0.574	56.3
Right Panel		
13	0.537	52.6
14	0.535	52.4
15	0.528	51.7
Center		
8	0.818	80.2
10	0.813	79.7
12	0.894	87.7
Top		
16	0.639	62.6
Bottom		
17	0.716	70.2
Average	0.714	69.9
Stand. Dev.*	0.120	11.8

* Stand. Dev. - Standard Deviation

Table 5-16. Phantom Study Four Results

Experiment	TLD Average Abs. Dose (mGy)	Geometric Factor Method Abs. Dose (mGy)	MIRD Pamphlet No. 3 Abs. Dose (mGy)	Dosimetry Model Abs. Dose (mGy)
1	69.9	52.8	53.6	53.4

reading, which was 12 mGy (Table 5-17). The Geometric Factor Method underestimated the total absorbed dose by one percent and the Dosimetry Model underestimated the absorbed dose by three-tenths of a percent (Table 5-17). Again, the TLD measurements were higher, but not by a factor of two or more. The higher TLD results are attributed to exposure times which were longer than those accounted for. The MIRD Pamphlet No. 3 results were expected to be higher than the Geometric Factor Method and the Dosimetry Model because it used spherical geometry, which was more efficient at absorbing dose than cylinders. There was good agreement among all of the absorbed dose methods for this experiment.

This experiment clearly showed the excellent agreement between the Dosimetry Model results and the other method results and proved that the Dosimetry Model is an accurate methodology for calculating absorbed doses in tissues whose activity is distributed homogeneously.

Clinical Study

The proposed dosimetry methodology in this research, the Dosimetry Model, was used to estimate the absorbed dose in the organs of one patient. Data from one patient participating in the clinical study being conducted at Bay Pines Veterans Medical Center was available for analysis. The absorbed dose results of patient ABG using MIRDOSE2 and the Dosimetry Model can be seen in Table 5-18. The patient

Table 5-17. Phantom Study Four Error Analysis

Standard Error between MIRD Pamphlet No. 3 Results :

Experiment	Standard Error* TLD Average (%)	Standard Error Geometric Factor Method (%)	Standard Error Dosimetry Model (%)
1	30.5	- 1.4	- 0.32

* Standard Error = $100 \times \frac{(X - \text{MIRD Pamphlet No. 3 value})}{\text{MIRD Pamphlet No. 3 value}}$

X = TLD, Geometric Factor, or Dosimetry Model value

Table 5-18. Clinical Study Results

Patient: ABG				
Organ	MIRDOSE2 Absorbed Dose (mGy)	MIRDOSE2 Volume (ml)	Dosimetry Model Absorbed Dose (mGy)	Dosimetry Model Volume (ml)
Liver	63.7	1800	547.6	301.9
Spleen	113.1	150	732.5	103.2
Tumor	n/a*	n/a	2421.5	8.9

* n/a - Not applicable (MIRDOSE2 does not calculate tumor absorbed doses)

was injected with 5.49 mCi of indium-111 labeled B72.3-GYK-DTPA. As seen in Table 5-18, the MIRDOSE2 program underestimated the absorbed doses for both the liver (factor of nine) and spleen (factor of 7) and did not calculate the absorbed dose for the tumor. The underestimation of the absorbed doses for the liver and spleen by the MIRDOSE2 program was due to the use of larger liver and spleen volumes (Table 5-18). The actual smaller volume resulting from tumor specific concentrations by the monoclonal antibody results in an expected higher absorbed dose due to the higher nonpenetrating absorbed dose component. The Dosimetry Model is felt to give a better representation of the absorbed doses in these organs.

CHAPTER 6

SUMMARY AND CONCLUSIONS

The objective of this research was to develop a foundation for a dosimetry methodology that could be used to calculate absorbed doses in target and nontarget tissues using uniformly and nonuniformly distributed activity. In this proposed methodology, a dosimetry model was developed which used Single-Photon Emission Computed Tomography (SPECT) to determine the volume and radioactive uptake in the tissues and a Monte Carlo method to determine the amount of energy deposited in the tissues.

The dosimetry model was divided into three independent models (the SPECT Model, the Monte Carlo Model, and the Dosimetry Model); whereby, each model completed a specific task. In the SPECT Model, a computer program, SPECTDOSE, was developed to calculate the target and nontarget tissue volumes and activity concentrations using a edge detection method and contour tracing algorithm. The edge detection method utilized in this research (Threshold Segmentation Method) required the use of a threshold value, a percentage of the SPECT image's maximum intensity value, to segment and extract the tissue volumes of interest from the SPECT image

for volume and activity quantitation. In the Monte Carlo Model, a monte carlo program, ALGAMP, was modified to determine the specific absorbed fractions. The results from the SPECT and Monte Carlo models were combined in the Dosimetry Model to determine the target and nontarget tissues absorbed dose.

Several phantom studies were conducted to determine the accuracy of the Dosimetry Model and to verify the ability of the Dosimetry Model to evaluate organ and tumor uptake volumes, sizes, and to calculate absorbed doses. Comparisons were made between the Dosimetry Model, other calculational methods (MIRDOSE2, Geometric Factor Method, MIRD Pamphlet No. 3), and TLD measurements.

The Standard Error of the Estimate was used to determine the best image threshold value, which was found to be affected by image noise. A higher threshold value was required to segment the image as the background image noise was increased. The image threshold value was determined for each experimental condition and range of volumes of interest.

For organ doses consistent with a diagnostic administration, the SPECT Model was found to calculate organ volumes, which were of the order of 1000 ml, to within fifteen percent of the actual volumes. The SPECT Model failed to accurately calculate organ volumes of approximately 200 ml or less with the use of the diagnostic

administration dose levels. This was due in part to the difficulty of discerning the smaller volumes from the image background noise using the Threshold Segmentation Method. Since the organ or tissue volumes were discerned on the basis of the amount of activity they contained (image intensity values), it is felt that at therapeutic dose administration levels, the SPECT Model would more accurately calculate organ size for the smaller tissue volumes. The higher tissue activities found with the use of therapeutic dose administration levels would create a large edge gradient between the tissue volumes and the image background noise, which would facilitate image segmentation by the Threshold Segmentation Method. Other image segmentation methods, such as the Gradient and Histogram methods, might be used to give a better estimate of the organ and tumor volumes when computer time and speed is not a concern. A combination of the Threshold Segmentation and Histogram Methods will be attempted in the future of this research.

The activity concentrations were not varied enough to establish a meaningful relationship between the actual and SPECT measured activity concentrations.

The radiation absorbed dose determined with the Dosimetry Model agreed within 12% to that determined by other calculational methods (Geometric Factor Method, MIRD Pamphlet No.3 results) using homogeneously and heterogeneously distributed ^{111}In . The TLD measurements were

within 30% at most of the other methods (Dosimetry Model, Geometric Factor Method, MIRD Pamphlet No. 3).

The results of the several phantom studies indicated the Dosimetry Model was working properly and that it is an appropriate methodology for calculating absorbed doses for homogeneously distributed activity. Further investigation is needed to determine the accuracy of the Dosimetry Model when heterogeneously distributed activity is used.

The MIRDOSE2 Program has been widely used for absorbed dose evaluation in nuclear medicine. In MIRDOSE2, the activity is assumed to be uniformly distributed in the source organ, which is not the case when radiolabeled monoclonal antibodies are used. This assumption, thus makes it inappropriate for use with heterogeneously distributed activity. The methodology proposed in this research provides a means of calculating absorbed doses for heterogeneously distributed activity. In comparison to MIRDOSE2, which uses the fixed organ sizes of Reference Man, the research Dosimetry Model is patient specific. The Dosimetry Model uses the organ tumor volumes of the patient of interest and calculates the specific absorbed fractions for those specific tissue volumes. MIRDOSE2 has no mechanism for calculating absorbed doses for tumors or nonstandard organs. The Dosimetry Model only requires one patient SPECT image at each time point; whereby, the MIRDOSE2 program requires several planar images to be taken at each time point to

assess the organ uptake. Thus, the Dosimetry Model reduces patient discomfort, which accompanies long image times and reduces the patient load, because the patient does not have to return for additional images. It is clear that the Dosimetry Model has several advantages over the MIRDOSE2 approach.

Corrections for photon absorption attenuation (nonlinear) and scatter and the inclusion of electron transport mechanisms were not accounted for in the development of this Dosimetry Model. Their inclusion should be considered in any further refinement of the methodology. Although not investigated in this study, new methods for determining photon absorption attenuation and scatter have been proposed. These methods include the use of simultaneous transmission and SPECT imaging and photon absorption attenuation and scattering computer simulations. The transmission image maps the object's attenuation and the buildup factors necessary for photon scatter correction (147,148). A monte carlo program has been developed which simulates photon absorption attenuation and scattering in a patient (148). The results of this program are convolved with the SPECT image raw data to remove the effects of photon absorption attenuation and scatter.

It was assumed in all the calculational methods utilized in this research that all nonpenetrating radiation was absorbed in the source organ. This assumption is

significant, in that, it overestimates the nonpenetrating absorbed dose contribution for small volumes in both the homogeneous and heterogeneous activity distribution case. Thus, it is pertinent that nonpenetrating radiation transport be included in the dosimetry methodology to accurately assess the absorbed dose in target and nontarget tissues using uniformly and nonuniformly distributed activity. An electron transport code developed at the Stanford Linear Acceleration Center (149) is being considered for future incorporation into the Dosimetry Model developed in this research.

A significant problem facing this research was the assessment of the accuracy of the absorbed dose results calculated by the research model. Phantoms were employed to assess the accuracy of the absorbed doses determined by the Dosimetry Model by comparing the results measured with TLDs and that calculated by other calculational methods (MIRDOSE2, Geometric Factor Method, MIRD Pamphlet No. 3).

The phantom absorbed dose assessment for a homogeneous activity distribution of ^{111}In showed close agreement between the four methods. No comparisons were made for the heterogeneously distributed activity case.

Only one patient was analyzed using the Dosimetry Model developed in this research; the results of which, differed greatly from those found using MIRDOSE2. No direct or indirect method of measurement in a living patient was

available for comparison with the calculational methods. Since the long term goal of the dosimetry methodology proposed in this research is to use it in human clinical studies, verification of the Dosimetry Model's results in humans will be difficult.

In this research, a foundation was developed for a dosimetry methodology that could be used to calculate absorbed doses in target and nontarget tissues using uniformly and nonuniformly distributed activity. This proposed methodology showed good agreement with the current dosimetry methods for uniformly distributed activity. But before this methodology could be used in clinical studies, several shortcomings must be resolved. This can be done by by improving the organ and tumor volume estimates by the use of other image segmentation methods or a combination of methods. The addition of photon absorbtion attenuation and scatter correction and nonpenetrating radiation transport should be considered. Phantom studies in which the range of volumes and activity concentrations simulate the range of clinical interest should also be considered.

REFERENCES

1. Rubin, P:Statement of the clinical oncologic problem. In: Clinical Oncology. Rubin P, ed., Atlanta, Ga., American Cancer Society, 1987, pp2-19.
2. Pressman D:Radiolabeled antibodies. Ann NY Acad Sci 69:644-650, 1957.
3. Kohler G,Milstein C:Continuous cultures of fused cells secreting antibody of predefined specificity. Nature 256:495-497, 1975.
4. Milstein C:Monoclonal antibodies. Sci Am 243(4):66-74, 1980.
5. Humm JL:Dosimetric aspects of radiolabeled antibodies for tumor therapy. J Nucl Med 27:1490-1497, 1986.
6. Zola H:Monoclonal Antibodies:A Manual of Techniques. Boca Raton, Florida, CRC Press, Inc., 1987.
7. Keenan AM,Harbert JC,Larson SM:Monoclonal antibodies in nuclear medicine. J Nucl Med 26:531-537, 1985.
8. Ross NR,Milgrom F,Van Oss CJ:Principles of Immunology. New York, Macmillan Publishing, 1979.
9. Weir DM:Immunology. New York, Churchill Livingstone, 1977.
10. Fawwaz RA,Wang TS,Srivastava SC,Hardy MA:The use of radionuclides for tumor therapy. Nucl Med Biol 13(4):429-436, 1986.
11. Wessels BW,Rogus RD:Radionuclide selection and model absorbed dose calculations for radilabeled tumor associated antibodies. Med Phys 11(5):638-645, 1984.
12. Williams LE,Duda RB,Proffitt RT,Beatty BG,Beatty JD, Wong JYC, Shively JE, Paxton RJ:Tumor uptake as a function of tumor mass:A mathematic model. J Nucl Med 29:103-109, 1988.

13. Hagan PL, Halpern SE, Dillman RO, Shawler DL, Johnson DE, Chen A, Krishnan L, Frincke J, Bartholomew RM, David GS, Carlo D: :Tumor size:Effect of monoclonal antibody uptake in tumor models. J Nucl Med 27:422-427, 1986.
14. Pimm MV, Baldwin RW:Effect of tumor size on monoclonal antibody uptake in tumor models. J Nucl Med 27:1788-1789, 1986.
15. Macey DJ, DeNardo SJ, DeNardo GL, DeNardo GL, Goodnight JK, Unger MW:Uptake of indium-111-labeled monoclonal antibody ZME-018 as a function of tumor size in a patient with melanoma. Amer J Physl Imag 3:1-6, 1988.
16. Cohen MB, Saxton RE, Mann B:Effect of tumor size on monoclonal antibody uptake in tumor models. J Nucl Med 27:1789-1790, 1986.
17. Larson SM:Lymphoma, melanoma, colon cancer:Diagnosis and treatment with radiolabeled monoclonal antibodies. Radio 165:297-304, 1987.
18. Douillard J-Y, Chatal J-F, Saccavini JC, Curtet C, Kremer M, Peuvrel P, Koprowski H:Pharmacokinetic study of radiolabeled anti-colorectal carcinoma monoclonal antibodies in tumor-bearing nude mice. Eur J Nucl Med 11:107-113, 1985.
19. Ballou B, Reiland J, Levine G:Tumor location using F(ab')₂ from a monoclonal IgM antibody:Pharmacokinetics. J Nucl Med 26:283-292, 1985.
20. Eger RR, Covell DG, Carrasquillo JA, Abrams PG, Foon KA, Reynolds JC, Schroff RW, Morgan AC, Larson SM, Weinstein JN:Kinetic model for the biodistribution of an In-111-labeled monoclonal antibody in humans. Cancer Res 47:3328-3336, 1987.
21. Hnatowich DJ, Griffin TW, Kosciuczyk C, Rusckowski M, Childs RL, Mattis JA, Shealy D, Doherty OW:Pharmacokinetics of In-111-labeled monoclonal antibody in cancer patients. J Nucl Med 26:849-858, 1985.
22. Fraker PJ, Speck JC:Protein and cell membrane iodinations with a sparingly soluble chloramide 1,3,4,6-tetrachloro 3a-6a-diphenyl-glycouril. Biochem Biophys Res Commun 80:849-857, 1978.
23. Gobuty AH, Kim EE, Weiner RE:Radiolabeled monoclonal antibodies:Radiochemical pharmacokinetic and clinical challenges. J Nucl Med 26:546-548, 1985.

24. Hnatowich DJ, Virzi F, Doherty PW: DTPA-coupled antibodies labeled with yttrium-90. J Nucl Med 26:503-509, 1985.
25. Larson SM: Radiolabeled monoclonal anti-tumor antibodies in diagnosis and therapy. J Nucl Med 26:538-545, 1985.
26. Goodwin DA: Pharmacokinetics and antibodies. J Nucl Med 28:1358-1362, 1987.
27. Gullino PM, Grantham FH: Studies on the exchange of fluids between host and tumor. II. The blood flow of hepatomas and other tumors in rats and mice. J Natl Cancer Inst 27:1465-1491, 1961.
28. Hosain F, Hosain P: Selection of radionuclides for therapy. In: Therapy in Nuclear Medicine. Spencer RP, ed., New York, Grune & Stratton, 1978, pp33-43.
29. Strudler PK, Larson SM: Radiolabeled monoclonal antibodies: A "decisive" technology. J Nucl Med 13:46-52, 1985.
30. d'Agincourt L: New radiopharmaceuticals opening doors for SPECT. Diag Imag June:94-100, 1986.
31. Engelstad BL, Ramos EC, Stoudemire J, O'Connell JW, Villanueva J, Faulkner DB, Hattner RS, Spitler LE, Scannon P: Improved immune-specificity in monoclonal radioimmunoimaging using dual radionuclide color functional maps. Invest Radiol 21:917-921, 1986.
32. Keenan AM, Weinstein JN, Mulshine L, Carrasquillo JA, Bunn PA, Reymolds JC, Larson SM: Immunolymphoscintigraphy in patients with lymphoma after subcutaneous injection of indium-111-labeled T101 monoclonal antibody. J Nucl Med 28:42-46, 1987.
33. Nelp WB, Eary JF, Jones RF, Hellstrom KE, Beaumier PL, Krohn KA: Preliminary studies of monoclonal antibody lymphoscintigraphy in malignant melanoma. J Nucl Med 28:34-41, 1987.
34. Perkins AC, Pimm MV: Differences in tumour and normal tissue concentrations of iodine- and indium-labelled monoclonal antibody: The effect on image contrast in clinical studies. Eur J Nucl Med 11:295-299, 1985.
35. Order SE, Stillwagon GB, Klein JL, Leichner PK, Siegelman SS, Fishman EK, Ettinger DS, Haulk T, Koper K, Finney K, Surdyke M, Self S, Leibel S: Iodine 131 antiferritin, a new treatment modality in hepatoma: A radiation therapy oncology group study. J Clin Oncol 3:1573-1582, 1985.

36. Washburn LC, Hwa Sun TT, Crook JE, Byrd BL, Carlton JE, Hung Y-W, Steplewski ZS: ^{90}Y -labeled monoclonal antibodies for cancer therapy. Nucl Med Biol 13:453-456, 1986.
37. Childs RL, Hnatowich DJ: Optimum conditions for labeling of DTPA-coupled antibodies with Technetium-99m. J Nucl Med 26:293-299, 1985.
38. Rhodes BA, Zamora PO, Newell KD, Valdez EF: Technetium-99m labeling of murine monoclonal antibody fragments. J Nucl Med 27:685-693, 1986.
39. Goldenberg DM, Ford EH, Lee RE, Hall TC, Horowitz JA, Sharkey RM, Hansen HJ: A new 99m-Tc labeling system for cancer radioimmunodetection. Fourth International Conference on Monoclonal Antibody Immunoconjugates for Cancer, San Diego, March 1989, p24.
40. Chen DCP, Pascal SG, Siegel ME, Liggett PE, Kempf RA, Payne D, Smith R: Radioimmunodetection of uveal and cutaneous melanomas with Tc99m labeled monoclonal antibody. Fourth International Conference on Monoclonal Antibody Immunoconjugates for Cancer. San Diego, March 1989, p126.
41. Leichner PK, Klein JL, Garrison JB, Jenkins RE, Nickoloff EL, Ettinger DS, Order SE: Dosimetry of ^{131}I -labeled antiferritin in hepatoma: A model for radioimmunoglobulin dosimetry. Intl J Oncol Biol Phys 7:323-333, 1981.
42. Freiherr G: Monoclonal antibodies against cancer: Clinical application. Res Resources Rpt 8:1-8, 1984.
43. Harrison A, Royle L: Preparation of a ^{211}At -IgG conjugate which is stable in vivo. Int J Appl Radiat Isot 35:1005-1008, 1984.
44. Vaughan ATM, Bateman WJ, Fisher DR: The in vivo fate of ^{211}At labeled monoclonal antibody with known specificity in a murine system. Int J Radiat Onc Biol Phys 8:1943-1946, 1982.
45. Macklis RM, Kinsey BM, Kassis AI, Ferrara JLM, Atcher RW, Hines JJ, Coleman CN, Adelstein SJ, Burakoff SJ: Radioimmunotherapy with alpha-particle-emitting immunoconjugates. Science 240:1024-1026, 1988.

46. Simonson RB, Ultee ME, Hauler JA, Alvarez VL: Radioimmunotherapy of peritoneal human colon cancer xenografts with site-specifically ^{212}Bi -labeled antibody. Fourth International Conference on Monoclonal Antibody Immunoconjugates for Cancer. San Diego, March 1989, p142.
47. Hnatowich DJ, Chinal M, Siebecker DA, Gionet M, Griffin T, Doherty PW, Hunter R, Kase KR: Patient biodistribution of intraperitoneally administered Yttrium-90-labeled antibody. J Nucl Med 29:1428-1434, 1988.
48. Royston I, Parker BA, Vassos A, Hupf H, Amox D, Green MR, Miller R, Halpern S: ^{90}Y anti-idiotypic monoclonal antibody therapy of Non-Hodgkin's lymphoma. Fourth International Conference on Monoclonal Antibody Immunoconjugates for Cancer. San Diego, March 1989, p142.
49. Vriesendorp HM, Stinson R, Onyekwere O, Leichner P, Klein J, Wessels B, Williams J: Bone marrow toxicity of polyclonal antiferritin in rat, dog and man. Fourth International Conference on Monoclonal Antibody Immunoconjugates for Cancer. San Diego, March 1989, p142.
50. Crook JE, Washburn LC, Lee Y-CC, Byrd BL, Sun TTH, Steplewski Z: Tissue distribution of ^{90}Y -labeled monoclonal antibody CO17-1A in young and old athymic mice. Fourth International Conference on Monoclonal Antibody Immunoconjugates for Cancer. San Diego, March 1989, p142.
51. DeNardo SJ, Meares CF, Deshpande SV, Moi MK, McCall MJ: Remarkably stable metal chelates for radioimmunotherapy with Cu-67 and Y-90. Fourth International Conference on Monoclonal Antibody Immunoconjugates for Cancer. San Diego, March 1989, p142.
52. Lee Y-CC, Washburn LC, Sun TTH, Byrd BL, Crook JE, Steplewski Z: Radiotherapy of human colorectal carcinoma xenografts using Y-90-labeled CO17-1A. Fourth International Conference on Monoclonal Antibody Immunoconjugates for Cancer. San Diego, March 1989, p142.
53. DeNardo SJ, Jungerman JA, DeNardo GL, Lagunas-Solar MC, Cole WC, Meares CF: The choice of radionuclides for radioimmunotherapy. Proceedings of the International Symposium of the Developing Role of Short-lived Radionuclides in Nuclear Medicine Practice, Davis, CA., DOE Publication, pp401-414.

54. Fawwaz RA, Wang TST, Srivastava AC, Rosen JM, Ferrone S, Hardy MA, Alderson PO: Potential of Palladium-109-labeled antimelanoma monoclonal antibody for tumor therapy. J Nucl Med 25:796-799, 1984.
55. Schroff R, Hanelin L, Vanderheyden J-L, Fer M, Weiden P, Breitz H, Fisher D, Abrams P, Ratliff B, Appelbaum J, Morgan C, Fritzberg A: Preliminary clinical evaluation of a Re-186 labeled anti-CEA F(ab')₂ antibody fragment as a potential radioimmunotherapy agent. Fourth International Conference on Monoclonal Antibody Immunoconjugates for Cancer. San Diego, March 1989, p142.
56. Khaw BA, Bailes JS, Schneider SL, Lancaster J, Powers J, Strauss HW, Laster JC, McGuire WL: Human breast tumor imaging using ¹¹¹In labeled monoclonal antibody: Athymic mouse model. Eur J Nucl Med 14:362-366, 1988.
57. Pedley RB, Boden J, Keep PA, Harwood PJ, Green AJ, Rogers GT: Relationship between tumour size and uptake of radiolabeled anti-CEA in a colon tumour xenograft. Eur J Nucl Med 13:197-202, 1987.
58. Davis KH: Use of Gallium-67 citrate and Indium-111 monoclonal antibodies in the detection of metastatic melanoma. J Nucl Med Tech 15:25-29, 1987.
59. Matzku S, Schuhmacher J, Kirchgebner H, Brugger J: Labeling of monoclonal antibodies with a ⁶⁷Ga-phenolic aminocarboxylic acid chelate. Part II: Comparison of immunoreactivity and biodistribution of monoclonal antibodies labeled with ⁶⁷Ga-chelate or with ¹³¹I. Eur J Nucl Med 12:405-412, 1986.
60. Ward MC, Roberts KR, Westwood JH, Coombes RCC, McCready VR: The effect of chelating agents on the distribution of monoclonal antibodies in mice. J Nucl Med 27:1746-1750, 1986.
61. Goodwin DA, Meares CF, McCall MJ, Haseman MK, McTigue M, Diamond CI, Chaovapong W: Chelate conjugates of monoclonal antibodies for imaging lymphoid structures in the mouse. J Nucl Med 26:493-502, 1985.
62. Esteban JM, Schlom J, Gansow OA, Atcher RW, Brechbeil MW, Simpson DE, Colcher D: New method for the chelation of Indium-111 to monoclonal antibodies: Biodistribution and imaging of athymic mice bearing human colon carcinoma xenografts. J Nucl Med 28:861-870, 1987.

63. Folkman J:How is blood vessel growth regulated in normal neoplastic tissue?-GHA Clowes Memorial Award Lecture. Cancer Res 46:467-473, 1986.
64. Anghileri LJ,Crone-Escanye MC,Thouvenot P,Brunotte F, Robert J:Mechanisms of gallium-67 accumulation by tumors:Role of cell membrane permeability. J Nucl Med 29:663-668, 1988.
65. Winchell HS:Mechanisms for localization of radiopharmaceuticals in neoplasms. Semin Nucl Med 6:371-378, 1976.
66. Leichner PK,Klein JL,Order SE:Dosimetric considerations in radioimmunotherapy of patients with hepatoma. Proceedings of the Fourth International Radiopharmaceutical Dosimetry Symposium, Schlafke-Stelson AT,Watson EE, eds., Oak Ridge Associated Universities, Oak Ridge, Tennessee, November 1985, pp477-492.
67. Belliveau RE,Witek JT:Possible therapeutic use of radiolabeled antibodies:A review. Therapy in Nuclear Medicine. Spencer RP, ed., New York, Grune & Stratton, Inc., 1978, pp295-303.
68. Hagan PL,Halpern SE,Chen A,Krishnan L,Frincke J,Bartholomew RM,David GS,Carlo D:In vivo kinetics of radiolabeled monoclonal anti-CEA antibodies in animal models. J Nucl Med 26:1418-1423, 1985.
69. Pimm MV,Baldwin RW:Comparative biodistributions and rates of catabolism of radiolabelled anti-CEA monoclonal antibody and control immunoglobulin in nude mice with human tumour xenografts showing specific antibody localization. Eur J Nucl Med 13:258-263, 1987.
70. Gatenby RA,Moldofsky PJ,Weiner LM:Metastatic colon cancer:Correlation of oxygen levels with I-131 F(ab')₂ uptake. Radio 166:757-759, 1988.
71. Dillman RO:Overview of the clinical problem of human antimouse antibodies. Fourth International Conference on Monoclonal Antibody Immunoconjugates for Cancer. San Diego, March 1989, p61.
72. Scannon PJ:Suppression of the human immune response to immunotoxins with drugs. Fourth International Conference on Monoclonal Antibody Immunoconjugates for Cancer. San Diego, March 1989, p62.

73. Myers MJ: Dosimetry for radiolabelled antibodies-macro or micro? Int J Cancer Supplement 2:71-73, 1988.
74. Loevinger R, Berman M: A schema for absorbed dose calculations for biologically-distributed radionuclides. J Nucl Med 9:9-14, 1968.
75. Berger MJ: Distribution of absorbed dose around point sources of electrons and beta particles in water and other media. J Nucl Med 12, Supplement 5:5, 1971.
76. Diel JH: Microdosimetry of internally deposited radionuclides. Int J Appl Radiat Isot 33:967-979, 1982.
77. Loevinger R, Budinger TF, Watson EE: MIRD Primer for Absorbed Dose Calculations. New York, The Society of Nuclear Medicine, 1988, pp 1-21.
78. Myers MJ, Epenetos AA, Hooker G: Practical assessment of radiation doses using labelled antibodies for therapy. Nucl Med Biol 13:437-446, 1986.
79. Myers MJ, Hooker GR, Epenetos AA: Dosimetry of radiolabeled monoclonal antibodies used for therapy. Proceedings of the Fourth International Radiopharmaceutical Dosimetry Symposium, Schlafke-Stelson AT, Watson EE, eds., Oak Ridge Associated Universities, Oak Ridge, Tennessee, November 1985, pp477-492.
80. Dillman LT, Von der Lage FC: Radionuclide decay schemes and nuclear parameters for use in radiation-dose estimation. Medical Internal Radiation Dose (MIRD) Pamphlet 10, revised. New York, Society of Nuclear Medicine, September 1975.
81. ICRU Report 32: Methods of Assessment of Absorbed Dose in Clinical Use of Radionuclides. Washington D.C., International Commission on Radiation Units and Measurements, 1979.
82. Loevinger R, Holt JG, Hine GJ: Internally administered radioisotopes. Radiation Dosimetry. New York, Academic Press, 1956, p804-821.
83. Berger MJ: Beta-ray dosimetry calculations with the use of point kernels. Medical Radionuclides: Radiation Dose and Effects Proceedings, Oak Ridge Associated Universities, Oak Ridge, Tennessee, December 1969, AEC-20, pp63-86.

84. Spencer RP:Applied principles of radiopharmaceutical use in therapy. Nucl Med Biol 13:461-463, 1986.
85. Fisher DR:The microdosimetry of monoclonal antibodies labeled with alpha emitters. Proceedings of the Fourth International Radiopharmaceutical Dosimetry Symposium. Schlafke-Stelson AT,Watson EE, eds., Oak Ridge Associated Universities, Oak Ridge, Tennessee, November 1985, pp26-36.
86. ICRU Report 33:Radiation quantities and units. Washington D.C., International Commission on Radiation Units and Measurements, 1980.
87. Bigler RE,Zanzonico PB,Cosma M:Adjuvant radioimmunotherapy for micrometastases:A strategy for cancer cure. Radiolabeled Monoclonal Antibodies for Imaging and Therapy. Srivastava SC, ed., New York, Plenum Publishing Corp., 1988, pp409-430.
88. Eckerman KF,Ryman JC,Taner AC,Kerr GD:Traversal of cells by radiation and absorbed fraction estimates for electrons and alpha particles. Proceedings of the Fourth International Radiopharmaceutical Dosimetry Symposium. Schlafke-Stelson AT,Watson EE, eds., Oak Ridge Associated Universities, Oak Ridge, Tennessee, November 1985, pp67-81.
89. Adelstein SJ,Kassis AI,Sastry KSR:Cellular vs organ approaches to dose estimates. Proceedings of the Fourth International Radiopharmaceutical Dosimetry Symposium. Schlafke-Stelson AT,Watson EE, eds., Oak Ridge Associated Universities, Oak Ridge, Tennessee, November 1985, ppl3-
90. Rao DV,Govelitz GF,Sastry KSR,Howell RW:Spermatogonial cell killing by radiolabeled methionine:A comparative study of the effects of Se-75, S-35, and H-3. Proceedings of the Fourth International Radiopharmaceutical Dosimetry Symposium. Schlafke-Stelson AT,Watson EE, eds., Oak Ridge Associated Universities, Oak Ridge, Tennessee, November 1985, pp52-66.
91. Langmuir VK:Dosimetry models for radioimmunotherapy. Med Phys 15(6):867-873, 1988.
92. O'Donoghue JA,Wheldon TE:Predicted allowable doses to normal organs for biologically targeted radiotherapy. Br J Radiol 61:264-266, 1988.
93. Vaughan ATM,Anderson P,Dykes PW,Chapman CE,Bradwell AR:Limitations to the killing of tumours using radiolabelled antibodies. Br J Radio 60:567-578, 1987.

94. Griffith MH, Wijewardene C, Wessels BW: Micro TLD and autoradiographic measurements for radiolabeled antibody uptake in tumor bearing mice. Med Phys 12(5):872, 1985
95. Griffith MH, Yorke ED, Wessels BW, DeNardo GL, Neacy WP: Direct dose confirmation of quantitative autoradiography with micro-TLD measurements for radioimmunotherapy. J Nucl Med 29:1795-1809, 1988.
96. Wessels BW, Griffith MH: Miniature thermoluminescent dosimeter absorbed dose measurements in tumor phantom models. J Nucl Med 27:1308-1314, 1986.
97. Ryman JC, Warner GG, Eckerman KF: ALGAMP-a Monte Carlo radiation transport code for calculating specific absorbed fractions of energy from internal or external photon sources. ORNL/TM-8377, 1986.
98. Cristy M: Mathematical phantoms representing children of various ages for use in estimates of internal dose. NUREG/CR-1159, ORNL/TM-367, 1980.
99. Croft BY: Single-Photon Emission Computed Tomography. Chicago, Year Book Medical Publishers, Inc., 1986, pl.
100. Jaszczak RJ, Greer KL, Coleman RE: SPECT quantification of regional radionuclide distributions. Proceedings of the Fourth International Radiopharmaceutical Dosimetry Symposium. Schlafke-Stelson AT, Watson EE, eds., Oak Ridge Associated Universities, Oak Ridge, Tennessee, November 1985, pp82-96.
101. Iosilevsky G, Israel O, Frenkel A, Even-Sapir E, Ben-Haim S, Front A, Kolodny GM, Front D: A practical SPECT technique for quantification of drug delivery to human tumors and organ absorbed radiation dose. Semin Nucl Med XIX:33-46, 1989.
102. Jaszczak RJ, Coleman RE, Whitehead FR: Physical factors affecting quantitative measurements using camera-based single photon emission computed tomography (SPECT). IEEE Trans Nucl Sci NS-28:69-80, 1981.
103. Cember H: Introduction to Health Physics. New York, Pergamon Press, 1983, pl11.
104. Axelsson B, Israelsson A, Larsson SA: Studies of a technique for attenuation correction in single photon emission computed tomography. Phys Med Biol 32:737-749, 1987.

105. Bailey DL, Hutton BF: The accuracy of SPECT attenuation correction using simultaneous transmission and emission tomography. J Nucl Med 28:677, 1987.
106. Chang, LT: A method for attenuation correction in radionuclide computed tomography. IEEE Trans Nucl Sci NS-25:638-643, 1978.
107. Galt JR, Hamilton DR, Garcia EV: SPECT quantitation: Attenuation correction in inhomogeneous media utilizing a transmission scan and assigned attenuation coefficients. J Nucl Med 26:797-798, 1988.
108. Guzzardi R, Licitra G: Three dimensional attenuation coefficients distribution for SPECT of the chest. J Nucl Med 28:128-129, 1987.
109. Keller AM, Simon TR, Smitherman TC, Mellay CR, Dehmer GJ: Direct determination of the attenuation coefficient for radionuclide volume measurements. J Nucl Med 28:102-107, 1987.
110. Lembcke TM, Ficken VJ, Allen EW: Optimum energies for dual energy attenuation correction in SPECT. J Nucl Med 30:5ab, 1989.
111. Malko JA, Van Heertum RL, Gullberg GT, Kowalski WP: SPECT liver imaging using an iterative attenuation correction algorithm and an external flood source. J Nucl Med 27:701-705, 1986.
112. Manglos SH, Jaszczak RJ, Floyd CE, Hahn LJ, Greer KL, Coleman RE: Nonisotropic attenuation in SPECT: Phantom tests of quantitative effects and compensation techniques. J Nucl Med 28:1584-1591, 1987.
113. Marshall CH: Absolute values of attenuation coefficient in computed tomography. Phys Med Biol 24:828, 1979.
114. Pellettier JL, Touzery C, Coitoux P: Relative efficiency of attenuation correction algorithms for emission tomography: Results from simulated data. Proceedings of the Third World Congress of Nuclear Medicine and Biology I:510-513, 1982.
115. Tsui BMW, Gullberg GT, Edgerton ER, Ballard JG, Perry JR, McCartney WH, Berg J: Correction of nonuniform attenuation in cardiac SPECT imaging. J Nucl Med 30:497-507, 1989.
116. Walters TE, Simon W, Chesler DA, Correia JA: Attenuation correction in gamma emission computed tomography. J Comp Ass Tomo 5:89-94, 1981.

117. Webb S, Flower MA, Ott RJ, Leach MO: A comparison of attenuation correction methods for quantitative single photon emission computed tomography. Phys Med Biol 28:1045-1056, 1983.
118. Zhang CG, DeNardo GL, Macey DJ, DeNardo SJ, Custer T: Determination of the attenuation correction factor (ACF) from a transmission image for absolute quantitation of radionuclide. J Nucl Med 29:872, 1988.
119. Todd-Pokropek A: The elimination of non-stationary effects as part of attenuation scatter and PSF correction in tomography. J Nucl Med 28:660-661, 1987.
120. Heller SL, Goodwin PN: SPECT instrumentation: Performance, lesion detection, and recent innovations. Semin Nucl Med Vol XVII:184-199, 1987.
121. Beck JW, Jaszczak RJ, Starmer CF: The effect of Compton scattering on quantitative SPECT imaging. Proceedings of the Third World Congress of Nuclear Medicine and Biology I:1042-1045, 1982.
122. Axelsson B, Msaki P, Israelsson A: Subtraction of Compton-scattered photons in single-photon emission computerized tomography. J Nucl Med 25:490-494, 1984.
123. Bloch P, Sanders T: Reduction of the effects of scattered radiation on a sodium iodide imaging system. J Nucl Med 14:67-72, 1972.
124. Egbert SD, May RS: An integral-transport method for Compton-scatter correction in emission computed tomography. IEEE Trans Nucl Sci NS-27:543-547, 1980.
125. Floyd CE, Jaszczak RJ, Greer KL, Coleman RE: Deconvolution of Compton scatter in SPECT. J Nucl Med 26:403-408, 1985.
126. Jaszczak RJ, Greer KL, Floyd CE: Improved SPECT quantification using compensation for scattered photons. J Nucl Med 25:893-900, 1984.
127. Koral KF, Swailen FM, Buchbinder S, Clinthorne NH, Rogers WL, Tsui BMW: In SPECT dual-energy-window Compton correction, is the k value object invariant? J Nucl Med 29:797, 1988.
128. Koral KF, Buchbinder S, Clinthorne NH, Rogers WL, Tsui BMW, Edgerton ER: Compensation for attenuation and Compton-scattering in absolute quantification of tumor activity. J Nucl Med 28:577, 1987.

129. Koral KF,Wang X,Clinthorne NH,Rogers WL,Floyd CE,Jaszczak RJ:Compton-scatter estimation by spectral fitting: Reproducibility comparison to monte carlo simulation. J Nucl Med 26:797, 1988.
130. Logan KW,McFarland WD:Direct scatter compensation by photopeak distribution analysis. J Nucl Med 29:797, 1988.
131. ADAC Laboratories Version 4 Operator's Manual, pE32-18, 1987.
132. Budinger TF,Gullberg GT:Three-Dimensional reconstruction in nuclear medicine emission imaging. IEEE Trans Nucl Sci NS-21:2-20, 1974.
133. Oppenheim BE:More Accurate algorithms for iterative-dimensional reconstruction. IEEE Trans Nucl Sci NS-91:72-77, 1972.
134. ADAC Laboratories Rotational Tomography Manual, pp4.12-4.13, 1987.
135. ADAC Laboratories Rotational Tomography Manual, p4.6, 1987.
136. Gonzalez RC,Wintz P:Digital Image Processing. Massachusetts, Addison-Wesley Publishing Company, Inc., 1987, p331.
137. Gonzalez RC,Wintz P:Digital Image Processing. Massachusetts, Addison-Wesley Publishing Company, Inc., 1987, p334-340.
138. Gonzalez RC,Wintz P:Digital Image Processing. Massachusetts, Addison-Wesley Publishing Company, Inc., 1987, p144-158.
139. Gonzalez RC,Wintz P:Digital Image Processing. Massachusetts, Addison-Wesley Publishing Company, Inc., 1987, p354-368.
140. ADAC Laboratories Version 4 Operator's Manual, pE32-8, 1987.
141. Stabin M:MIRDOSE2 Program. Oak Ridge, Tennessee, Oak Ridge Associated Universities, 1985.
142. Budnitz RJ,Nero AV,Murphy DT,Graven R:Instrumentation For Environmental Monitoring. Berkeley, California, John Wiley & Sons, Inc., 1983, pp285-288.

143. Bennett JM:Basic Concepts in investigational therapeutics. In:Clinical Oncology. Rubin P, ed., New York, American Cancer Society, 1983, pp96-99.
144. Focht EF,Quimpy EH,Gershowitz M:Revised Average Geometric Factors for Cylinders in Isotope Dosage. Part I. Radiology 85:151-152, 1965.
145. Cember H:Introduction to Health Physics. New York, Pergamon Press, 1983, pp135-155.
146. Brownell GL,Ellett WH,Reddy AR:MIRD Pamphlet 3:Absorbed Fractions for Photon Dosimetry. J Nucl Med Supplement No. 1:29-39, 1968.
147. Siegel JA, Lee RA,Steimle VS,Pawlyk DA,Khalvati S,Murthy S,Front D,Horowitz JA,Sharkey RM,Goldenberg DM:Monoclonal antibody (Mab) image quantitation using the buildup factor. J Nucl Med 31:783, 1990.
148. Ljungberg M:Development and Evaluation of Attenuation and Scatter Correction Techniques for SPECT Using the Monte Carlo Method. Sweden, Ljungbergs Tryckeri AB, Klippan, 1990.
149. Oak Ridge National Laboratory Radiation Shielding Information Center, Oak Ridge, Tennessee 37831.

APPENDIX A
SAMPLE CALCULATIONS

Calculations made using the MIRDOSE2 Program, the Geometric Factor Method, MIRD Pamphlet No. 3, the Dosimetry Model, and in the phantom studies, utilized the procedures and formulas given in this appendix. Sample calculations are given below for each dosimetry method:

MIRDOSE2 Program:

Biodistribution and organ planar uptake data are fitted by an exponential curve using the program Plot, which is included along with the MIRDOSE2 program. The organ residence times are determined from the curve fits. The effective half-life is assumed to be infinite and equal to the physical half-life (T_p). The residence times are then inputted into MIRDOSE2 to determine the absorbed doses:

$$\text{Residence Time} = 1.443 \times T_p \times \text{Organ Uptake}$$

$$\text{Absorbed Dose} = A_0 \times \text{MIRDOSE2 results (Gy/MBq injected)}$$

Geometric Factor Method:

$$D = C \times \Gamma \times g$$

$$\Gamma = \text{Specific Gamma-Ray Emission} = 3.65\text{E-}09 \times \sum n_i E_i$$

$$n_{172} = 0.8959 \quad E_{172} = 0.172 \text{ Mev}$$

$$n_{247} = 0.9395 \quad E_{247} = 0.247 \text{ Mev}$$

$$\begin{aligned} \Gamma(^{111}\text{In}) &= 3.65\text{E-}09 \times [(0.8959)(0.172) + (0.9395)(0.247)] \\ &= 1.409\text{E-}09 \quad \text{C Kg}^{-1} \text{ m}^2 \text{ MBq}^{-1} \text{ h}^{-1} \end{aligned}$$

$$\begin{aligned} C = \text{Activity Concentration} &= 1.25\text{E-}03 / 6032.5 \\ &= 7.667\text{E-}03 \quad \text{MBq m}^3 \end{aligned}$$

$$g = 89.6 \text{ cm} = 0.896 \text{ m}$$

$$\begin{aligned} D &= 7.667\text{E+}03 \times 1.409\text{E-}09 \times 0.896 \\ &= 9.679\text{E-}06 \text{ C Kg}^{-1} \text{ h}^{-1} \end{aligned}$$

$$D = (9.679\text{E-}06 \text{ C Kg}^{-1} \text{ h}^{-1}) \times (37 \times \mu_m/p_m/\mu_a/p_a) \text{ Gy h}^{-1}$$

$$\begin{aligned} \mu_m/p_m &= \text{Mass Energy-Absorption Coefficient of Tissue} \\ &= 0.0299 \text{ cm}^2 \text{ g}^{-1} \end{aligned}$$

$$\mu_a/p_a = \text{Mass Energy-Absorption Coefficient of Air} \\ = 0.0268 \text{ cm}^2 \text{ g}^{-1}$$

$$D = 9.679\text{E-}06 \times 37 \times 0.0299/0.0268 \\ = 3.995\text{E-}04 \text{ Gy h}^{-1}$$

$$D_{ep} = \text{Penetrating Absorbed Dose at infinity} \\ = 1.443 \times T_p \times D$$

$$T_p = \text{Physical Half-Life} = 67.92 \text{ h}$$

$$D = \text{Absorbed Dose Rate (Gy h}^{-1}\text{)}$$

$$D_{ep} = 1.443 \times 67.92 \times 3.995\text{E-}04 \\ = 39.17 \text{ mGy}$$

$$D_{enp} = \text{Nonpenetrating Absorbed Dose at Infinity} \\ = 1.443 \times T_p \times A \times \sum_i E_i$$

$$A = \text{Activity } \mu\text{Ci}$$

$$D_{enp} = 1.443 \times 67.92 \text{ h} \times 1250 \mu\text{Ci} \times [(0.1197)(0.166)] \times \\ (0.001 \text{ Kg g}^{-1}) \\ = 24.34 \text{ mGy}$$

$$D_o = D_{ep} + D_{enp} = 63.5 \text{ mGy}$$

MIRD Pamphlet No. 3:

$$\Phi_{172} = 0.2365/6 = 0.0394 \text{ Kg}^{-1}$$

$$\Phi_{247} = 0.2398/6 = 0.0400 \text{ Kg}^{-1}$$

$$\Delta_{172} = 0.3282 \text{ g rad } \mu\text{Ci}^{-1} \text{ h}^{-1}$$

$$\Delta_{247} = 0.4942 \text{ g rad } \mu\text{Ci}^{-1} \text{ h}^{-1}$$

$$D_o = 1.443 \times T_p \times A \times \sum_i \Delta_i \Phi_i \\ = 1.443 \times 67.92 \times 1250 \times [(0.3282)(0.0394) + \\ (0.4942)(0.0400) + (0.1197)(0.166)] \times \\ 0.001 \text{ Kg g}^{-1} \\ = 64.4 \text{ mGy}$$

Dosimetry Model:

Specific Absorbed Fractions (SAF) determined in the Monte Carlo Model are used along with the injected activity (A_0) and radionuclide energy parameters to determine the absorbed doses:

$$D_o = 1.443 \times T_p \times A_0 \times [(2.13 \sum_i E_i \times \text{SAF}_p) + (2.13 \sum_i E_i \times \text{SAF}_{np})]$$

$$\Delta_p = 2.13 \sum_i E_i = 0.8224 \quad \text{g rad } \mu\text{Ci}^{-1} \text{ h}^{-1}$$

$$\Delta_{np} = 2.13 \sum_i E_i = 0.1197 \quad \text{g rad } \mu\text{Ci}^{-1} \text{ h}^{-1}$$

$$\begin{aligned} D_o &= 1.443 \times 67.92 \times 1250 \times [(0.8224)(0.03366) + (0.1197)(0.166)] \times 0.001 \\ &= 58.3 \text{ mGy} \end{aligned}$$

Standard Error:

$$\begin{aligned} \text{Standard Error} &= ((X - \text{MIRD Pamphlet No. 3 result}) / \text{MIRD Pamphlet No. 3 result}) \times 100\% \\ &= ((278.4 - 64.4) / 64.4) \times 100\% \\ &= 332.3\% \end{aligned}$$

X = TLD result, or Geometric Factor Method result, or Dosimetry Model result

APPENDIX B
TLD CALIBRATION

The TLDs used in Phantom Study Three were calibrated using a radium needle source to relate the exposure reading to absorbed dose. The radium needle's exposure rate was $4.00\text{E-}07$ C Kg⁻¹. Two TLD cards (two TLD chips each) were exposed to the radium needle for a specified length of time for a total of four time intervals. The resulting TLD measurements (nC) are correlated with the radium needle exposures (mR). The following correlation was found between the TLD readings and the radium needle exposure:

$$\text{Exposure (mR)} = 67.5 \times \text{TLD measurement (nC)} + 20.9$$

The exposure results were converted to absorbed dose rate by using the mass energy-absorption coefficients and a constant.

$$\text{Absorbed Dose Rate} = \text{Exposure} \times 37 \times \mu_m/p_m / \mu_a/p_a$$

$$\begin{aligned} \mu_m/p_m &= \text{mass energy-absorption coefficient in tissue} \\ &= 0.0299 \text{ cm}^2 \text{ g}^{-1} \end{aligned}$$

$$\begin{aligned} \mu_a/p_a &= \text{mass energy-absorption coefficient in air} \\ &= 0.0268 \text{ cm}^2 \text{ g}^{-1} \end{aligned}$$

$$\text{Absorbed Dose (at } \infty) = 1.443 \times T_p \times \text{Absorbed Dose Rate}$$

APPENDIX C
SPECTDOSE PROGRAM

The following pages of this appendix contain the computer code developed for the program SPECTDOSE. This program is written in Fortran-77* for a Vax/VMS Operating System**.

* American National Standard X3.9-1978

** Digital Equipment Corporation, Chelmsford, MA 01824

Program SPECT_Dose

```

c
c   This program uses SPECT images to calculate object
c   volumes, store pixel locations, and pixel count.
c
c***** Written by Latresia A. Wilson *****
c
Integer ia(262144),es,bs,ds,ac,rd,proj(64,64),ch,imm
Integer sat,choice,tv,cum
Integer*4 bslice,eslice,m,slice,s
Real*4 threshold,u,ad,atten,thalf,chalf,lambda
Real*4 ct,decay
Logical*1 a(262144)
Logical aa(262144)
Character fname*40
Common pixel

c
c*****
c
c   cum=0
5   Call menu
   read(5,*)choice
   if((choice .gt. 5).or.(choice .lt. 1))then
   write(6,*)'Choice must be between 1 and 5, Try Again!'
   go to 5
   end if
   if(choice .eq. 2)then
   if(sat .eq. 1)go to 6
   write(6,*)'Enter the Number of Object Files:'
   read(5,*)imm
6   cum=cum+1
   if(cum .gt. 1)go to 17
   open(unit=7,file='voxel',status='new')
   go to 17
   end if
   if(choice .eq. 3)go to 18
   if(choice .eq. 4)go to 19
   if(choice .eq. 5)go to 1501
1  write(6,*) 'The maximum image size is 64*64'
   write(6,*) 'The default directory is $Disk[account.
   current]:'
   write(6,*) ' '
   write(6,*) 'Enter the Directory and Filename:'
   read(5,800)fname
800 format(a34)
   write(6,*) 'The maximum number of image slices is 64.'
11  write(6,*) 'Enter the beginning and ending slice number
   (1,64=all):'
   read(5,*)bs,es
   ds=es-bs
   if(ds .GT. 64) then

```

```

write(6,*) 'Maximum number of slices is 64, Try Again!'
go to 11
end if
bslice=((bs-1)*4096)/512 + 1
eslice=(es*4096)/512
write(6,*) 'Enter the Image Pixel Size (cm):'
read(5,*)pixel
write(6,*) 'Do you want to Correct for Attenuation
(1-Yes,0-No)?'
read(5,*)ac
atten=1
if(ac .eq. 1) then
write(6,*) 'Enter the Attenuation Coefficient (cm-1):'
read(5,*)u
write(6,*) 'Enter the Attenuated Distance (Organ
Depth)(cm):'
read(5,*)ad
atten=exp(u*ad)
end if
write(6,*) 'Do you want to Correct for Radioactive
Decay (1-Yes,0-No)?'
read(5,*)rd
decay=1
if(rd .eq. 1) then
write(6,*) 'Enter the Radioactive Halflife (days):'
read(5,*)Thalf
chalf=1440*thalf
lambda=0.693/chalf
write(6,*) 'Enter Correction Time (min):'
read(5,*)ct
decay=exp(lambda*ct)
end if

```

C

C*****

```

open(unit=4, file=fname, access='direct', status='old')

```

```

do 10 i=bslice, eslice

```

```

k=(i-1)*512

```

```

read(4, rec=i) (a(k+j), j=1, 512)

```

```

do 20 j=1, 512

```

```

aa(k+j)=a(k+j)*atten*decay

```

```

int=aa(k+j)

```

```

if(int .lt. 0) int=int+256

```

```

ia(k+j)=int

```

```

20 continue

```

```

10 continue

```

C-----

C For each slice, read values into matrix proj()

```

s=(bs-1)*4096

```

```

Write(6,*) 'If Threshold Value the same for all slices,
Enter 1:'

```

```

read(5,*)tv

```

```

if(tv .eq. 1) then

```

```

write(6,*) 'Enter the Threshold Value for all Slices:'
read(5,*)threshold
end if
c   open objval.dat file
    open(unit=1,file='objval',status='new')
    write(1,705)
705  format(' z',2x,'Obj',1x,'6ox',1x,'Totct',3x,'Avgct',2x,
1    'Volume',2x,'Width',1x,'Length',1x,'Area',1x,
2    'Center',1x,'Minx',1x,'Maxx',1x,'Miny',1x,'Maxy')
    do 30 slice=bs,es
      do 40 i=1,64
        m=(i-1)*64+s
        do 50 j=1,64
          proj(i,j)=ia(j+m)
50     continue
40     continue
        s=slice*4096
c-----
c   Call threshold method to segment image
    if(tv .eq. 1)go to 15
    write(6,*)' For Slice=',slice,' Enter its Threshold:'
    read(5,*)threshold
15   if(slice .eq. bs)imm=1
      call thold(proj,threshold,slice,imm)
c-----
30   continue
      close(unit=1)
      imm=imm-1
      sat=1
      go to 5 17
      call objselect(imm)
      go to 5
18   call corgan
      go to 5
19   call voxfil
      go to 5
c*****
1500 close(unit=7)
1501 stop
end

```

Subroutine Menu

```
c
c   This subroutine displays a menu of choices
c.....
c   write(6,*)'Choose the Number of the Option of your
      Choice:'
      write(6,*)' '
      write(6,*)'1) Image Segmentation by Threshold Method'
      write(6,*)'2) Object Extraction and Volume Calculation'
      write(6,*)'3) Create an Organ'
      write(6,*)'4) Create Voxel Phantom'
      write(6,*)'5) Quit Program'
      write(6,*)' '
c   return
      end
```

```

Subroutine Thold(Data,tval,zslice,incr)
C
C This subroutine segments the image into objects with
C pixel values greater than the inputed threshold.
C.....
Integer data(64,64),seg(64,64),tot,incr
Integer*4 maxval,threshval,zslice
Real*4 tval
Common pixsize
C.....
C Find maximum count value in image
maxval=0
do 60 i=1,64
do 70 j=1,64
if(data(i,j) .gt. maxval)then
maxval=data(i,j)
else
maxval=maxval
end if
70 continue
60 continue
C
C Determine threshold value
threshval=nint(tval*maxval)
C
C Zero segmented image matrix
do 80 i=1,64
do 90 j=1,64
seg(i,j)=0
90 continue
80 continue
C Segment image
do 100 i=1,64
do 110 j=1,64
if(data(i,j) .gt. threshval) then
seg(i,j)=data(i,j)
end if
110 continue
100 continue
C
C.....
C call subroutine contour
do 120 i=1,64
do 130 j=1,64
tot=0
if(seg(i,j) .eq. 0) go to 130
call contour(i,j,seg,incr,tot,pixsize,zslice)
130 continue
120 continue
close(unit=3)
return
end

```

```

Subroutine Contour(l,m,bin,inx,totalct,pixs,z)
C
C This subroutine traces out objects in the segmented
C image. Stores the objects indices,volume,voxel id,
C and count.
C.....
Integer l,m,inx,bin(64,64),minx,maxx,miny,maxy,width
Integer length,totalct,numvox,area,xloc(256),yloc(256)
Integer obj(64,64),objct,p,r,q,zmin,zmax,o,c(256),w,t
Integer chkx,chky,temp(64,64),pw,tx,ty,tc(256)
Integer xs(4096),ys(4096),cs(4096),cont(64,64)
Integer*4 z
Real volume,center,avgct
Real*4 pixs,voxvol
Character oname*15,inum*4,objname*15
C.....
voxvol=pixs**3
k=1
C Zero indice matrices
do 200 i=1,64
xloc(i)=0
yloc(i)=0
200 continue
C.....
C Setup temporary matrix to store ct array,bin()
do 290 i=1,64
do 300 j=1,64
temp(i,j)=bin(i,j)
300 continue
290 continue
C.....
C Trace object contour
xloc(k)=1
yloc(k)=m
obj(l,m)=1
9 if(bin(l-1,m+1) .ne. 0) then
l=l-1
m=m+1
k=k+1
xloc(k)=1
yloc(k)=m
obj(l,m)=1
go to 9
end if
31 if(bin(l,m+1) .ne. 0) then
m=m+1
k=k+1
xloc(k)=1
yloc(k)=m
obj(l,m)=1
go to 9
end if

```

```
41  if(bin(l+1,m+1) .ne. 0) then
    l=l+1
    m=m+1
    k=k+1
    xloc(k)=1
    yloc(k)=m
    obj(l,m)=1
    go to 9
    end if
51  if(bin(l+1,m) .ne. 0) then
    l=l+1
    k=k+1
    xloc(k)=1
    yloc(k)=m
    obj(l,m)=1
    go to 41
    end if
61  if(bin(l+1,m-1) .ne. 0) then
    l=l+1
    m=m-1
    k=k+1
    xloc(k)=1
    yloc(k)=m
    obj(l,m)=1
    go to 41
    end if
71  if(bin(l,m-1) .ne. 0) then
    m=m-1
    if((l .eq. xloc(1)).and.(m .eq. yloc(1))) go to 401
    k=k+1
    xloc(k)=1
    yloc(k)=m
    obj(l,m)=1
    go to 61
    end if
81  if(bin(l-1,m-1) .ne. 0) then
    l=l-1
    m=m-1
    if((l .eq. xloc(1)).and.(m .eq. yloc(1))) go to 401
    k=k+1
    xloc(k)=1
    yloc(k)=m
    obj(l,m)=1
    go to 71
    end if
91  if(bin(l-1,m) .ne. 0) then
    l=l-1
    if((l .eq. xloc(1)).and.(m .eq. yloc(1))) go to 401
    k=k+1
    xloc(k)=1
    yloc(k)=m
    obj(l,m)=1
```

```

go to 81
end if
101 if(bin(l-1,m+1) .ne. 0) then
l=l-1
m=m+1
if((l .eq. xloc(1)).and.(m .eq. yloc(1))) go to 401
k=k+1
xloc(k)=l
yloc(k)=m
obj(l,m)=1
go to 81
end if
201 if(bin(l,m+1) .ne. 0) then
m=m+1
if((l .eq. xloc(1)).and.(m .eq. yloc(1))) go to 401
k=k+1
xloc(k)=l
yloc(k)=m
obj(l,m)=1
go to 81
end if
301 if(bin(l+1,m+1) .ne. 0) then
l=l+1
m=m+1
if((l .eq. xloc(1)).and.(m .eq. yloc(1))) go to 401
k=k+1
xloc(k)=l
yloc(k)=m
obj(l,m)=1
go to 101
end if
C.....
c   Reset bin pixels if isolated point
401 if(k .eq. 1) then
obj(xloc(1),yloc(1))=0
go to 1000
end if
C.....
c   Calculate width,length,center,area
minx=xloc(1)
maxx=xloc(1)
miny=yloc(1)
maxy=yloc(1)
do 210 i=2,k
if(xloc(i) .lt. minx)minx=xloc(i)
if(xloc(i) .gt. maxx)maxx=xloc(i)
if(yloc(i) .lt. miny)miny=yloc(i)
if(yloc(i) .gt. maxy)maxy=yloc(i)
210 continue
width=maxy-miny
length=maxx-minx
area=width*length

```

```

center=real((maxx-minx)/2.0)
c.....
c   Write object contour to file object.dat
   write(unit=inum,fmt='(I4)')inx
   if(inum(1:3) .eq. ' ')then
   oname='OBJECT'//inum(4:4)
   else if (inum(1:2) .eq. ' ')then
   oname='OBJECT'//inum(3:4)
   else if (inum(1:1) .eq. ' ')then
   oname='OBJECT'//inum(2:4)
   else
   oname='OBJECT'//inum(1:4)
   end if
   open(unit=2,file=oname,status='new')
write(2,703)z,oname
703  format(2x,'Slice=',I2,10x,a15)
   do 270 i=1,64
   write(2,704)(obj(i,j),j=1,64)
704  format(64I2)
270  continue
   close(unit=2)
c.....
c   Zero contour matrix
   do 279 i=1,64
   do 278 j=1,64
   cont(i,j)=0
278  continue
279  continue
c   Count voxels
   p=1
   w=0
   numvox=0
   objct=0
   do 220 i=1,k
   chkx=xloc(i)
   chky=yloc(i)
   if(i .eq. 1) go to 223
   if(w .eq. 0) go to 222
   do 230 t=1,w
   if(chkx .eq. xloc(c(t))) go to 220
230  continue
222  if(i .eq. k) go to 224
223  do 240 j=i+1,k if (xloc(j) .eq. chkx) then
   w=w+1
   c(w)=j
   end if
240  continue
224  if((w .eq. 0).or.(i .eq. k)) then
   numvox=numvox+1
   objct=objct+bin(chkx,chky)
   cont(chkx,chky)=bin(chkx,chky)
   bin(chkx,chky)=0

```

```

obj(chkx, chky)=0
go to 220
end if
zmin=yloc(c(p))
zmax=yloc(c(p))
do 250 o=p+1,w
if(yloc(c(o)) .lt. zmin)zmin=yloc(c(o))
if(yloc(c(o)) .gt. zmax)zmax=yloc(c(o))
250 continue
if(chky .gt. zmax)zmax=chky
q=chkx
if((zmax .gt. 0).and.(zmin .eq. 0)) then
numvox=numvox+1
objct=objct + bin(chkx, chky)
cont(chkx, chky)=bin(chkx, chky)
bin(chkx, chky)=0
obj(chkx, chky)=0
go to 220
end if
do 260 r=zmin, zmax
numvox=numvox+1
objct=objct+bin(q, r)
cont(q, r)=bin(q, r)
bin(q, r)=0
obj(q, r)=0
260 continue
p=w+1
220 continue
c.....
c Calculate object parameters
volume=numvox*voxvol
totalct=totalct+objct          avgct=totalct/numvox
c.....
c Write object info to file objval.dat
write(1,706)z,inx,numvox,totalct,avgct,volume,width,
1 length,area,center,minx,maxx,miny,maxy
706 format(1x,I2,1x,I3,2x,I4,1x,I6,1x,F7.2,1x,F7.2,1x,I4,2x,
1 I4,3x,I4,1x,F5.2,3x,I2,3x,I2,3x,I2,3x,I2)
c.....
c Write object pixels to file objpix.dat
write(unit=inum,fmt='(I4)')inx
if(inum(1:3) .eq. ' ')then
objname='OBJPIX'//inum(4:4)
else if(inum(1:2) .eq. ' ')then
objname='OBJPIX'//inum(3:4)
else if(inum(1:1) .eq. ' ')then
objname='OBJPIX'//inum(2:4)   else
objname='OBJPIX'//inum(1:4)
end if
open(unit=3,file=objname,status='new')
write(3,707)
707 format(' Z',3x,'X',3x,'Y',4x,'Ct')

```

```
c      Remove duplicate values from xloc and yloc
      pw=0
      do 275 i=1,64
      do 276 j=1,64
      if(cont(i,j) .ne. 0)then
      pw=pw+1
      xs(pw)=i
      ys(pw)=j
      cs(pw)=cont(i,j)
      end if
276  continue
275  continue
      do 274 i=1,pw
      w r i t e ( 3 , 7 0 8 ) z , x s ( i ) , y s ( i ) , c s ( i )
708  format(1x,I2,2x,I2,2x,I2,2x,I4)
274  continue
C.....
      inx=inx+1
1000 return
      end
```

Subroutine Objselect(objnum)

```

c
c This subroutine sums the objects in each slice to form
c a complete organ/object, whereby its volume is
c calculated. The object is assigned an ID number, medium,
c organ, which is written to a file.
c.....
Integer obj,medno,id1,id2,id3,id4,x(4096),y(4096)
Integer zs(4096),oct(4096) counter,objnum,xi
Integer sxloc(30000),syloc(30000),soctn(30000)
Integer incl,octer,nw,pp,ss(30000),selob(64)
Integer*4 totct,objvox,otot,nvoxel
Real psize,sw,ssr(30000),srxloc(30000),syrloc(30000)
Real zmin,zmax,ymin,ymax,xmin,xmax
Real*4 organvol,select,avgct,wt(30000)
Character organ*16
c.....
write(6,*)'Enter the Selected Object Contour Number:'
read(5,*)obj
write(6,*)'Enter the Image Pixel Size (cm):'
read(5,*)psize
write(6,*)'Enter the Image Slice Size (cm):'
read(5,*)sw
write(6,*)'Enter Organ Name:'
read(5,810)organ
810 format(a16)
write(6,*)'Enter Organ Medium Number(1-bone,2-soft
tiss,3-lung,4-void)'
read(5,*)medno
write(6,*)'Enter Whole Body Region Number:'
read(5,*)id1
write(6,*)'Enter Organ ID Number:'
read(5,*)id2
write(6,*)'Enter Organ Subregion Number:'
read(5,*)id3
write(6,*)'Enter Organ Subregion Grouping Number:'
read(5,*)id4
c-----
c Open Selected Object File
c Call fopen(obj,counter,zs,x,y,oct)
c-----
c Calculate select object total count,number of voxels,
c volume and pixels
totct=0
objvox=0
xi=0
Call subjct(counter,oct,totct,objvox,xi)
c Store selected object pixels in separate matrix
nw=xi
do 370 i=1,nw
ss(i)=zs(i)
sxloc(i)=x(i)

```

```

    syloc(i)=y(i)
    soctn(i)=oct(i)
370 continue
    otot=totct
    nvoxel=objvox
    pp=1
    selob(pp)=obj
c   Open other object files
    do 380 j=1,objnum
    do 381 i=1,pp
    if(j .eq. selob(i)) go to 380
381 continue
    call fopen(j,counter,zs,x,y,oct)
    call sobjct(counter,oct,totct,objvox,xi)
c   Check the number object pixels in select object,
c   include > 90%
    octer=0
    incl=0
    do 390 i=1,xi
    octer=octer+1
    do 400 k=1,nw
    if((x(i) .eq. sxloc(k)).and.(y(i) .eq. syloc(k)))then
        incl=incl+1
    end if
400 continue
390 continue
c   Include if 90% of object pixels in selected object
    select=real(incl/octer)
    if(select .ge. 0.90)then
        do 410 i=1,xi
            k=nw+i
            ss(k)=zs(i)
            sxloc(k)=x(i)
            syloc(k)=y(i)
            soctn(k)=oct(i)
410         continue
            pp=pp+1
            selob(pp)=j
            otot=otot+totct
            nvoxel=nvoxel+objvox
            nw=nw+xi
        end if
380 continue
c   Calculate weighting factor
    avgct=real(otot/nvoxel)
    do 415 j=1,nw
c   Converts z,x,y into real coordinates (cm)
    ssr(j)=ss(j)*sw
    sxrloc(j)=(sxloc(j)-32)*psize
    syrloc(j)=(syloc(j)-32)*psize
c   Calculate voxel weights
    wt(j)=soctn(j)/avgct

```

```
415 continue
c   Calculate organ volume
    organvol=nvoxel*(psize**3)
c   Find organ minimum and maximum coordinates
    call voxmax(ssr,sxrloc,syrloc,nw,zmax,xmax,ymax,zmin,
1   xmin,ymin)
c   Write results to file
    write(7,416)psize,sw
416 format(1x,F5.3,1x,F5.3)
    write(7,417)nvoxel,zmax,xmax,ymax,zmin,xmin,ymin,
1   organvol,avgct
417 format(1x,I5,1x,F8.3,1x,F8.3,1x,F8.3,1x,F8.3,1x,
1   F8.3,1x,F8.3,1x,F8.3,1x,F8.3)
    do 420 i=1,nw
        write(7,820)ssr(i),sxrloc(i),syrloc(i),soctn(i),
1   wt(i),organ,medno,id1,id2,id3,id4
820 format(1x,F7.3,1x,F7.3,1x,F7.3,1x,I3,1x,F5.3,1x,a10,
1   1x,I1,2x,I3,1x,I3,1x,I3,1x,I3)
420 continue
c-----
    return
    end
```

```
Subroutine Sobjct(ct,octs,stot,sobjvox,sxi)
```

```
C  
C This subroutine determines the number of voxels and total  
C number of voxels.
```

```
C-----  
Integer octs(4096),sxi,ct  
Integer*4 stot,sobjvox
```

```
C-----  
sxi=0  
sobjvox=0  
stot=0  
do 310 i=1,ct  
sxi=sxi+1  
sobjvox=sobjvox+1  
stot=stot+octs(i)  
310 continue
```

```
C-----  
return  
end
```

```
C*****
```

Subroutine FOPEN(sobj,cter,szs,sx,sy,soct)

```

C
C   This subroutine opens files based on sobj and returns
C   slice,x,y,and pixel ct
C-----
C   Integersobj,cter,szs(4096),sx(4096),sy(4096),soct(4096)
C   Character selobj*15,head*20,num*3
C-----
write(unit=num,fmt='(I3)')sobj
if(num(1:1).eq.' ')then
    selobj='OBJPIX'//num(3:3)
else
    selobj='OBJPIX'//num(2:3)
end if
selobj='OBJPIX'//num(1:3)
open(unit=3,file=selobj,status='old')
read(3,305)head
305 format(a20)
    cter=1
307 read(3,900,end=306)szs(cter),sx(cter),sy(cter),soct(cter)
900 format(1x,I2,2x,I2,2x,I2,2x,I4)
    cter=cter+1
    go to 307
306 close(unit=3)
    cter=cter-1
C.....
return
end

```

```

SubroutineVoxmax(z,x,y,n,zmax,xmax,ymax,zmin,xmin,ymin)
C
C   This subroutine finds the maximum and minimum voxel
C   location
C.....
      Integer n
      Real z(30000),x(30000),y(30000),zmax,xmax,ymax
      Real zmin,xmin,ymin
C.....
C   Find minimum and maximum z coordinate
      zmin=z(1)
      zmax=z(1)
      do 405 k=2,n
      if(z(k) .gt. zmax)zmax=z(k)
      if(z(k) .lt. zmin)zmin=z(k)
405 continue
C
C   Find maximum and minimum x
      xmax=x(1)
      xmin=x(1)
      do 407 k=2,n
      if(x(k) .gt. xmax)xmax=x(k)
      IF(x(k) .lt. xmin)xmin=x(k)
407 continue
C
C   Find maximum and minimum y
      ymax=y(1)
      ymin=y(1)
      do 412 k=2,n
      if(y(k) .gt. ymax)ymax=y(k)
      if(y(k) .lt. ymin)ymin=y(k)
412 continue
C.....
      return
      end

```

Subroutine Corgan

```

C
C This subroutine allows for the creation of an organ
C for the reflection properties. The user inputs the voxels
C and their characteristics.
C.....
Integer bos,eos,ho,xvmin,yvmin,xvmax,yvmax,id0,id1,id2
Integer id3,id4,medno,x(4096),y(4096),z(4096),sct
Integer*4 cttot,nvox,c,r
Real xr(20000),yr(20000),zr(20000),ops,oss,zmax,xmax
Real ymax,zmin,xmin,ymin
Real*4 vorgan,wt(20000),avgct
Character organ*16
C.....
c=1
r=0
write(6,*)' Enter the Image Pixel Size (cm):'
read(5,*)ops
write(6,*)' Enter the Image Slice Size (cm):'
read(5,*)oss
write(6,*)' Enter the Organ Name:'
read(5,902)organ
902 format(a16)
write(6,*)' Enter the Organ Number:'
read(5,*)id0
write(6,*)'Enter Organ Medium Number(1-bone,2-soft
1      tiss,3-lung,4-void) '
read(5,*)medno
write(6,*)' Enter Whole Body Region Number:'
read(5,*)id1
write(6,*)' Enter Organ ID Number:'
read(5,*)id2
write(6,*)' Enter Organ Subregion Number:'
read(5,*)id3
write(6,*)' Enter Organ Subregion Grouping Number:'
read(5,*)id4
cttot=0
nvox=0
write(6,*)' The maximum image size is 64x64.'
write(6,*)' The maximum number of image slices is 64.'
write(6,*)' '
2 write(6,*)' Enter the beginning and ending slice
1      number(1,64=all):'
read(5,*)bos,eos
if((eos .gt. 64).or.(bos .lt. 1))then
    write(6,*)' Maximum number of slices is 64,Try
1      Again!'
    go to 2
end if
write(6,*)'Enter 1,If all slices contain the same number
1      of voxels:'
read(5,*)ho

```

```

    if(ho .eq. 1)go to 3
    do 15 i=bos,eos
    write(6,905) i
905  format(' For Slice=',I2)
    write(6,*)' Enter minimum and maximum X voxel
1    coordinates:'
    read(5,*)xvmin,xvmax
    write(6,*)' Enter minimum and maximum Y voxel
1    coordinates:'
    read(5,*)yvmin,yvmax
    write(6,*)'Enter the slice voxel count (0-255):'
    read(5,*)sct
    do 25 k=xvmin,xvmax
    do 35 j=yvmin,yvmax
        nvox=nvox+1
        cttot=cttot+sct
        x(nvox)=k
        y(nvox)=j
        z(nvox)=i
35  continue
25  continue
    go to 4
15  continue
    go to 7
3   write(6,*)' Enter minimum and maximum X voxel
1   coordinates:'
    read(5,*)xvmin,xvmax
    write(6,*)' Enter minimum and maximum Y voxel
1   coordinates:'
    read(5,*)yvmin,yvmax
    write(6,*)'Enter the voxel count (0-255):'
    read(5,*)sct
    do 45 i=bos,eos
    do 46 j=xvmin,xvmax
    do 47 k=yvmin,yvmax
        nvox=nvox+1
        cttot=cttot+sct
        x(nvox)=j
        y(nvox)=k
        z(nvox)=i
47  continue
46  continue
45  continue
4   avct=real(cttot/nvox)
    do 55 l=c,nvox+r
        wt(l)=sct/avct
55  continue
    c=nvox+1
    r=nvox
    if(ho .ne. 1)go to 15
7   open(unit=7,file='voxel',status='new')
    do 56 m=1,nvox

```

```

xr(m)=(x(m)-32)*ops
yr(m)=(y(m)-32)*ops
zr(m)=z(m)*oss
56 continue
c Calculate organ volume
vorgan=nvox*(ops**3)
c Find minimum and maximum organ coordinates
callvoxmax(zr,xr,yr,nvox,zmax,xmax,ymax,zmin,xmin,ymin)
c Write results to file
write(7,906)nvox,zmax,xmax,ymax,zmin,xmin,ymin,vorgan
906 format(1x,I5,1x,F8.3,1x,F8.3,1x,F8.3,1x,F8.3,1x,
1 F8.3,1x,F8.3,1x,F8.3)
do 57 n=1,nvox
write(7,910)zr(n),xr(n),yr(n),sct,wt(n),organ,medno,ido,
1 id1,id2,id3,id4
910 format(1x,F7.3,1x,F7.3,1x,F7.3,1x,I3,1x,F5.3,1x,A10,1x,
1 I1,2x,I3,1x,I3,1x,I3,1x,I3,1x,I3)
57 continue
close(unit=7)
C.....
return
end

```

Subroutine Voxfil

```

C
C   This subroutine reads the voxel data files,"voxel.dat",
C   for all organs to create one large file, "voxphan".
C.....
Integer norg,fvox(20),medno(100000),id1(100000)
Integerid3(100000),id4(100000),ct(100000),d,id2(100000)
Integer*4 tnvox
Real z(100000),x(100000),y(100000),volume(20)
Real zmax(20),xmax(20),psize,ssize
Real zmin(20),xmin(20),ymin(20),ymax(20)
Real*4 wt(100000)
Character orgfil*15,num*2
Character*16 organ(100000),nmorg(20)
C.....
d=1
tnvox=0
write(6,*)'Maximum number of organs is 20!'
write(6,*)'Enter the number of organs(#voxel files):'
read(5,*)norg
do 21 i=1,norg
write(unit=num,fmt='(I2)')i
if(num(1:1) .eq. ' ')then
    orgfil='voxel.dat;'//num(2:2)
else
    orgfil='voxel.dat;'//num(1:2)
end if
open(unit=11,file=orgfil,status='old')
C   Read pixel size and slice size
read(11,610)psize,ssize
610 format(1x,F5.3,1x,F5.3)
C   Read number of voxels in the file
read(11,620)fvox(i),zmax(i),xmax(i),ymax(i),zmin(i),
1   xmin(i),ymin(i),volume(i)
620 format(1x,I5,1x,F8.3,1x,F8.3,1x,F8.3,1x,F8.3,1x,F8.3,1x,
1   F8.3,1x,F8.3)
tnvox=tnvox+fvox(i)
do 22 j=d,tnvox
read(11,625,end=23)z(j),x(j),y(j),ct(j),wt(j),organ(j),
1   medno(j),id1(j),id2(j),id3(j),id4(j)
625 format(1x,F7.3,1x,F7.3,1x,F7.3,1x,I3,1x,F5.3,1x,A10,
1   1x,I1,2x,I3,1x,I3,1x,I3,1x,I3)
22 continue
23 nmorg(i)=organ(tnvox)
close(unit=11)
d=tnvox+1
21 continue
open(unit=12,file='voxphan',status='new')
C   Write results to file
C   Total number of voxels and organs, pixel and slice size
write(12,627)tnvox,norg,psize,ssize
627 format(1x,I7,1x,I2,1x,F5.3,1x,F5.3)

```

```

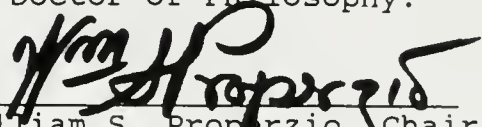
c   Write #voxels,minimum and maximum coordinates, volume
c   of each organ
      do 25 j=1,norg
        write(12,628) nmorg(j),fvox(j),zmax(j),xmax(j),ymax(j),
1       zmin(j),xmin(j),ymin(j),volume(j)
628   format(1x,A10,1x,I5,1x,F8.3,1x,F8.3,1x,F8.3,1x,
1       F8.3,1x,F8.3,1x,F8.3,1x,F8.3)
25   continue
      do 24 k=1,tnvox
        write(12,629) z(k),x(k),y(k),ct(k),wt(k),organ(k),
1       medno(k),id1(k),id2(k),id3(k),id4(k)
629   format(1x,F7.3,1x,F7.3,1x,F7.3,1x,I3,1x,F5.3,1x,A10,
1       1x,I1,2x,I3,1x,I3,1x,I3,1x,I3)
24   continue
      close(unit=12)
C.....
      return
      end

```

BIOGRAPHICAL SKETCH

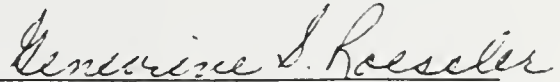
Latresia Ann Wilson was born in 1963 in Miami, Florida. She grew up and attended high school in Ocala, Florida whereupon she graduated in 1981. She received a Bachelor of Science Degree in Nuclear Engineering in 1985 and a Master of Science Degree in Nuclear Engineering in 1986 from the University of Virginia. At present she is completing her Ph.D. degree in Medical Health Physics in the Department of Environmental Engineering Sciences at the University of Florida.

I certify that I have read this study and that in my opinion it conforms to acceptable standards of scholarly presentation and is fully adequate, in scope and quality, as a dissertation for the degree of Doctor of Philosophy.



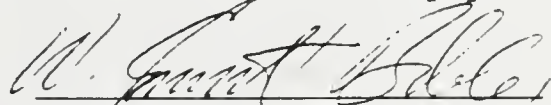
William S. Properzio, Chair
Associate Professor of
Environmental Engineering
Sciences

I certify that I have read this study and that in my opinion it conforms to acceptable standards of scholarly presentation and is fully adequate, in scope and quality, as a dissertation for the degree of Doctor of Philosophy.



Genevieve S. Roessler
Genevieve S. Roessler
Associate Professor of Nuclear
Engineering Sciences

I certify that I have read this study and that in my opinion it conforms to acceptable standards of scholarly presentation and is fully adequate, in scope and quality, as a dissertation for the degree of Doctor of Philosophy.



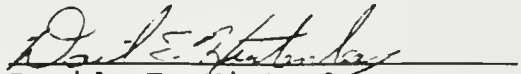
W. Emmett Bolch
W. Emmett Bolch
Professor of Environmental
Engineering Sciences

I certify that I have read this study and that in my opinion it conforms to acceptable standards of scholarly presentation and is fully adequate, in scope and quality, as a dissertation for the degree of Doctor of Philosophy.



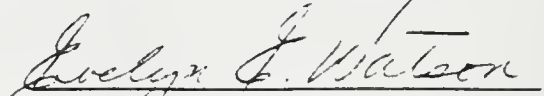
Walter E. Drane
Walter E. Drane
Assistant Professor of Radiology

I certify that I have read this study and that in my opinion it conforms to acceptable standards of scholarly presentation and is fully adequate, in scope and quality, as a dissertation for the degree of Doctor of Philosophy.



David E. Hintenlang
Assistant Professor of Nuclear
Engineering Sciences

I certify that I have read this study and that in my opinion it conforms to acceptable standards of scholarly presentation and is fully adequate, in scope and quality, as a dissertation for the degree of Doctor of Philosophy.



Evelyn E. Watson
Oak Ridge Associated
Universities

This dissertation was submitted to the Graduate Faculty of the College of Engineering and to the Graduate School and was accepted as partial fulfillment of the requirements for the degree of Doctor of Philosophy.

December 1990


for Dean, College of
Engineering

Dean, Graduate School

